Fluorescence imaging of cellular organelles and membrane dynamics

by

Chamari S. Wijesooriya

A dissertation submitted to the graduate faculty

in partial fulfillment of the requirements for the degree of

DOCTOR OF PHILOSOPHY

Major: Analytical Chemistry

Program of Study Committee:
Emily A. Smith, Major Professor
Arthur Winter
Young-Jin Lee
Robbyn K. Anand
Brett VanVeller

The student author, whose presentation of the scholarship herein was approved by the program of study committee, is solely responsible for the content of this dissertation. The Graduate College will ensure this dissertation is globally accessible and will not permit alterations after a degree is conferred.

Iowa State University

Ames, Iowa

2019

DEDICATION

This dissertation is dedicated to my parents, husband Nuwan, loving daughter Sandali, and especially to my uncle Bimal De Silva who encouraged me to pursue my higher studies in the United States.

TABLE OF CONTENTS

Page

ACKNOWLEDGEMENTS

First and foremost, I sincerely thank Dr. Emily Smith for her excellent guidance, encouragement, and continuous support during my time at Iowa State University. Her wealth of knowledge, creativity, and inspirations have greatly helped my achievements. I would also like to thank my committee members Drs. Arthur Winter, Robbyn Anand, Young-Jin Lee, and Brett VanVeller for their support and advise throughout my graduate studies. I would especially like to thank Dr. Mohan Gupta for serving as a temporary committee member for my final oral defense. I also acknowledge the funding provided by National Science Foundation. The administrative support provided by Lynette Edsall, Renee Harris, Amy Carver, and Carlene Auestad was also appreciated.

I extend my sincere thanks to Dr. Arthur Winter for providing me the opportunity to work on successful collaborations with his research group. My thanks also goes to Dr. Jake Zimmerman and his students for a successful collaboration. I also thank Julie Peterson, Pradeep Shrestha and Dr. Kalyan Santra for their excellent support and colloboration with our research projects.

I would like to thank the past and present members of Smith group: Dr. Aleem Syed, Dr. Qiaochu Zhu, Dr. Avinash Singh, Brett, Charles, Daniel, Deyny, Jingzhe, Nicole, and Sadie for their support throughout my time at ISU as well as for making the overall journey enjoyable.

Special thanks go to my parents, grandparents, daughter, and siblings for their unconditional love and giving me the courage to pursue my graduate studies. I also thank my friends Himashi, Dilini, Kasuni, Sagarika, Lakshmi, Waruni, Ravindu, Mohan, Dinuka, Gayan, and Roshan for their kind help in various ways. Last but not least my heartiest thanks goes to my loving husband Nuwan, for being extremely supportive and patient throughout this journey.

ABSTRACT

Fluorescence microscopy is a versatile technique for studying biological structures in their native environment. The live cell imaging ability of this technique enables the study of dynamic processes in biological systems. Fluorophores play an important role in fluorescence-based cellular imaging. Development of cell permeable, non-toxic, small organic molecules with specific targeting ability is advantageous for imaging of live cellular organelles. Two coumarin-based compounds were developed to selectively target the endoplasmic reticulum (ER), which is the largest organelle in most mammalian cell types. Unlike the commercially available ER targeting probes, the coumarin-based compounds can be used to image the ER in both live and fixed cells. The simple synthetic procedure, bright emission in the blue region, narrow emission profile, low toxicity, and the specificity contribute to the utility of these probes for imaging the dynamic events of the ER.

The spatial resolution the traditional optical microscopy is limited by the diffraction of light. Subcellular organelles are in the nanometer size range, and the majority of the biological phenomena happen in the nanoscale. Therefore traditional light microscopic techniques have limited capability of studying these systems. Super-resolution microscopic techniques that were developed in the past decade to overcome this issue. Single molecule localization microscopy (SMLM) is based on the activation and excitation of subsets of fluorophores, followed by their localization with nanometer spatial resolution to generate a super-resolution image. Traditional SMLM fluorophores have the drawbacks of requiring two high power lasers including lasers emitting in the ultra-violet range. Also, the requirement of harsh chemicals in the imaging medium limits the ability to image live cells. A BODIPY-based photoactivatable probe is developed as a promising probe for SMLM. A single low-power visible laser is utilized without

requiring harsh conditions in the imaging medium to make this probe exceptionally useful for imaging in biological systems. The probe can be simply linked to nucleophile-containing targeting groups to image specific cellular components. Super-resolution images of *in vitro* and *in vivo* microtubules are generated using paclitaxel attached probe.

Membrane receptors are one of the major components that contribute to the control of cellular function. Interactions of receptor proteins with extracellular ligands, other membrane constituents, and intracellular components result in the activation of intracellular signaling mechanisms. These dynamic interactions are governed by the lateral diffusion of membrane components. RAGE is a multi-ligand receptor responsible for various pathological diseases. Amyloid beta 1-40 and 1-42 peptides react with RAGE protein to stimulate neuronal dysfunction and are also responsible for Alzheimer's disease. The effects of these peptides on RAGE diffusion is not yet known. The fluorescence-based single particle tracking method is used to measure the effect of amyloid beta ligands for the lateral diffusion of the receptor for advanced glycation endproducts (RAGE) at the single receptor level. Both of the peptides altered the RAGE membrane diffusion, but to a different extent. Activation of the p38 MAPK pathway is observed for the treatment of RAGE with amyloid beta 1-42 ligand. The effect of different oligomeric forms of these two peptides on the RAGE diffusion and signaling is further studied.

DISSERTATION OVERVIEW

This dissertation is categorized into 5 chapters. Chapter 1 contains an introduction to optical methods to measure the nanoscale organization and dynamics of biological systems. Chapter 2 describes the development of coumarin-based fluorophores to selectively image the endoplasmic reticulum in mammalian cells. In Chapter 3, the development of a BODIPY-based photoactivatable probe and its utility for localization-based super-resolution imaging is described. The work presented in Chapter 4 targeted to measure the effect of amyloid beta ligand on RAGE lateral diffusion using single particle tracking method. General conclusions and possible future insights are summarized in Chapter 5.

CHAPTER 1. GENERAL INTRODUCTION

OPTICAL IMAGING OF THE NANOSCALE STRUCTURE AND DYNAMICS OF BIOLOGICAL MEMBRANES

Modified from a review article published in Analytical Chemistry

Chamari S. Wijesooriya, Charles K. A. Nyamekye, Emily A. Smith*

Department of Chemistry, Iowa State University, Ames, Iowa 50011 USA

1.1 Introduction

Biological membranes serve as the fundamental unit of life, allowing the compartmentalization of cellular contents into subunits with specific functions. The bilayer structure, consisting of lipids, proteins, small molecules, and sugars, also serves many other complex functions in addition to maintaining the relative stability of the inner compartments. Signal transduction, regulation of solute exchange, active transport, and energy transduction through ion gradients all take place at biological membranes, primarily with the assistance of membrane proteins. For these functions, membrane structure is often critical. The fluid-mosaic model introduced by Singer and Nicolson in 1972 evokes the dynamic and fluid nature of biological membranes.[1] According to this model, integral and peripheral proteins are oriented in a viscous phospholipid bilayer. Both proteins and lipids can diffuse laterally through the two-dimensional structure. Modern experimental evidence has shown, however, that the structure of the membrane is considerably more complex; various domains in the biological membranes, such as lipid rafts and confinement regions, form a more complicated molecular organization. The proper organization and dynamics of the membrane components are critical for the function of the entire cell. For example, cell signaling is often initiated at biological membranes and requires receptors to diffuse and assemble into complexes and clusters, and the resulting

downstream events have consequences throughout the cell. Revealing the molecular level details of these signaling events is the foundation to understanding numerous unsolved questions regarding cellular life.

Optical imaging methods have substantial utility in revealing information about biological materials. They offer simple sample preparation, the ability to noninvasively image samples in situ and in vivo, the ability to simultaneously image several different properties, and compatibility with many other imaging techniques. The earliest applications of optical imaging to measure cellular membranes revealed their basic structure and their dynamic properties at the ensemble level. Many important molecular assemblies in biological membranes occur in the nanometer scale; thus, diffraction-limited optical techniques are unable to resolve them. The development of super-resolution optical imaging techniques has accelerated the study of biological membranes, sometimes one molecule at a time. Within the past few years, multimodal and multicolor imaging approaches were developed to facilitate multivariable imaging of membranes, primarily with fluorescence contrast. Recent advances in Raman scattering techniques have paved the path to obtain chemical information at the nanoscale level. The introduction of novel and highly selective probes, advanced light sources, novel detectors with fast detection rates and high quantum yields, and modifications to optics that provide optimized signals as well as recent big data efforts have all helped improve image quality and analysis and have thus led to a better understanding of membrane-related phenomena.

This review summarizes the optical imaging instrumentation that has recently been developed or is being developed in order to measure membrane organization and dynamics as well as some of the key applications of these instruments for membrane studies. The developments and applications of fluorescence and Raman-based imaging methods are covered.

Atomic force microscopy, mass spectroscopy, and electron microscopy methods are useful for revealing complementary details about membrane structure and dynamics, but will not be covered herein, nor will studies of model membranes, such as those using supported lipid bilayers.

1.2 Fluorescence Microscopy Techniques

Fluorescence techniques have been valuable tools for the study of biological membranes for many decades. They have the advantages of allowing live cell imaging with fast time resolution and the sensitivity to measure single fluorescent molecules or probes. Recent developments in subdiffraction or super-resolution fluorescence-based techniques have expanded our knowledge of membrane structure and dynamics. In many cases, these super-resolution imaging techniques have been used in combination with well-established fluorescence techniques to reveal information about membrane nanostructure and dynamics that cannot be measured using a diffraction-limited analysis volume.

The well-established fluorescence imaging techniques that have been used for biological membrane studies include: fluorescence lifetime imaging (FLIM), fluorescence resonance energy transfer (FRET), fluorescence recovery after photobleaching (FRAP), single particle tracking (SPT), and fluorescence correlation spectroscopy (FCS). FLIM is widely used to measure protein-protein interactions, protein conformational changes, and lipid domains within plasma membranes.[2,3] The fluorescent probe's lifetime is used to generate the image, which has the benefit of being independent of probe concentration. FRET is also used to elucidate membrane protein interactions and conformational kinetics,[4-9] and is exquisitely sensitive to a separation distance of less than 10 nm. FRAP,[10-14] SPT[15,16] and FCS[17,18] are well suited to measure membrane dynamics. FRAP is an ensemble technique in which the target is linked to a fluorescent probe and a selected region is photobleached with a high-power laser beam.

Fluorescence recovery over time at the bleached region is used to analyze the diffusion properties of the labeled target. In SPT, a membrane component is tagged with a photostable fluorescent probe (e.g., quantum dots) and the movement of the probe is recorded over time to generate the trajectory of the biomolecule. The statistical analysis of the trajectories can provide information about heterogeneous populations and rare populations that may be averaged out of the ensemble FRAP signal. FCS is based on the statistical analysis of the fluorescence intensity fluctuations of a small number of fluorescent probes. All factors that alter the fluorescence fluctuations such as dynamics, molecular kinetics and photophysical properties of the probes (dark and triplet states) can be measured using FCS.

Total internal reflection fluorescence microscopy (TIRFM) and light sheet microscopy (LSM) are two illumination geometries that have been widely used to image cell membranes and their components. These techniques image thin optical sheets of less than a couple hundred nanometers (TIRFM) and a couple of micrometers (LSM) and reject the extensive background from the bulk of the cell. This is important in order to image the 6 to 10 nm thick biological membrane with a high signal-to-background ratio. Recent applications of TIRFM include imaging membrane protein clusters,[19,20] the structure and dynamics of membrane transporters,[21-25] and lipid rafts.[26,27] LSM has been recently used to image the dynamics and organization of membrane proteins[28] as well as to study the changes of membrane dynamics in dividing cells.[29] Although these techniques provide signal selectivity in the axial direction (i.e., perpendicular to the focal plane), in the lateral direction they are inherently diffraction limited and by themselves are not well suited for measuring the nanoscale structure and dynamics of membranes.

1.2.1 Single Molecule Localization Microscopy (SMLM)

SMLM techniques such as photoactivated localization microscopy (PALM) [30,31] and stochastic optical reconstruction microscopy (STORM)[32,33] have gained widespread use for

imaging biological membranes. PALM uses photoactivatable fluorescent proteins and was first independently introduced by Betzig et al.[30] and Hess et al.[31] (wherein it was termed fluorescence photoactivation localization microscopy, FPALM). STORM uses organic molecules as SMLM probes and was first introduced by the Zhuang group.[32]

The SMLM techniques rely on the sequential activation of sparse subsets of fluorescent probes and the time-resolved localization of these probes with nanometer precision. An order of magnitude better spatial resolution can be achieved with SMLM techniques compared to diffraction-limited optical imaging techniques. Typical SMLM instrumentation consists of an epi-fluorescence microscope, lasers for activation and excitation of the fluorophores, and an array detector with high sensitivity and fast acquisition rates. The lasers are focused at the back focal plane of a high-numerical-aperture oil-immersion microscope objective to produce a broad (global) illumination profile at the sample plane. The very low read noise of electron-multiplying charge-coupled device (EMCCD) cameras or scientific complementary metal oxide semiconductor cameras allows for efficient signal collection from single molecules. The signal detected from a single emitting probe is fit to a Gaussian profile or similar function to localize the emitter position with precision in the nanometer range. Controlling the on and off state switching of the probe is crucial to maintaining a low number of emitters in each frame of the collected data. This is generally achieved with relatively high-power lasers and using additives such as thiol, phosphates, and oxygen scavengers in the imaging medium. For techniques that require the acquisition of images over time, as required for SMLM, drift correction is commonly required to extract accurate information from the images.

Photoactivatable, photoconvertible, or reversibly photoconvertible fluorescent proteins have been used for PALM.[34] Light irradiation converts the photoactivatable probes from the

nonfluorescent form into the fluorescent form. Photoconvertible and reversibly photoconvertible probes are converted from one fluorescent state into another fluorescent state (i.e., emitting one color to another color). This cycle can be repeated many times in reversibly photoconvertible fluorescent proteins. These proteins are genetically encoded and are coexpressed with the target, which leads to specific labeling and a high expression density suitable for PALM. This super-resolution technique is able to image the spatial distribution of membrane proteins and lipid-enriched nanodomains in cell membranes.[35-42]

Dual color PALM has the ability to image the nanoscale coassociation of two cell membrane components.[43-45] The downstream signaling molecules of T cell antigen receptor[44] and the effects of ethanol and naltrexone on the distribution of glycosylphosphatidylinositol and mu-opioid receptor[45] were studied using dual color PALM, where the sequential activation of two fluorescent proteins was achieved by altering the activation laser irradiance. Gabor et al. showed the colocalization of the cytokine receptor family members with Caveolin-1 protein using simultaneous activation of Dendra (λ_{ex} of 490 nm and λ_{em} of 507 nm, before photoactivation; λ_{ex} of 553 nm and λ_{em} of 573 nm, after photoactivation) and PAmCherry (λ_{ex}: 564 nm; λ_{em}: 595 nm) fluorescent proteins.[43] Signal from these proteins were simultaneously detected by separating the emission signal into two paths using appropriate dichroic mirrors and emission filters prior to directing the signal onto an EMCCD camera. Localized molecules were identified using a ratio of signal in the red channel divided by the intensity in both channels (0.55-0.64 for Dendra and 0.68-0.75 for PAmCherry).

PALM combined with single particle tracking (sptPALM) enables the study of heterogeneity in the dynamics of membrane components with high spatial and temporal resolution.[46,47] In contrast to traditional single particle tracking methods, sptPALM generates a

higher density of single-molecule trajectories in the membrane of a single cell. The lateral dynamics and nanoscale organization of purinergic receptor P2X7 in neuronal membranes were imaged with sptPALM. Two receptor populations were detected, a rapidly diffusing fraction and a clustered fraction (the clusters were ~ 100 nm in diameter), were detected.[48] Two color sptPALM with spectrally resolved PATagRFP (λ_{ex}: 562 nm; λ_{em}: 595 nm) and PAGFP (λ_{ex}: 475 nm; λ_{em}: 517 nm) was used by Verkhusha and coauthors to image the dynamics of two transmembrane proteins in the plasma membrane of COS-7 cells.[49]

PALM is a versatile technique capable of imaging nanoscale features, but it does require transfected fluorescent proteins that are linked to the target; thus, the study of endogenous membrane components is not possible. The linked fluorescent protein can be bulky and may also alter the dynamics of the targeted biomolecules depending on the cloning location.

STORM is based on switching organic fluorophores between the on and off fluorescent states to achieve the stochastic activation of a small subset of these molecules. In order to achieve accurate single molecule localization, only a small fraction of fluorophores can be activated at the same time, leading to one or fewer excited molecules within a diffraction-limited area. The fluorophores are converted into a long-lived triplet state called a dark state using a high irradiance excitation laser and/or using additives in the imaging medium. Oxygen scavenging buffers with mercaptoethylamine or β-mercaptoethanol are commonly used. The distribution and clustering patterns of several receptor proteins were imaged in cell membranes using STORM.[50-58]

Similar to dual color PALM, dual color STORM can measure the nanoscale coassociation of membrane components using two spectrally distinct fluorophores tagged to the membrane components. Sparse populations of both fluorophores are simultaneously activated

and excited, and the emission from both fluorophores is directed onto the detector using a dual-channel image splitter with the appropriate filters (or multiple detectors).[59-63] Dual color STORM with Atto 565 and Atto 647N revealed the clustering of two different cell antigen receptors in spatially distinct areas in B cell membrane.[61]Activation of B cells reduced the cluster size for both receptors, and the activation of one receptor had a minimal effect on the clustering of the other receptor.

A combination of PALM and STORM techniques has also been used to simultaneously image multiple components within the cell membrane.[64-73] "Ordered" and "disordered" lipid domains as well as the localization of clustered B cell receptor into ordered domains were measured in mouse B lymphoma cell membranes using this approach (Figure 1).[69] The combinations of fluorescent probes in this study were Atto 655 with Alexa Fluor 532 (i.e., dual color STORM) to localize ordered and disordered lipid domains and Atto 655 with mEos3.2 fluorescent protein (i.e., PALM/STORM) to measure colocalization of B cell receptors into ordered domains. The latter probe pair required three lasers: 647 nm solid-state laser, 561 nm solid-state laser (excitation of mEos3.2), and a 405 nm diode laser (photoactivation of mEos3.2). Laser irradiances were adjusted between 5 and 20 kW/cm^2 to achieve favorable conditions for single molecule/protein localization, and the emission was separated into two channels prior to reaching the detector.

A recent combined PALM/STORM study by Bernhem et al. measured the effect of protein overexpression on the cell membrane of HEK293a cells during transient transfection.[72] The endogenous and exogenous membrane protein distributions of Na,K-ATPase were quantified and revealed there was a competition between endogenous and exogenous expression during the transient transfection state. The exogenous population was measured by PALM

whereas the endogenous versus exogenous population was quantified with STORM. Forty one hours post-transfection, the total plasma membrane concentration of Na,K-ATPase increased by 63% over the concentration measured prior to transfection, and the amount of Na,K-ATPase attributed to endogenous expression was only 16%. Alexa Fluor 647 was used for STORM imaging with a 405 nm activation laser and 642 nm excitation laser. PALM imaging was achieved with mMaple3 fluorescent protein using a 405 nm activation laser and 561 nm excitation laser.

In another study utilizing PALM/STORM, the organization of Nipah virus proteins on the plasma membrane was detected.[73] Nipah is a biosafety level 4 human-to-human transmitted virus. The results showed clusters of virus proteins, such as attachment glycoproteins and fusion glycoproteins, were randomly distributed on the mammalian PK13 cell membrane regardless of whether virus matrix proteins were present or absent. This contradicts the previously proposed models developed using electron microscopy and biochemical methods, which show matrix proteins assist in the arrangement of glycoproteins into assembly sites at the plasma membrane. The PALM and STORM data were acquired sequentially; GFP was used for PALM with 488 nm excitation, and Alexa Fluor 647 and Cy3B were used for STORM with 639 and 532 nm excitation lasers, respectively. A 405 nm laser activated the probes. To facilitate photoswitching, oxygen scavenging buffers were used that contained 50 mM mercaptoethylamine or 140 mM □-metcaptoehanol.

The photophysical properties of the probes are critical to SMLM techniques. Assuming the noise is constant, the larger the number of detected photons, the better are the localization precision and the spatial resolution of the reconstructed image. Longer dark states help to maintain low duty cycles so that a small subset of probes can be activated and reduce multiple

detection events for the same probe. Alexa Fluor, Atto, and cyanine dyes are commonly used as STORM probes. Photoactivatable organic probes, wherein a structural rearrangement occurs upon photoillumination at a specific wavelength to generate the on state, have also gained interest for SMLM imaging. Reactivation and photoswitching of these probes are negligible due to the irreversible nature of the photoactivation. The photoactivatable probes cage 500 and cage 552 were used as SMLM probes to image the oligo/dimerization of G protein-coupled receptors with approximately 8 nm resolution.[74] A 390 nm laser was used for activation; 491 and 561 nm lasers were used to excite the activated cage 500 and cage 552, respectively. BODIPY-based photoactivatable compounds are also promissive SMLM probes for the study of membrane components.[75] These probes can be activated and excited using low power visible (~500 nm) light, and live cell imaging of membrane components is possible. Huang and co-workers introduced blinking carbon dots as SMLM probes due to their low duty cycle (~0.003), high photon count per switching event (~8000), and a high resistance to photobleaching, which is a common problem for small molecule SMLM probes (e.g., Alexa Fluor 647 and Cy5).[76] They used blinking carbon dots to image the distribution and the clustering of chemokine receptor CCR3 on the HeLa membrane.

Sharonov and Hochstrasser developed the technique called points accumulation for imaging in nanoscale topography (PAINT) as another approach to obtain the on and off switching required for SMLM probes.[77] The technique does not require a photoactivation step to generate the on state. In PAINT, fluorescent probes are freely diffusing in the imaging medium. The probes continuously and stochastically bind and unbind from the imaging target. The signal is obtained when the probe immobilizes on the target, and then disappears when the probe dissociates from the target or photobleaches. The first demonstration of PAINT took advantage

of the photophysical properties of Nile Red, which is not fluorescent in aqueous solutions but is highly fluorescent in the hydrophobic membrane environment. [77] Numerous probes have subsequently used. The binding rate is easily managed by controlling the probe concentration. Since the probes dynamically bind and unbind to the target over the course of the experiment, all of the target molecules have the potential to be imaged, even if the target density is high and simultaneous binding of the probe to all targets is prohibited.

As first described, PAINT was limited to short analysis times and single molecules could not be tracked over long times. This problem was overcome with universal PAINT (uPAINT) developed by Giannone and Hosy, which enabled the real-time dynamic imaging of live cell membrane components.[78] This method involves the use of oblique illumination of the imaging target with diffusing fluorescent ligands in the solution. Long single-molecule trajectories are obtained with high densities that reveal the local diffusion properties of target components. Dual color uPAINT with two different fluorophores (one bound to the ligand epidermal growth factor and another bound to a specific antibody, panitumumab, that prevents ligand activation by blocking the binding site) was combined with FRET to study the nanoscale localization and ligand activated dimerization of epidermal growth factor receptor (Figure 2).[79] The authors found that the activated dimers were preferentially located at the edge of the cell, and note that they were able to image the receptor moments after ligand binding occurred (i.e., the event that generated the signal), which would not have been possible with SMLM techniques that require photoswitching.

DNA-PAINT takes advantage of the reversible binding kinetics of DNA hybridization.[80,81] The docking DNA strand is bound to a primary or secondary antibody specific to the imaging target, and the imager DNA strand is bound to a fluorescent probe. DNA-PAINT

elucidated the distribution of single ryanodine receptors in cardiac myocytes.[82] The random and unconstrained arrangement of ryanodine receptors as well as the stoichiometry of the coclusters of ryanodine receptor and the regulatory protein junctophilin-2 were quantified. In another study, the nonhomogeneous distributions of five types of receptor tyrosine kinases in the plasma membrane were identified with five different fluorescent probes bound to different DNA imager strands.[83]

SMLM techniques including PALM and STORM provide nanoscale resolution with simple instrumentation compared to many other super-resolution microscopies, but they require postcapture processing and image reconstruction. Other disadvantages include slow data acquisition due to the large number of acquired frames for each reconstructed image, and the often required high irradiances are not ideal for many cellular studies. Simultaneous activation of multiple probes in a diffraction limited spot, insufficient or incomplete target labeling and limited probe accessibility due to high target packing density may all underestimate the quantity of target biomolecules. Overestimation of the probes is also possible and may result in imaging artificial clusters that do not exist in the membranes.[84] These artifacts are attributed to high photoswitching rates as well as high emitter densities. In multicolor studies, and particularly in PAINT studies, different affinities of the probes for their targets also affect the image quality of different targets. Therefore, the quantification of densely packed membrane components using SMLM techniques may not always be reliable.

1.2.2 Super-Resolution Optical Fluctuation Imaging (SOFI)

Super-resolution optical fluctuation imaging (SOFI)[85] developed by Dertinger et al. generates nearly background-free high-contrast super-resolution images with a short acquisition time of around a few seconds. This method also requires the stochastic switching of the probe between two different emission states but uses higher-order statistical analysis to measure the

intensity fluctuations over time. Contrary to STORM or PALM, SOFI can be used when multiple probes are simultaneously emitting within a diffraction-limited area.[86,87] High-resolution SOFI images are constructed by using spatiotemporal cross-cumulants.[88] The brightness, concentration, and emitting state lifetimes can be extracted by analyzing several cumulant orders of the same data set.[89] Balanced SOFI (bSOFI) was used to quantify the distribution of CD4 glycoprotein and mutant variants in the plasma membrane of Jurkat T cells (Figure 3).[90] bSOFI-based cluster analysis calculations do not depend on molecular localization coordinates, nor any of the user-defined parameters that are required for SMLM-based cluster analysis. Also, bSOFI is not subject to measuring artificial clusters that arise in SMLM images due to multiple blinking events from the same probe. Although this method allows for a biased-free analysis of cluster formation, membrane dynamics cannot be revealed due to the need to image fixed cells.

Zhang and co-workers introduced photochromic SOFI (pcSOFI), which enables nanoscale imaging of events in live cells using the advantage of strong intensity fluctuations generated by reversible photochromic probes.[91] As a proof of concept for imaging cell membrane components, a protein that targets sphingolipid and cholesterol enriched microdomains (Lyn kinase protein) was tagged with Dronpa fluorescent protein and imaged using pcSOFI with ~120 nm resolution.[91] The same group recently introduced a new class of fluorescent biosensor for pcSOFI imaging called fluorescence fluctuation increase by contact (FLINC).[92] In these biosensors, the fluorescence fluctuation is controlled by the proximity of two fluorescent proteins. The resulting single molecule fluorescence fluctuations are recorded over time; then, the pcSOFI values at sub-pixel resolution are calculated using pair wise cross-cumulants with suitable pixel pairings. Nanoscale activity maps are generated using the collected pcSOFI values. This technique was used to image protein kinase A activity in nanodomains in the plasma

membrane of HeLa cells. Although the best reported resolution of SOFI techniques has not yet reached the levels achieved with PALM or STORM, fast image acquisition rates and the ability to use a wide range of fluorescent probes are advantages of SOFI techniques.

1.2.3 Stimulated Emission Depletion Microscopy (STED)

Similar to SMLM and SOFI techniques, STED is also a far-field super-resolution imaging technique that requires specific photophysical properties of the fluorescent probe.[93] STED was introduced by Hell and Wichmann in 1994. With reported lateral resolution levels better than 10 nm,[94-96] STED is a promising tool to study membrane components. In a STED experiment, the lateral resolution is improved by reversibly depleting the signal from fluorophores around the periphery of the observation spot. This requires two laser wavelengths. The excitation beam is spatially overlapped with a red-shifted doughnut-shaped depletion beam to eliminate spontaneous fluorescence from molecules within the doughnut profile. Only molecules within the center of the excitation profile contribute to the spontaneous fluorescence signal. When the laser beams are scanned over the sample (or vice versa), a subdiffraction image is produced. The axial resolution can also be improved with at least three different approaches: using a bottle-shaped focused beam to axially confine the fluorescence,[97] combining STED with 4Pi microscopy,[98] or combining STED with selective plane illumination microscopy.[99] The principles of STED microscopy and its biological applications have been broadly discussed.[100-102] The earliest applications of STED for imaging biological membranes include studies of membrane protein clusters, lipid nanodomains, and their interactions.[103-108] In a recent study, the spatial colocalization within the membrane of mortalin, a mitochondrial chaperon protein that is overexpressed in cancer, with the complement membrane attack complex C5b-9 was imaged with 35 nm lateral spatial resolution using two color STED.[109] As is common for many scanning imaging techniques, fixed cells (human leukemia cells) were

studied. The specific labeling of the target was achieved using antibodies, and the fluorescent probes were ATTO 594 and Abberior Star 635p. Both represent common classes of fluorophores used in STED imaging. Two excitation beams of 590 and 640 nm were used to simultaneously image the signal from ATTO 594 and Abberior Star 635p, respectively. A single depletion laser beam of 775 nm was suitable for both probes. Two acousto-optic modulators switched the excitation lasers sequentially, resulting in a quasi-simultaneous signal acquisition of two channels at the single pixel level. The resulting signal was spectrally resolved using dichroic mirrors and optical filters and was directed to two single photon counting devices. The ImageJ program "Linear unmixing" was used to remove the spectral cross-talk between the two detection channels.

STED was used by Shin et al. to image the fusion pore behaviors in live cell membranes.[110] Single-color, two-color and three-color STED imaging were achieved using a tunable white-light excitation laser and hybrid detectors. A 592 or 660 nm depletion beam was used depending on the probe. Scanning in both the lateral and axial directions generated STED images with ~60 nm lateral resolution and ~150-200 nm axial resolution.

Lang and co-workers used STED microscopy to determine the packing density of the Alzheimer's disease-related amyloid precursor protein on fixed neuron-like human cell membranes.[111] Amyloid precursor protein and membranes were labeled with antibody-coupled Alexa Fluor 594 and Fast-DiO, respectively. They found that most amyloid precursor proteins that are associated with the plasma membrane are organized into structures containing 20 to 30 molecules confined within a region of 65 to 85 nm in diameter. Nine amyloid precursor proteins were measured per micrometer squared. The same group studied syntaxin 1A protein clustering on human liver cancer cell (HepG2) membranes using

continuous wave and pulsed STED techniques (Figure 4).[112] They identified a hierarchy in membrane protein clustering, where "loose" clustering is due to the forces acting on the transmembrane segment and "tight" clustering is due to cytoplasmic interactions. They also reported that the size of the protein cluster does not necessarily scale with the number of proteins it contains.

The combination of STED with fluorescence correlation spectroscopy (STED FCS) can analyze a wide range of dynamic membrane processes with improved spatial resolution (Figure 4). Typically, the analyzed area in a FCS experiment is diffraction limited. In STED FCS, the fluctuations in fluorescence intensity are detected and statistically analyzed to study the diffusion properties or binding interactions of the fluorescent species within a subdiffraction volume. The analyzed area is reduced to a few or tens of nanometers. This allows nanoscale heterogeneities to be measured that would otherwise be averaged out of a confocal analysis volume. Lipid dynamics have been measured in model membranes using STED FCS[113] and gated STED FCS wherein the detected signal is time-gated to optimize the spatial resolution.[114] Time-correlated-single-photon-counting photon filtering removes the background that is produced from incomplete depletion within the doughnut profile and enhances the spatial resolution. The molecular organization and the diffusion properties of fluorescent lipid analogs and glycophosphatidylinositol-anchored proteins in live PtK2 or CHO cell membranes and cell-derived giant plasma membrane vesicles (GPMVs) were analyzed using STED FCS.[115]

STED has also been coupled with scanning FCS (sSTED FCS) by Bizzarri and co-workers.[116] In this combination technique, the signal was rapidly recorded along a line or a circle. Heterogeneity in lipid and protein diffusion was mapped with sSTED FCS in live cell membranes with 60 nm spatial resolution and submillisecond temporal resolution. This method

has advantages over single-point STED FCS because molecular trajectories can be simultaneously detected at different positions on the membrane, and heterogeneous behaviors can be measured with nanoscale resolution. Moreover, single point FCS measurements require precise knowledge of the analysis volume to obtain accurate diffusion properties, whereas scanning FCS overcomes this requirement. Fluorophore photobleaching and background are also problematic in single point STED FCS experiments, but the faster dwell times of scanning FCS reduce the photobleaching that may lead to false diffusion properties.[117] A disadvantage of sSTED FCS also comes from the faster dwell times per pixel, which leads to decreased signal-to-noise ratios in the correlation curve. The method, however, was shown by Eggeling and co-workers to be suitable to measure the diffusion dynamics of fluorescently labeled phospholipids, cholesterol, and sphingolipids in PtK2 cell membranes.[118] The spatiotemporal mapping of Atto647N-labeled phosphatidylethanolamine and sphingomyelin in PtK2 cell membranes as well as the quantification of cholesterol dynamics in different cell lines as a function of growth time were also measured using sSTED FCS.[119] Additionally, the dynamics of Atto647N-labeled sphingomyelin and phosphatidylethanolamine in Cos-7 cell membranes were mapped.[117] The authors report there was a lot of heterogeneity in the signal measured between and within cells, which was not captured by other STED FCS techniques, and that the inversely correlated diffusion coefficient and local dye concentration were an indicator that the lipid species become temporally trapped, for example, by the glass substrate on which the cells were spread or an unknown cellular component.

In contrast to SMLM techniques that require a series of images to be collected over time, fast data acquisition rates have been reported with STED. In a STED experiment, neither postimage processing nor special imaging buffers are required. While the high laser irradiances

generally limit the choice of fluorophore to the most photostable fluorophores, there is a wide selection of excitation wavelengths available for STED. Live cell membrane imaging is possible using lower irradiances, generally at the expense of spatial resolution. Continuous wave STED enables fast imaging and is thus suitable for live cells, but the achievable resolution is limited compared to pulsed STED when using the same irradiance. Overall, the STED instrumentation is more complicated than most SMLM setups.

1.2.4 Super-Resolution Structured Illumination Microscopy (SR-SIM)

SR-SIM is a wide-field imaging technique that uses a structured pattern of the illumination light to excite the florophores in the sample. An overlay of two grids with different mesh sizes or at various angles generates moirè fringes that reveal subdiffraction spatial information. Using nonlinear responses, resolution lower than 100 nm is achieved. The sample preparation methods used with standard imaging techniques are compatible with SR-SIM, and any fluorophore with reasonable resistivity to photobleaching is suitable. SR-SIM is also suitable for live cell imaging due to its use of relatively low excitation irradiances and fast imaging capabilities. Multicolor imaging of up to four colors has been reported.[120] Several studies have reported the use of SR-SIM to evaluate the relationship between the plasma membrane organization and cytoskeleton components.[121-125]

SR-SIM was also combined with other super-resolution imaging techniques such as SMLM to study biological membranes. STORM imaging results in a better spatial resolution than SIM, but SIM avoids the clustering artifacts in STORM images. SIM combined with STORM imaged the distribution of T-cell receptors in lymph nodes (Figure 5)[126] and acetylcholine receptors in postsynaptic membranes.[127] In the latter study, Alexa Fluor 647 was used to label the acetylcholine receptors and 3D-SIM was used to identify their stripe-like distribution pattern at the neuromuscular junctions. The enhanced resolution of STORM imaging

revealed the receptor localization around the openings of junction folds (invaginations of the postsynaptic muscle membrane). In another study, a combination of SMLM and SIM revealed the correlation of the flows of plasma membrane and cortical actin in live T-cell synapses.[121] The nanoscale actin distribution was imaged in fixed cells using SMLM. Dual-color live-cell SIM images using a spatial light modulator to produce the structured illumination pattern were collected in TIRF mode. The SIM image series was analyzed using spatio-temporal image correlation spectroscopy, which measures the diffusion properties as well as the velocity vectors (magnitude and direction) of the imaging target.

Instant structured illumination microscopy (iSIM) improves the spatial resolution compared to diffraction-limited imaging without affecting the temporal resolution and enables dynamic events to be imaged in live cells with higher acquisition speeds.[128] Information from excitation and emission point spread functions are optically combined to sharpen the image instantly. TIRF combined with iSIM was used to image plasma membrane components in U2OS cells with ~115 nm lateral resolution and with frame rates up to 100 Hz.[129]

SR-SIM techniques are superior to SMLM or STED techniques for live cell imaging when low light irradiances and fast imaging speeds are required. This technique, however, has not yet reached the spatial resolution that can be achieved with SMLM or STED techniques. Ongoing advances such as fast detectors, superior adaptive optics, and advanced image reconstruction algorithms are expected to improve the resolution to a level that is suitable for imaging many dynamic membrane events on the nanoscale.

1.2.5 Fluorescent Probes for Membrane Studies

The photophysical properties of probes play a major role in the quality of a fluorescence image. Genetically encoded fluorescent protein labels are widely used, although the fluorescent protein may affect the natural function and/or dynamics of the biomolecule. The resulting data

may not represent the properties of the endogenous pool of biomolecules. Immunolabeling with fluorescently labeled antibodies targets specific membrane components, such as receptors, but this requires an available antibody to the target. Epitope tags (e.g., His, HA, FLAG, c-Myc) with the antibody corresponding to the tag are useful to label a specific target. They do not require a specific antibody for each membrane component, but genetically encoded epitope tags also eliminate the possibility of studying endogenous components. Nile red, Laurdan, DiI, DiD, DiO, and fluorescent lipid analogs are widely used lipid mimetic probes for imaging membrane lipids. While these conventional probes are generally useful for imaging biological membranes, new minimally invasive membrane probes with targeting specificity are needed. In addition to the specific photophysical properties required for each super-resolution imaging technique, membrane targeting probes should have solubility in imaging buffers, photostability to ensure imaging for long analysis times without signal loss, low toxicity, and biocompatibility. A range of emission wavelengths is also desirable for multicolor imaging.

Several novel probes were recently introduced to image the lipid fraction of biological membranes. A permeabilization-tolerant membrane imaging probe was developed by linking three species: cholesterol-polyethylene glycol, fluorescein isothiocyanate, and amine-rich glycol chitosan.[130] This probe was used to simultaneously image cell membranes with intracellular components in fixed cells. N-[[40-N,N-Diethylamino-3-hydroxy-6-flavonyl]-methyl]-N-methyl-N-(3-sulfopropyl)-1-dodecanaminium was synthesized as an environment sensitive probe.[131] This probe had dual emission peaks based on the lipid order in its surrounding environment; thus, it can be used as a ratiometric probe for imaging the ordered and disordered lipid domains in membranes. A two-photon activatable red emitting styrylpyridine-based small molecule rotor was developed to image cell membranes.[24] The membrane affinity of this probe is due to the

amphipathic nature of the molecule. The high membrane viscosity limits free molecular rotation and results in enhanced fluorescence, whereas fluorescence is low when the probe is outside the membrane.

Another newly developed membrane probe consisting of three linked components: cholesterol, phospho-D-thyrosine, and 4-nitro-2,1,3-benzoxadiazole fluorophore, was used to image the real time dynamics of cell membranes.[132] GPI-anchored enzymes in lipid rafts activate the probe by cleaving the phosphate group, and the activated probes self-assemble on the plasma membrane. A membrane-targeting two-photon-excitable nitric-oxide probe was developed by attaching a quaternary ammonium compound and a long alkyl chain into 4-amino-1,8-naphthalimide.[133] This bipolar structure is specifically localized in the plasma membrane. Initially, it has a negligible fluorescence, but upon binding with nitric oxide, its fluorescence is enhanced. Jiao and co-workers developed a conformationally induced off-on probe by linking hexamethylenediamine with sunitinib and pyrene to target and image the tyrosine kinase receptor protein in cell membranes.[134] The TLSHalo probe was developed to image the potassium ion transportation in cell membranes.[135] This probe specifically targets Halo-tag expressing proteins on the cell membrane and is fluorescent upon binding with potassium; the reported selectivity over sodium is high.

Fluorescent conjugated-polymer nanoparticles have advantages as imaging probes due to their high quantum yield, photostability, biocompatibility, and ease of surface modification. Although for some applications, their larger size may alter the membrane properties. Conjugated polymer nanoparticles with poly(fluorene-co-phenylene) linked to the drug plerixafor were used to target CXCR4, a G protein-coupled receptor in the cell membrane.[136] The blue-emitting nanoparticles showed good water solubility, selective membrane targeting, and a low toxicity

that is suitable for live cell membrane imaging. Red-emitting conjugated-polymer nanoparticles with two photon absorptivity were also developed as membrane probes.[137] The membrane selectivity is due to the hydrophobic interactions of the polymer's aliphatic chains with membrane lipids. A cationic polythiophene derivative, poly((3-((4-methylthiophen-3-yl)oxy)propyl)triphenylphosphonium chloride) was introduced as an imaging agent for adenosine triphosphate in cell membranes.[138] Qian and co-workers developed lectin-functionalized lanthanide-doped upconversion nanoparticles to image the glycan molecules within the cell membrane.[139] They used this probe to identify cancer cells by imaging the glycan distribution pattern in cell membrane. Gold nanoparticles bioconjugated with rationally designed peptides were developed for integrin selective imaging on cell membrane.[140] This probe is excitable with two photons and enables the quantification of integrin expression on the cell membrane. Semiconductor quantum dots labeled with phenylboronic acid were developed as imaging probes to detect sialic acids in membranes.[141] This probe enabled the imaging of sialylated glycoproteins in live PC12 cell membranes. These novel probes that report on a specific endogenous membrane component or membrane function are promising for future use with super-resolution imaging techniques.

1.3 Raman Imaging

Raman imaging is a chemically specific label-free technique that allows the simultaneous imaging of multiple membrane components. The fundamental details of Raman scattering as well as the previous applications of Raman techniques for biomaterial analysis,[142] including membranes and lipid-rich organelles, have been previously discussed.[143] The low cross section of spontaneous Raman scattering, and the resulting weak signals, generally mean that signal enhancement techniques are required in order to image membrane components at relevant

cellular concentrations. Surface-enhanced Raman spectroscopy (SERS) and tip-enhanced Raman spectroscopy (TERS) have been used to image cell membranes.

1.3.1 Surface-Enhanced Raman Spectroscopy (SERS)

In SERS, the Raman scattering is greatly enhanced for molecules in close contact with a nanostructured plasmonic substrate consisting of metals such as gold, silver, or copper. Since the membrane is the organelle in closest proximity when cells are spread on a SERS substrate, membrane selectivity can be achieved. SERS spectra of lipids, amino acids, and carbohydrates in live red blood cell membranes were recorded using nanoclustered silver as the plasmonic substrate (Figure 6).[144] Raman peaks corresponding to membrane components could not be identified by spontaneous Raman spectroscopy due to the large signal from bulk hemoglobin within the cell. Fogarty et al. suggest spectral mapping of the endothelial plasma membrane with a silver-intensified gold plasmonic substrate (gold-core silver-shell nanoparticles) showed evidence of a heterogeneous distribution of membrane components.[145] The positively charged gold plasmonic nanoparticles were linked with the net negatively charged glycocalyx (the glycoprotein and glycolipid enriched covering around the endothelial cell membrane) and were evenly distributed across the glycocalyx. A 100-fold signal enhancement of the spectral signal from the membrane was observed.

In order to image a specific membrane component with SERS, a targeting label must be added to the SERS substrate. Lipid raft membrane domains were imaged by incorporating a ring-opened alkyne steroid-analogue probe into the cell membrane.[146] This analogue formed microdomains that resemble the lipid rafts in membranes. Alkyne tags are commonly used because they have a unique Raman peak at ~2120 cm^{-1} and enable the imaging of biomolecules over long times with minimal effects on their intrinsic properties. Alkyne tags have also been used to image membrane proteins such as folate receptors and luteinizing hormone-releasing

hormone receptors in HeLa cells.[147,148] In these HeLa cell studies, 4-ethynylbenzenethiol derivatives were modified with various substituents to introduce the ability for multiplexed imaging. These alkyne reporters were encapsulated into polyallylamine-containing gold-silver nanoparticles with a thiol-gold bond. By incorporating the appropriate ligand, specific receptors were imaged.

In a recent study, wide-field Raman imaging was combined with SERS for bioimaging of phosphatidyl serine in human colon (LoVo) cell membranes.[149] The spatial resolution of wide-field Raman imaging was improved to 100 nm using standing-wave total-internal-reflection microscopy with narrow band-pass filters. Similar to the SIM technique discussed above, the spatial resolution was enhanced by using spatially patterned light to illuminate the sample. Total internal reflection mode reduced the illumination depth, which enhanced the signal-to-background ratio. SERS was used to enhance the Raman scattering. The SERS substrate consisted of a metal core coated with a polymer that was subsequently modified for covalent attachment of Annexin V antibody.

SERS enables imaging with enhanced signals compared to spontaneous Raman scattering, but the routine sensitivity is still not as good as what can be commonly achieved with fluorescence. Single molecule SERS experiments with biological membranes remain a challenge, and as a result, SERS measurements provide an average signal of many biomolecules. In addition, all molecules can potentially contribute to the Raman signal, so as mentioned previously, selective measurements often do require a label. Reproducible SERS measurements also remain a challenge to be solved. While many SERS measurements use low laser irradiances, photodamage of the SERS substrate or sample is still possible with prolonged acquisition times.[150-152]

1.3.2 Tip-Enhanced Raman Spectroscopy (TERS)

Tip-enhanced Raman spectroscopy (TERS) combines the chemical sensitivity of SERS and the nanoscale spatial resolution of scanning probe microscopies and permits molecular level imaging of membranes. Scanning probe techniques such as scanning tunneling microscopy, atomic force microscopy, sheer force microscopy, and scanning near-field optical microscopy have been used in TERS. The concept of TERS was introduced by Wessel in 1985.[153] In 2000, four groups independently reported TERS results that proved the applicability of the technique.[154-157] TERS uses focused laser illumination on a metal or metal-coated tip, which creates a localized, strongly enhanced electromagnetic field at the tip apex. While scanning the tip in close proximity to the sample (a separation distance equal to roughly the wavelength of light), enhanced Raman scattering is measured from molecules close to the tip. Spatial resolution in the tens of nanometer range or less is achieved. Multiple studies reported subnanometer spatial resolution with TERS.[158-160] The fundamentals of the technique and recent advances beyond the measurement of cell membranes are discussed in several reviews.[161-165] The earliest applications of TERS for membrane studies include imaging model cell membranes (i.e., lipid bilayers)[166-169] and bacterial[170,171] and viral surfaces.[172-174]

In a recent study using TERS, Gram positive and negative bacterial species were differentiated on the basis of the Raman signal of their membranes.[175] Gold nanoparticles with a 100 nm diameter were used at the apex of the TERS tip, and Raman data were collected with an upright microscope. The outer membrane of Gram negative bacteria consists of a lipid bilayer whereas the outer layer of Gram positive bacteria consists of a peptidoglycan cell wall. When the TERS tip was in contact with the Gram negative cell surface, the Raman signal was enhanced compared to the signal when the tip was out of contact. There was no difference in the ‘tip in’

and ‘tip out’ signals on Gram positive bacterial surfaces. Based on these spectral differences, Gram negative and positive bacterial types were distinguished.

Deckert and co-workers used TERS with silver-coated AFM tips to image plasma membrane components in human dermal-derived keratinocyte cells[167] and human colon cancer cells.[176] In the latter study, fixed cells were imaged with five second acquisitions to collect TERS data from up to a 270 × 162 nm area. Data collection was combined with multivariate data analysis to measure nanometer-sized lipid-and-protein-enriched domains in cell membranes. Lipid-enriched domains were measured primarily using phosphate bands and ranged from 10 × 40 nm to 20 × 20 nm in size, whereas protein enriched domains were measured using amide bands and were 10 × 30 nm to 30 × 70 nm in size. The exact protein composition within the domains could not be measured.

Alexander and Schultz imaged antibody-conjugated nanoparticles bound to fixed cell membranes using TERS.[177] A gold nanoparticle was also immobilized on the AFM tip and top illumination was used for TERS. In another study, the same group used ligand functionalized nanoparticles to chemically characterize $\alpha_v\beta_3$ integrins in the intact cell membrane of fixed human colon cancer cells using TERS.[178] The plasmonic interaction between the functionalized gold nanoparticle and the TERS tip selectively enhanced the amino acid signals from the nanoparticle-bound receptors on the membrane. Using the same technique, two integrin types on human colon cell membranes were identified and differentiated based on the spectral differences that result from slightly different ligand binding sites on these receptors (Figure 7).[179]

TERS is a valuable technique for measuring the nanoscale structure of the cell membrane; however, membranes are highly dynamic, and TERS studies have been limited to imaging fixed cells. Live-cell imaging may also be problematic due to the need for imaging

buffers. Emerging applications of TERS using a liquid medium[180-182] and improvements in the data acquisition speed by Van Duyne and co-workers[183] will make this technique a promising tool for imaging structural and dynamic events in live cell membranes.

1.3.3 Raman-Based Techniques being Developed for Membrane Studies

There are Raman techniques that are still in their infancy but have promise for providing both the chemical information inherent in Raman scattering and the spatial resolution of super-resolution fluorescence imaging. While SERS and TERS require the use of plasmonic materials in close contact with the sample, the emerging Raman techniques do not have this requirement. Therefore the sample preparation is easier, and the potential of altering the membrane structure and dynamics during the imaging process is limited.

Sub-diffraction femtosecond stimulated Raman spectroscopy

Nonlinear Raman spectroscopy such as coherent anti-Stokes Raman scattering spectroscopy (CARS) has been used for lipid bilayer studies. Frontiera and co-workers combined the concept of STED with nonlinear femtosecond stimulated Raman spectroscopy (FSRS) to achieve subdiffraction Raman imaging (Figure 8).[184] In this method, vibrational coherences in all Raman active modes are generated by overlapping two Gaussian-shaped picosecond and femtosecond beams. A doughnut-shaped decoherence pulse interferes with the FSRS signal and selectively eliminates the signal at the edge of the focal spot. The FSRS signal is generated only in the center where the decoherence beam has no intensity, which produces subdiffraction images. Bacteriorhodopsin proteins in purple membrane sheets isolated from *Halobacterium salinarum* were imaged as a proof-of-concept for imaging biological membranes. Ongoing advancements to this technique are promising, particularly those that allow the use of reduced laser irradiances and further improvements to the spatial resolution.

Total internal reflection (TIR) Raman spectroscopy

As with TIRF imaging, TIR Raman imaging provides signal from molecules within a couple hundred nanometers away from a substrate and can be used to provide enhanced signals from membrane components with a reduced contribution from the bulk of the cell. TIR Raman spectroscopy was first demonstrated by Ikeshoji and co-workers in 1973[185] using a carbon disulfide sample on a glass substrate. Under TIR, an evanescent wave with a decaying electric field is produced near the substrate. One to two orders of magnitude enhancement in the Raman signal may result from the enhanced electric field produced under TIR. Monolayer sensitivity has been achieved using various TIR Raman formats (Figure 9).[186-189] While the TIR enhancement is typically less than the SERS enhancement, the TIR Raman signal is very reproducible and well modeled and does not require a roughened metal substrate. Also, the TIR Raman signal is collected over a longer distance than is possible with SERS, so the entire membrane and associated cytoskeleton can be probed. In addition, by varying the incident angle of light, the distance over which the Raman signal is collected can be varied, and tens of nanometer axial resolution is possible.[190,191] To demonstrate the compatibility of this technique with biological samples, a thin layer of bovine serum was imaged with a high signal-to-noise ratio.[192] As a proof-of-concept for membrane studies, a model planar supported lipid layer was imaged with the TIR Raman technique.[193] In contrast to epi-illumination, the Raman signal of cells collected with TIR illumination is expected to reduce signals arising from cytosolic and nuclear compounds; thus, the plasma membrane could be imaged with a high signal-to-background ratio. While these developing Raman techniques are still in their infancy in regard to membranes studies, they are promising tools for future membrane studies.

1.4. Summary and Outlook

Biological membranes are highly heterogeneous and exhibit specific structural and dynamic properties that guide numerous cellular functions. Remarkable advances in optical techniques have enabled imaging with nanoscale spatial and fast temporal resolution. This review reports the advances in fluorescence and Raman-based nanoscale imaging techniques and their recent applications to study the organization and dynamics of biological membranes. Localization-based super-resolution techniques including PALM and STORM enable high spatial resolution generally at the cost of temporal resolution. In contrast, STED and SIM generally offer faster acquisition rates with lower spatial resolution. Raman imaging techniques reveal spatially resolved chemical information, although they have not yet reached the superior performance for membrane studies that has been demonstrated for fluorescence techniques.

Even with many recent advancements, membrane imaging has not yet been optimized to solve some of the most crucial questions related to membrane biology. These complex questions may not be addressed with a single imaging (or analytical) technique, and future developments in multimodal instrumentation are promising. For instance, whole cell studies using combinations of diffraction-limited and super-resolution imaging as well as optical imaging combined with nonoptical imaging, such as atomic force microscopy, electron microscopy, and mass spectroscopy, will enable information to be measured over multiple length, temporal, and chemical contrast scales. Of course, instrument developments, such as detectors with improved sensitivity, high quantum yields, larger pixel areas, and faster response, will enhance the temporal resolution and facilitate the capturing of fast membrane dynamics. Advances in analysis techniques will facilitate the fast and improved data processing and image generation and may eliminate the colocalization and clustering artifacts generated during the data processing, particularly in SMLM.

Improved sample preparation techniques and probes are also important for achieving the best imaging quality. The majority of the cell membrane components are sensitive to fixation procedures; thus, they may not be detected accurately in fixed cells. Fluorescent probes with high quantum yields, small size, good selectivity, and controllable photophysical properties also need continual development. Bright white-light lasers make it possible to provide a range of wavelengths for multicolor imaging, yet suitable spectrally resolved fluorophores, particularly those that report on a specific component or function, are not always available. Additional environmental sensitive fluorophores would be beneficial to image various membrane processes such as ion transportation, variances of pH, and electric potential.

Raman-based imaging approaches are commonly performed in fixed cell membranes due to lengthy imaging times (i.e., resulting from long acquisition times or scanning), which limits the dynamic information that can be measured. For the Raman techniques that have the best-reported spatial resolution to date, developing sensitive, reproducible, and biocompatible plasmonic SERS substrates and advances in TERS tip fabrication have the potential to provide selective imaging of single membrane components. Extension of TERS for compatibility with liquid medium would be highly advantageous for imaging membranes in live cells. Emerging Raman techniques may also be beneficial for noninvasively imaging biological membranes without the use of SERS substrates or TERS tips.

While the nature of the cell membrane may seem to not warrant the need for super-resolution 3D (three -dimensional) imaging techniques, they will permit the imaging of membrane processes and related intercellular signaling pathways as well as membrane topology and curvature. Visualization of the formation of exosomes from the cell membrane and their regulation by specific proteins is also possible. 3D optical methods are also helpful to image the

membrane interactions of adjacent cells and interactions with extracellular materials, for example, viral or bacterial pathogens.

Acknowledgements

This work is supported by funding from NSF grant CHE-1709099. The authors thank Qiaochu Zhu and Sadie Burkhow for useful discussion and assistance in preparing this manuscript.

1.5 References

1. Singer, S. J.; Nicolson, G. L. *Science* **1972**, *175*, 720-731.

2. Becker, W. *Journal of Microscopy* **2012**, *247*, 119-136.

3. Berezin, M. Y.; Achilefu, S. *Chemical Reviews* **2010**, *110*, 2641-2684.

4. Gagnon, E.; Connolly, A.; Dobbins, J.; Wucherpfennig, K. W. In *The Immune Synapse: Methods and Protocols*, Baldari, C. T.; Dustin, M. L., Eds.; Springer New York: New York, NY, 2017, pp 259-289.

5. King, C.; Wirth, D.; Workman, S.; Hristova, K. *Biochimica et Biophysica Acta (BBA) - Biomembranes* **2018**, *1860*, 2118-2125.

6. Lam, J. G. T.; Vadia, S.; Pathak-Sharma, S.; McLaughlin, E.; Zhang, X.; Swanson, J.; Seveau, S.; Bement, W. *Molecular Biology of the Cell* **2018**, *29*, 270-284.

7. Liu, Y.; Chen, L.-Y.; Zeng, H.; Ward, R.; Wu, N.; Ma, L.; Mu, X.; Li, Q.-L.; Yang, Y.; An, S.; Guo, X.-X.; Hao, Q.; Xu, T.-R. *The International Journal of Biochemistry & Cell Biology* **2018**, *99*, 114-124.

8. Ma, Y.; Yamamoto, Y.; Nicovich, P. R.; Goyette, J.; Rossy, J.; Gooding, J. J.; Gaus, K. *Nature Biotechnology* **2017**, *35*, 363-370.

9. Schihada, H.; Vandenabeele, S.; Zabel, U.; Frank, M.; Lohse, M. J.; Maiellaro, I. *Communications Biology* **2018**, *1*, 105, 1-8.

10. Khandelwal, N. K.; Sarkar, P.; Gaur, N. A.; Chattopadhyay, A.; Prasad, R. *Biochimica et Biophysica Acta (BBA) - Biomembranes* **2018**, *1860*, 2308-2319.

11. Kingsley, J. L.; Bibeau, J. P.; Mousavi, S. I.; Unsal, C.; Chen, Z.; Huang, X.; Vidali, L.; Tüzel, E. *Biophysical Journal* **2018**, *114*, 1153-1164.

12. Lorén, N.; Hagman, J.; Jonasson, J. K.; Deschout, H.; Bernin, D.; Cella-Zanacchi, F.; Diaspro, A.; McNally, J. G.; Ameloot, M.; Smisdom, N.; Nydén, M.; Hermansson, A.-M.; Rudemo, M.; Braeckmans, K. *Quarterly Reviews of Biophysics* **2015**, *48*, 323-387.

13. Ono, J.; Fushimi, S.; Suzuki, S.; Ameno, K.; Kinoshita, H.; Shirakami, G.; Kabayama, K. *FEBS Open Bio* **2018**, *8*, 1127-1134.

14. Zhang, M.; Zhang, Z.; He, K.; Wu, J.; Li, N.; Zhao, R.; Yuan, J.; Xiao, H.; Zhang, Y.; Fang, X. *Analytical Chemistry* **2018**, *90*, 4282-4287.

15. Carlo, M.; Maria, F. G.-P. *Reports on Progress in Physics* **2015**, *78*, 124601, 1-29.

16. Shen, H.; Tauzin, L. J.; Baiyasi, R.; Wang, W.; Moringo, N.; Shuang, B.; Landes, C. F. *Chemical Reviews* **2017**, *117*, 7331-7376.

17. Krieger, J. W.; Singh, A. P.; Bag, N.; Garbe, C. S.; Saunders, T. E.; Langowski, J.; Wohland, T. *Nature Protocols* **2015**, *10*, 1948-1974.

18. Macháň, R.; Wohland, T. *FEBS Letters* **2014**, *588*, 3571-3584.

19. Lucarelli, S.; Delos Santos, R. C.; Antonescu, C. N. *Methods Mol Biol* **2017**, *1652*, 191-225.

20. Greitzer-Antes, D.; Xie, L.; Qin, T.; Xie, H.; Zhu, D.; Dolai, S.; Liang, T.; Kang, F.; Hardy, A. B.; He, Y.; Kang, Y.; Gaisano, H. Y. *J Biol Chem* **2018**, *293*, 6893-6904.

21. Goudsmits, J. M. H.; van Oijen, A. M.; Slotboom, D. J. *Methods Enzymol* **2017**, *594*, 101-121.

22. Tanaka, H.; Fujii, S.; Hirano, T. *Nat Protoc* **2014**, *9*, 76-89.

23. Kisler, K.; Dominguez, R. *Methods Mol Biol* **2016**, *1366*, 175-187.

24. Guo, L.; Zhang, R.; Sun, Y.; Tian, M.; Zhang, G.; Feng, R.; Li, X.; Yu, X.; He, X. *Analyst* **2016**, *141*, 3228-3232.

25. Thal, L. B.; Tomlinson, I. D.; Quinlan, M. A.; Kovtun, O.; Blakely, R. D.; Rosenthal, S. J. *ACS Chem Neurosci* **2018**, DOI: 10.1021/acschemneuro.8b00350.

26. Hirama, T.; Das, R.; Yang, Y.; Ferguson, C.; Won, A.; Yip, C. M.; Kay, J. G.; Grinstein, S.; Parton, R. G.; Fairn, G. D. *J Biol Chem* **2017**, *292*, 14292-14307.

27. Yeow, I.; Howard, G.; Chadwick, J.; Mendoza-Topaz, C.; Hansen, C. G.; Nichols, B. J.; Shvets, E. *Curr Biol* **2017**, *27*, 2951-2962.

28. Ponjavic, A.; McColl, J.; Carr, A. R.; Santos, A. M.; Kulenkampff, K.; Lippert, A.; Davis, S. J.; Klenerman, D.; Lee, S. F. *Biophys J* **2018**, *114*, 2200-2211.

29. Aguet, F.; Upadhyayula, S.; Gaudin, R.; Chou, Y. Y.; Cocucci, E.; He, K.; Chen, B. C.; Mosaliganti, K.; Pasham, M.; Skillern, W.; Legant, W. R.; Liu, T. L.; Findlay, G.; Marino, E.; Danuser, G.; Megason, S.; Betzig, E.; Kirchhausen, T. *Mol Biol Cell* **2016**, *27*, 3418-3435.

30. Betzig, E.; Patterson, G. H.; Sougrat, R.; Lindwasser, O. W.; Olenych, S.; Bonifacino, J. S.; Davidson, M. W.; Lippincott-Schwartz, J.; Hess, H. F. *Science* **2006**, *313*, 1642-1645.

31. Hess, S. T.; Girirajan, T. P.; Mason, M. D. *Biophys J* **2006**, *91*, 4258-4272.

32. Rust, M. J.; Bates, M.; Zhuang, X. *Nat Methods* **2006**, *3*, 793-795.

33. Heilemann, M.; van de Linde, S.; Schüttpelz, M.; Kasper, R.; Seefeldt, B.; Mukherjee, A.; Tinnefeld, P.; Sauer, M. *Angewandte Chemie International Edition* **2008**, *47*, 6172-6176.

34. Shcherbakova, D. M.; Sengupta, P.; Lippincott-Schwartz, J.; Verkhusha, V. V. *Annual Review of Biophysics* **2014**, *43*, 303-329.

35. Mizuno, H.; Abe, M.; Dedecker, P.; Makino, A.; Rocha, S.; Ohno-Iwashita, Y.; Hofkens, J.; Kobayashi, T.; Miyawaki, A. *Chemical Science* **2011**, *2*, 1548-1553.

36. Owen, D. M.; Williamson, D. J.; Magenau, A.; Gaus, K. *Nature Communications* **2012**, *3*, 1256, 1-8.

37. Scarselli, M.; Annibale, P.; Radenovic, A. *Journal of Biological Chemistry* **2012**, *287*, 16768-16780.

38. Sengupta, P.; Jovanovic-Talisman, T.; Skoko, D.; Renz, M.; Veatch, S. L.; Lippincott-Schwartz, J. *Nature Methods* **2011**, *8*, 969-975.

39. Lillemeier, B. F.; Mörtelmaier, M. A.; Forstner, M. B.; Huppa, J. B.; Groves, J. T.; Davis, M. M. *Nature Immunology* **2009**, *11*, 90-96.

40. Gabor, K. A.; Kim, D.; Kim, C. H.; Hess, S. T. *PLOS ONE* **2015**, *10*, e0117225.

41. Hess, S. T.; Gould, T. J.; Gudheti, M. V.; Maas, S. A.; Mills, K. D.; Zimmerberg, J. *Proceedings of the National Academy of Sciences* **2007**, *104*, 17370-17375.

42. Annibale, P.; Vanni, S.; Scarselli, M.; Rothlisberger, U.; Radenovic, A. *PLOS ONE* **2011**, *6*, e22678.

43. Gabor, K. A.; Stevens, C. R.; Pietraszewski, M. J.; Gould, T. J.; Shim, J.; Yoder, J. A.; Lam, S. H.; Gong, Z.; Hess, S. T.; Kim, C. H. *PLOS ONE* **2013**, *8*, e68759.

44. Sherman, E.; Barr, V.; Manley, S.; Patterson, G.; Balagopalan, L.; Akpan, I.; Regan, Carole K.; Merrill, Robert K.; Sommers, Connie L.; Lippincott-Schwartz, J.; Samelson, Lawrence E. *Immunity* **2011**, *35*, 705-720.

45. Tobin, S. J.; Cacao, E. E.; Hong, D. W. W.; Terenius, L.; Vukojevic, V.; Jovanovic-Talisman, T. *PLOS ONE* **2014**, *9*, e87225.

46. Manley, S.; Gillette, J. M.; Patterson, G. H.; Shroff, H.; Hess, H. F.; Betzig, E.; Lippincott-Schwartz, J. *Nature Methods* **2008**, *5*, 155-157.

47. Heidbreder, M.; Zander, C.; Malkusch, S.; Widera, D.; Kaltschmidt, B.; Kaltschmidt, C.; Nair, D.; Choquet, D.; Sibarita, J.-B.; Heilemann, M. *Biochimica et Biophysica Acta (BBA) - Molecular Cell Research* **2012**, *1823*, 1984-1989.

48. Shrivastava, A.; Rodriguez, P.; Triller, A.; Renner, M. *Frontiers in Cellular Neuroscience* **2013**, *7*, 1-11.

49. Subach, F. V.; Patterson, G. H.; Renz, M.; Lippincott-Schwartz, J.; Verkhusha, V. V. *Journal of the American Chemical Society* **2010**, *132*, 6481-6491.

50. Dudok, B.; Barna, L.; Ledri, M.; Szabó, S. I.; Szabadits, E.; Pintér, B.; Woodhams, S. G.; Henstridge, C. M.; Balla, G. Y.; Nyilas, R.; Varga, C.; Lee, S.-H.; Matolcsi, M.; Cervenak, J.; Kacskovics, I.; Watanabe, M.; Sagheddu, C.; Melis, M.; Pistis, M.; Soltesz, I.; Katona, I. *Nature Neuroscience* **2014**, *18*, 75-76.

51. Gao, J.; Wang, Y.; Cai, M.; Pan, Y.; Xu, H.; Jiang, J.; Ji, H.; Wang, H. *Nanoscale* **2015**, *7*, 2511-2519.

52. Hartley, J. M.; Chu, T.-W.; Peterson, E. M.; Zhang, R.; Yang, J.; Harris, J.; Kopeček, J. *ChemBioChem* **2015**, *16*, 1725-1729.

53. Lee, J.; Sengupta, P.; Brzostowski, J.; Lippincott-Schwartz, J.; Pierce, S. K.; Lidke, D. *Molecular Biology of the Cell* **2017**, *28*, 511-523.

54. Lee, S. F.; Vérolet, Q.; Fürstenberg, A. *Angewandte Chemie International Edition* **2013**, *52*, 8948-8951.

55. Shelby, Sarah A.; Holowka, D.; Baird, B.; Veatch, Sarah L. *Biophysical Journal* **2013**, *105*, 2343-2354.

56. Truan, Z.; Tarancón Díez, L.; Bönsch, C.; Malkusch, S.; Endesfelder, U.; Munteanu, M.; Hartley, O.; Heilemann, M.; Fürstenberg, A. *Journal of Structural Biology* **2013**, *184*, 329-334.

57. Jiang, H.; English, B. P.; Hazan, R. B.; Wu, P.; Ovryn, B. *Angewandte Chemie International Edition* **2015**, *54*, 1765-1769.

58. Letschert, S.; Göhler, A.; Franke, C.; Bertleff-Zieschang, N.; Memmel, E.; Doose, S.; Seibel, J.; Sauer, M. *Angewandte Chemie International Edition* **2014**, *53*, 10921-10924.

59. Aaron, J. S.; Carson, B. D.; Timlin, J. A. *Small* **2012**, *8*, 3041-3049.

60. Chen, J.; Gao, J.; Wu, J.; Zhang, M.; Cai, M.; Xu, H.; Jiang, J.; Tian, Z.; Wang, H. *Nanoscale* **2015**, *7*, 3373-3380.

61. Maity, P. C.; Blount, A.; Jumaa, H.; Ronneberger, O.; Lillemeier, B. F.; Reth, M. *Science Signaling* **2015**, *8*, ra93, 1-15.

62. Wang, J.; Richards, D. A. *Biology Open* **2012**, *1*, 857-862.

63. Notelaers, K.; Rocha, S.; Paesen, R.; Swinnen, N.; Vangindertael, J.; Meier, J.; Rigo, J.-M.; Ameloot, M.; Hofkens, J. *Histochemistry & Cell Biology* **2014**, *142*, 79-90.

64. Ji, C.; Zhang, Y.; Xu, P.; Xu, T.; Lou, X. *Journal of Biological Chemistry* **2015**, *290*, 26978-26993.

65. Mattila, Pieta K.; Feest, C.; Depoil, D.; Treanor, B.; Montaner, B.; Otipoby, Kevin L.; Carter, R.; Justement, Louis B.; Bruckbauer, A.; Batista, Facundo D. *Immunity* **2013**, *38*, 461-474.

66. Owen, D. M.; Rentero, C.; Rossy, J.; Magenau, A.; Williamson, D.; Rodriguez, M.; Gaus, K. *Journal of Biophotonics* **2010**, *3*, 446-454.

67. Pageon, S. V.; Tabarin, T.; Yamamoto, Y.; Ma, Y.; Nicovich, P. R.; Bridgeman, J. S.; Cohnen, A.; Benzing, C.; Gao, Y.; Crowther, M. D.; Tungatt, K.; Dolton, G.; Sewell, A. K.; Price, D. A.; Acuto, O.; Parton, R. G.; Gooding, J. J.; Rossy, J.; Rossjohn, J.; Gaus, K. *Proceedings of the National Academy of Sciences* **2016**, *113*, E5454-E5463.

68. Shelby, S. A.; Veatch, S. L.; Holowka, D. A.; Baird, B. A.; Lippincott-Schwartz, J. *Molecular Biology of the Cell* **2016**, *27*, 3645-3658.

69. Stone, M. B.; Shelby, S. A.; Núñez, M. F.; Wisser, K.; Veatch, S. L. *eLife* **2017**, *6*, e19891.

70. Stone, M. B.; Veatch, S. L. *Nature Communications* **2015**, *6*, 7347, 1-9.

71. Williamson, D. J.; Owen, D. M.; Rossy, J.; Magenau, A.; Wehrmann, M.; Gooding, J. J.; Gaus, K. *Nature Immunology* **2011**, *12*, 655-663.

72. Bernhem, K.; Blom, H.; Brismar, H. *PLoS One* **2018**, *13*, e0195825.

73. Liu, Q.; Chen, L.; Aguilar, H. C.; Chou, K. C. *Nat Commun* **2018**, *9*, 3050, 1-7.

74. Jonas, K. C.; Fanelli, F.; Huhtaniemi, I. T.; Hanyaloglu, A. C. *Journal of Biological Chemistry* **2015**, *290*, 3875-3892.

75. Peterson, J. A.; Wijesooriya, C.; Gehrmann, E. J.; Mahoney, K. M.; Goswami, P. P.; Albright, T. R.; Syed, A.; Dutton, A. S.; Smith, E. A.; Winter, A. H. *Journal of the American Chemical Society* **2018**, *140*, 7343-7346.

76. He, H.; Liu, X.; Li, S.; Wang, X.; Wang, Q.; Li, J.; Wang, J.; Ren, H.; Ge, B.; Wang, S.; Zhang, X.; Huang, F. *Anal Chem* **2017**, *89*, 11831-11838.

77. Sharonov, A.; Hochstrasser, R. M. *Proceedings of the National Academy of Sciences* **2006**, *103*, 18911-18916.

78. Giannone, G.; Hosy, E.; Levet, F.; Constals, A.; Schulze, K.; Sobolevsky, Alexander I.; Rosconi, M. P.; Gouaux, E.; Tampé, R.; Choquet, D.; Cognet, L. *Biophysical Journal* **2010**, *99*, 1303-1310.

79. Winckler, P.; Lartigue, L.; Giannone, G.; De Giorgi, F.; Ichas, F.; Sibarita, J.-B.; Lounis, B.; Cognet, L. *Scientific Reports* **2013**, *3*, 2387, 1-5.

80. Jungmann, R.; Steinhauer, C.; Scheible, M.; Kuzyk, A.; Tinnefeld, P.; Simmel, F. C. *Nano Letters* **2010**, *10*, 4756-4761.

81. Schnitzbauer, J.; Strauss, M. T.; Schlichthaerle, T.; Schueder, F.; Jungmann, R. *Nature Protocols* **2017**, *12*, 1198-1228.

82. Jayasinghe, I.; Clowsley, A. H.; Lin, R. S.; Lutz, T.; Harrison, C.; Green, E.; Baddeley, D.; Di Michele, L.; Soeller, C. *Cell Rep* **2018**, *22*, 557-567.

83. Werbin, J. L.; Avendaño, M. S.; Becker, V.; Jungmann, R.; Yin, P.; Danuser, G.; Sorger, P. K. *Scientific Reports* **2017**, *7*, 12150, 1-12.

84. Burgert, A.; Letschert, S.; Doose, S.; Sauer, M. *Histochemistry and Cell Biology* **2015**, *144*, 123-131.

85. Dertinger, T.; Colyer, R.; Iyer, G.; Weiss, S.; Enderlein, J. *Proceedings of the National Academy of Sciences* **2009**, *106*, 22287-22292.

86. Deschout, H.; Lukes, T.; Sharipov, A.; Szlag, D.; Feletti, L.; Vandenberg, W.; Dedecker, P.; Hofkens, J.; Leutenegger, M.; Lasser, T.; Radenovic, A. *Nature Communications* **2016**, *7*, 13693, 1-11.

87. Geissbuehler, S.; Dellagiacoma, C.; Lasser, T. *Biomed. Opt. Express* **2011**, *2*, 408-420.

88. Dertinger, T.; Colyer, R.; Vogel, R.; Enderlein, J.; Weiss, S. *Opt. Express* **2010**, *18*, 18875-18885.

89. Geissbuehler, S.; Bocchio, N. L.; Dellagiacoma, C.; Berclaz, C.; Leutenegger, M.; Lasser, T. *Optical Nanoscopy* **2012**, *1*, 4, 1-7.

90. Lukeš, T.; Glatzová, D.; Kvíčalová, Z.; Levet, F.; Benda, A.; Letschert, S.; Sauer, M.; Brdička, T.; Lasser, T.; Cebecauer, M. *Nature Communications* **2017**, *8*, 1731, 1-7.

91. Dedecker, P.; Mo, G. C.; Dertinger, T.; Zhang, J. *Proc Natl Acad Sci U S A* **2012**, *109*, 10909-10914.

92. Mo, G. C.; Ross, B.; Hertel, F.; Manna, P.; Yang, X.; Greenwald, E.; Booth, C.; Plummer, A. M.; Tenner, B.; Chen, Z.; Wang, Y.; Kennedy, E. J.; Cole, P. A.; Fleming, K. G.; Palmer, A.; Jimenez, R.; Xiao, J.; Dedecker, P.; Zhang, J. *Nat Methods* **2017**, *14*, 427-434.

93. Hell, S. W.; Wichmann, J. *Opt Lett* **1994**, *19*, 780-782.

94. Gao, M.; Maraspini, R.; Beutel, O.; Zehtabian, A.; Eickholt, B.; Honigmann, A.; Ewers, H. *ACS Nano* **2018**, *12*, 4178-4185.

95. Rittweger, E.; Han, K. Y.; Irvine, S. E.; Eggeling, C.; Hell, S. W. *Nature Photonics* **2009**, *3*, 144-147.

96. Wildanger, D.; Patton, B. R.; Schill, H.; Marseglia, L.; Hadden, J. P.; Knauer, S.; Schönle, A.; Rarity, J. G.; O'Brien, J. L.; Hell, S. W.; Smith, J. M. *Advanced Materials* **2012**, *24*, OP309-OP313.

97. Arlt, J.; Padgett, M. J. *Opt. Lett.* **2000**, *25*, 191-193.

98. Dyba, M.; Hell, S. W. *Physical review letters* **2002**, *88*, 163901.

99. Friedrich, M.; Gan, Q.; Ermolayev, V.; Harms, Gregory S. *Biophysical Journal* **2011**, *100*, L43-L45.

100. Blom, H.; Widengren, J. *Chemical Reviews* **2017**, *117*, 7377-7427.

101. Vicidomini, G.; Bianchini, P.; Diaspro, A. *Nature Methods* **2018**, *15*, 173-182.

102. Roobala, C.; Ilanila, I. P.; Basu, J. K. *J Biosciences* **2018**, *43*, 471-484.

103. Milovanovic, D.; Honigmann, A.; Koike, S.; Göttfert, F.; Pähler, G.; Junius, M.; Müllar, S.; Diederichsen, U.; Janshoff, A.; Grubmüller, H.; Risselada, H. J.; Eggeling, C.; Hell, S. W.; van den Bogaart, G.; Jahn, R. *Nature Communications* **2015**, *6*, 5984, 1-10.

104. Sieber, J. J.; Willig, K. I.; Heintzmann, R.; Hell, S. W.; Lang, T. *Biophysical Journal* **2006**, *90*, 2843-2851.

105. Sieber, J. J.; Willig, K. I.; Kutzner, C.; Gerding-Reimers, C.; Harke, B.; Donnert, G.; Rammner, B.; Eggeling, C.; Hell, S. W.; Grubmüller, H.; Lang, T. *Science* **2007**, *317*, 1072-1076.

106. van den Bogaart, G.; Meyenberg, K.; Risselada, H. J.; Amin, H.; Willig, K. I.; Hubrich, B. E.; Dier, M.; Hell, S. W.; Grubmüller, H.; Diederichsen, U.; Jahn, R. *Nature* **2011**, *479*, 552-555.

107. Blom, H.; Rönnlund, D.; Scott, L.; Spicarova, Z.; Widengren, J.; Bondar, A.; Aperia, A.; Brismar, H. *BMC Neuroscience* **2011**, *12*, 16, 1-7.

108. Willig, K. I.; Rizzoli, S. O.; Westphal, V.; Jahn, R.; Hell, S. W. *Nature* **2006**, *440*, 935-939.

109. Mazkereth, N.; Rocca, F.; Schubert, J.-R.; Geisler, C.; Hillman, Y.; Egner, A.; Fishelson, Z. *Immunobiology* **2016**, *221*, 1395-1406.

110. Shin, W.; Ge, L.; Arpino, G.; Villarreal, S. A.; Hamid, E.; Liu, H.; Zhao, W.-D.; Wen, P. J.; Chiang, H.-C.; Wu, L.-G. *Cell* **2018**, *173*, 934-945.

111. de Coninck, D.; Schmidt, T. H.; Schloetel, J. G.; Lang, T. *Biophys J* **2018**, *114*, 1128-1141.

112. Merklinger, E.; Schloetel, J. G.; Weber, P.; Batoulis, H.; Holz, S.; Karnowski, N.; Finke, J.; Lang, T. *Elife* **2017**, *6*, e20705.

113. Sarangi, N. K.; Roobala, C.; Basu, J. K. *Methods* **2018**, *140-141*, 198-211.

114. Clausen, M. P.; Sezgin, E.; Bernardino de la Serna, J.; Waithe, D.; Lagerholm, B. C.; Eggeling, C. *Methods* **2015**, *88*, 67-75.

115. Schneider, F.; Waithe, D.; Clausen, M. P.; Galiani, S.; Koller, T.; Ozhan, G.; Eggeling, C.; Sezgin, E. *Mol Biol Cell* **2017**, *28*, 1507-1518.

116. Bianchini, P.; Cardarelli, F.; Luca, M. D.; Diaspro, A.; Bizzarri, R. *PLOS ONE* **2014**, *9*, e99619.

117. Benda, A.; Ma, Y.; Gaus, K. *Biophys J* **2015**, *108*, 596-609.

118. Honigmann, A.; Mueller, V.; Ta, H.; Schoenle, A.; Sezgin, E.; Hell, S. W.; Eggeling, C. *Nat Commun* **2014**, *5*, 5412, 1-12.

119. Maraspini, R.; Beutel, O.; Honigmann, A. *Methods* **2018**, *140-141*, 188-197.

120. Heintzmann, R.; Huser, T. *Chemical Reviews* **2017**, *117*, 13890-13908.

121. Ashdown, G. W.; Burn, G. L.; Williamson, D. J.; Pandžić, E.; Peters, R.; Holden, M.; Ewers, H.; Shao, L.; Wiseman, P. W.; Owen, D. M. *Biophysical Journal* **2017**, *112*, 1703-1713.

122. Bridges, A. A.; Jentzsch, M. S.; Oakes, P. W.; Occhipinti, P.; Gladfelter, A. S. *The Journal of Cell Biology* **2016**, *213*, 23-32.

123. Brown, A. C.; Oddos, S.; Dobbie, I. M.; Alakoskela, J. M.; Parton, R. M.; Eissmann, P.; Neil, M. A.; Dunsby, C.; French, P. M.; Davis, I.; Davis, D. M. *PLoS Biol* **2011**, *9*, e1001152.

124. Brown, A. C. N.; Dobbie, I. M.; Alakoskela, J.-M.; Davis, I.; Davis, D. M. *Blood* **2012**, *120*, 3729-3740.

125. Ashdown, G. W.; Owen, D. M. *Methods* **2018**, *140-141*, 112-118.

126. Hu, Y. S.; Cang, H.; Lillemeier, B. F. *Proceedings of the National Academy of Sciences* **2016**, *113*, 7201-7206.

127. York, A. L.; Zheng, J. Q. *eneuro* **2017**, *4*, e0232-17.

128. Curd, A.; Cleasby, A.; Makowska, K.; York, A.; Shroff, H.; Peckham, M. *Methods* **2015**, *88*, 37-47.

129. Guo, M.; Chandris, P.; Giannini, J. P.; Trexler, A. J.; Fischer, R.; Chen, J.; Vishwasrao, H. D.; Rey-Suarez, I.; Wu, Y.; Wu, X.; Waterman, C. M.; Patterson, G. H.; Upadhyaya, A.; Taraska, J. W.; Shroff, H. *Nature Methods* **2018**, *15*, 425-428.

130. Wang, H. Y.; Sun, J.; Xia, L. Y.; Li, Y. H.; Chen, Z.; Wu, F. G. *Acs Biomaterials Science & Engineering* **2017**, *3*, 2570-2578.

131. Kilin, V.; Glushonkov, O.; Herdly, L.; Klymchenko, A.; Richert, L.; Mely, Y. *Biophys J* **2015**, *108*, 2521-2531.

132. Wang, H.; Feng, Z.; Del Signore, S. J.; Rodal, A. A.; Xu, B. *J Am Chem Soc* **2018**, *140*, 3505-3509.

133. Zhang, X.; Wang, B.; Xiao, Y.; Wang, C.; He, L. *Analyst* **2018**, *143*, 4180-4188.

134. Jiao, Y.; Yin, J.; He, H.; Peng, X.; Gao, Q.; Duan, C. *J Am Chem Soc* **2018**, *140*, 5882-5885.

135. Hirata, T.; Terai, T.; Yamamura, H.; Shimonishi, M.; Komatsu, T.; Hanaoka, K.; Ueno, T.; Imaizumi, Y.; Nagano, T.; Urano, Y. *Anal Chem* **2016**, *88*, 2693-2700.

136. Li, M.; Nie, C.; Feng, L.; Yuan, H.; Liu, L.; Lv, F.; Wang, S. *Chemistry – An Asian Journal* **2014**, *9*, 3121-3124.

137. Liu, P.; Li, S.; Jin, Y.; Qian, L.; Gao, N.; Yao, S. Q.; Huang, F.; Xu, Q.-H.; Cao, Y. *ACS Applied Materials & Interfaces* **2015**, *7*, 6754-6763.

138. Huang, B.; Geng, Z.; Yan, S.; Li, Z.; Cai, J.; Wang, Z. *Anal Chem* **2017**, *89*, 8816-8821.

139. Zhang, W.; Peng, B.; Tian, F.; Qin, W.; Qian, X. *Anal Chem* **2014**, *86*, 482-489.

140. Gao, L.; Liu, M.; Ma, G.; Wang, Y.; Zhao, L.; Yuan, Q.; Gao, F.; Liu, R.; Zhai, J.; Chai, Z.; Zhao, Y.; Gao, X. *ACS Nano* **2015**, *9*, 10979-10990.

141. Liu, A.; Peng, S.; Soo, J. C.; Kuang, M.; Chen, P.; Duan, H. *Anal Chem* **2011**, *83*, 1124-1130.

142. Krafft, C.; Schmitt, M.; Schie, I. W.; Cialla-May, D.; Matthaus, C.; Bocklitz, T.; Popp, J. *Angew Chem Int Ed Engl* **2017**, *56*, 4392-4430.

143. Syed, A.; Smith, E. A. *Annu Rev Anal Chem (Palo Alto Calif)* **2017**, *10*, 271-291.

144. Zito, G.; Rusciano, G.; Pesce, G.; Dochshanov, A.; Sasso, A. *Nanoscale* **2015**, *7*, 8593-8606.

145. Fogarty, S. W.; Patel, II; Martin, F. L.; Fullwood, N. J. *PLoS One* **2014**, *9*, e106283, 1-7.

146. Yamaguchi, S.; Matsushita, T.; Izuta, S.; Katada, S.; Ura, M.; Ikeda, T.; Hayashi, G.; Suzuki, Y.; Kobayashi, K.; Tokunaga, K.; Ozeki, Y.; Okamoto, A. *Sci Rep* **2017**, *7*, 41007, 1-7.

147. Chen, Y.; Bai, X.; Su, L.; Du, Z.; Shen, A.; Materny, A.; Hu, J. *Sci Rep* **2016**, *6*, 19173, 1-12.

148. Chen, Y.; Ren, J. Q.; Zhang, X. G.; Wu, D. Y.; Shen, A. G.; Hu, J. M. *Anal Chem* **2016**, *88*, 6115-6119.

149. Chen, H. K.; Wang, S. Q.; Zhang, Y. Q.; Yang, Y.; Fang, H.; Zhu, S. W.; Yuan, X. C. *Opt Commun* **2017**, *402*, 221-225.

150. Etchegoin, P. G.; Lacharmoise, P. D.; Le Ru, E. C. *Anal Chem* **2009**, *81*, 682-688.

151. Kudelski, A.; Pettinger, B. *Chem Phys Lett* **2000**, *321*, 356-362.

152. Zhang, W.; Cui, X.; Yeo, B. S.; Schmid, T.; Hafner, C.; Zenobi, R. *Nano Lett* **2007**, *7*, 1401-1405.

153. Wessel, J. *J. Opt. Soc. Am. B* **1985**, *2*, 1538-1541.

154. Anderson, M. S. *Applied Physics Letters* **2000**, *76*, 3130-3132.

155. Hayazawa, N.; Inouye, Y.; Sekkat, Z.; Kawata, S. *Opt Commun* **2000**, *183*, 333-336.

156. Pettinger, B. P., G.; Schuster, R.; Ertl, G. . *Electrochemistry* **2000**, *68*, 942-949.

157. Stockle, R. M. S., Y. D.; Deckert, V.; Zenobi, R. . *Chem Phys Lett* **2000**, *318*, 131-136.

158. Kurouski, D.; Deckert-Gaudig, T.; Deckert, V.; Lednev, I. K. *Journal of the American Chemical Society* **2012**, *134*, 13323-13329.

159. Liao, M.; Jiang, S.; Hu, C.; Zhang, R.; Kuang, Y.; Zhu, J.; Zhang, Y.; Dong, Z. *Nano Letters* **2016**, *16*, 4040-4046.

160. Zhang, R.; Zhang, Y.; Dong, Z. C.; Jiang, S.; Zhang, C.; Chen, L. G.; Zhang, L.; Liao, Y.; Aizpurua, J.; Luo, Y.; Yang, J. L.; Hou, J. G. *Nature* **2013**, *498*, 82-86.

161. Gao, L.; Zhao, H.; Li, T.; Huo, P.; Chen, D.; Liu, B. *International Journal of Molecular Sciences* **2018**, *19*, 1193, DOI:10.3390/ijms19041193.

162. Kurouski, D. *Vibrational Spectroscopy* **2017**, *91*, 3-15.

163. Schmid, T.; Opilik, L.; Blum, C.; Zenobi, R. *Angewandte Chemie International Edition* **2013**, *52*, 5940-5954.

164. Xiao, L.; Schultz, Z. D. *Analytical Chemistry* **2018**, *90*, 440-458.

165. Zhang, Z.; Sheng, S.; Wang, R.; Sun, M. *Analytical Chemistry* **2016**, *88*, 9328-9346.

166. Böhme, R.; Cialla, D.; Richter, M.; Rösch, P.; Popp, J.; Deckert, V. *Journal of Biophotonics* **2010**, *3*, 455-461.

167. Böhme, R.; Richter, M.; Cialla, D.; Rösch, P.; Deckert, V.; Popp, J. *Journal of Raman Spectroscopy* **2009**, *40*, 1452-1457.

168. Nakata, A.; Nomoto, T.; Toyota, T.; Fujinami, M. *Analytical Sciences* **2013**, *29*, 865-869.

169. Opilik, L.; Bauer, T.; Schmid, T.; Stadler, J.; Zenobi, R. *Physical Chemistry Chemical Physics* **2011**, *13*, 9978-9981.

170. Neugebauer, U.; Rösch, P.; Schmitt, M.; Popp, J.; Julien, C.; Rasmussen, A.; Budich, C.; Deckert, V. *ChemPhysChem* **2006**, *7*, 1428-1430.

171. Neugebauer, U.; Schmid, U.; Baumann, K.; Ziebuhr, W.; Kozitskaya, S.; Deckert, V.; Schmitt, M.; Popp, J. *ChemPhysChem* **2007**, *8*, 124-137.

172. Cialla, D.; Deckert-Gaudig, T.; Budich, C.; Laue, M.; Möller, R.; Naumann, D.; Deckert, V.; Popp, J. *Journal of Raman Spectroscopy* **2009**, *40*, 240-243.

173. Hermann, P.; Hermelink, A.; Lausch, V.; Holland, G.; Möller, L.; Bannert, N.; Naumann, D. *Analyst* **2011**, *136*, 1148-1152.

174. Olschewski, K.; Kämmer, E.; Stöckel, S.; Bocklitz, T.; Deckert-Gaudig, T.; Zell, R.; Cialla-May, D.; Weber, K.; Deckert, V.; Popp, J. *Nanoscale* **2015**, *7*, 4545-4552.

175. Berezin, S.; Aviv, Y.; Aviv, H.; Goldberg, E.; Tischler, Y. R. *Scientific Reports* **2017**, *7*, 3810, DOI:10.1038/s41598-017-02212-2.

176. Richter, M.; Hedegaard, M.; Deckert-Gaudig, T.; Lampen, P.; Deckert, V. *Small* **2011**, *7*, 209-214.

177. Alexander, K. D.; Schultz, Z. D. *Analytical Chemistry* **2012**, *84*, 7408-7414.

178. Wang, H.; Schultz , Z. D. *ChemPhysChem* **2014**, *15*, 3944-3949.

179. Xiao, L.; Wang, H.; Schultz, Z. D. *Anal Chem* **2016**, *88*, 6547-6553.

180. Martín Sabanés, N.; Driessen, L. M. A.; Domke, K. F. *Analytical Chemistry* **2016**, *88*, 7108-7114.

181. Pienpinijtham, P.; Vantasin, S.; Kitahama, Y.; Ekgasit, S.; Ozaki, Y. *The Journal of Physical Chemistry C* **2016**, *120*, 14663-14668.

182. Touzalin, T.; Dauphin, A. L.; Joiret, S.; Lucas, I. T.; Maisonhaute, E. *Physical Chemistry Chemical Physics* **2016**, *18*, 15510-15513.

183. Klingsporn, J. M.; Sonntag, M. D.; Seideman, T.; Van Duyne, R. P. *The Journal of Physical Chemistry Letters* **2014**, *5*, 106-110.

184. Silva, W. R.; Graefe, C. T.; Frontiera, R. R. *ACS Photonics* **2016**, *3*, 79-86.

185. Ikeshoji, T.; Ono, Y.; Mizuno, T. *Appl. Opt.* **1973**, *12*, 2236-2237.

186. Lesoine, M. D.; Bobbitt, J. M.; Zhu, S.; Fang, N.; Smith, E. A. *Analytica Chimica Acta* **2014**, *848*, 61-66.

187. McKee, K. J.; Meyer, M. W.; Smith, E. A. *Analytical Chemistry* **2012**, *84*, 9049-9055.

188. McKee, K. J.; Meyer, M. W.; Smith, E. A. *Analytical Chemistry* **2012**, *84*, 4300-4306.

189. Nyamekye, C. K. A.; Weibel, S. C.; Bobbitt, J. M.; Smith, E. A. *Analyst* **2018**, *143*, 400-408.

190. McKee, K. J.; Smith, E. A. *Review of Scientific Instruments* **2010**, *81*, 043106, 1-6.

191. M., B. J.; A., S. E. *Journal of Raman Spectroscopy* **2018**, *49*, 262-270.

192. Iwamoto, R.; Ohta, K.; Miya, M.; Mima, S. *Appl. Spectrosc.* **1981**, *35*, 584-587.

193. Lee, C.; Bain, C. D. *Biochimica et Biophysica Acta (BBA) - Biomembranes* **2005**, *1711*, 59-71.

1.6 Figures

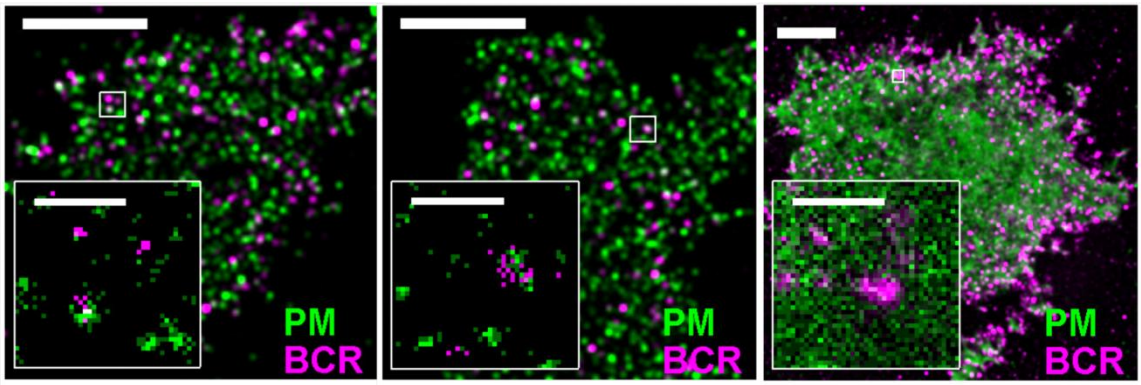

Figure 1.1 Two-color SMLM images collected using a combination of PALM and STORM showing the colocalization of B cell receptor clusters (magenta color) within ordered membrane domains (green color) in CH27 B cells. Images were collected using cells fixed (left) 1 min or (middle) 5 min after receptor clustering and (right) live cells. The receptor was labeled with an organic fluorophore, and receptors were clustered with a biotinylated anti-body followed by (multivalent) streptavidin binding. Ordered membrane domains were labeled with lipidated peptide anchored to the inner membrane leaflet (PM peptide) and mEos3.2 fluorescent protein. Cross-correlation analysis was used to show colocalization. Reproduced from Stone, M. B.; Shelby, S. A.; Núñez, M. F.; Wisser, K.; Veatch, S. L. Protein sorting by lipid phase-like domains supports emergent signaling function in B lymphocyte plasma membranes. *eLife* **2017**, *6*, e19891. (ref 69), with permission from Creative Commons Attribution license, copyright 2017.

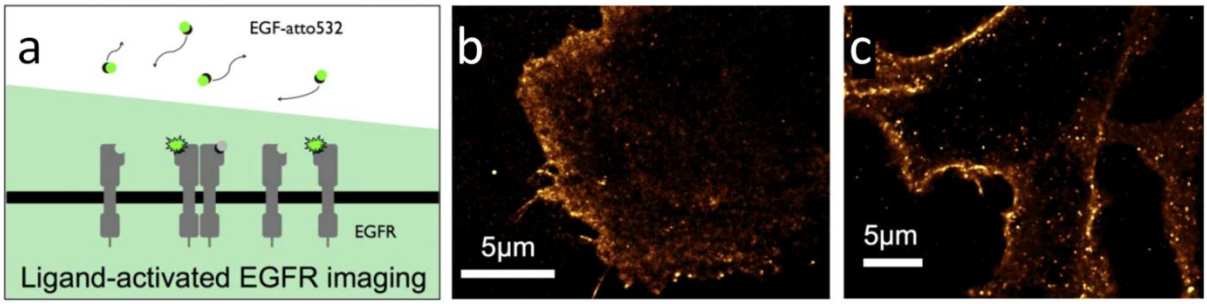

Figure 1.2 uPAINT super -resolution images of endogenous epidermal growth factor receptor (EGFR) in COS7 plasma membranes. (a) Schematic showing the principle behind signal generation from the stochastic binding and unbinding of a fluorescent species. Reconstructed images from (b) 1.6×10^5 localizations with simultaneous incubation with 0.4 nM EGF-Atto 532 ligand (shown in the schematic) or (c) fluorescently labeled ligand-binding-inhibitor panitumumab-Atto 647N. The illumination thickness (green shaded area in a) is approximately 2 μm. Reprinted with modifications by permission from Springer Nature: SCIENTIFIC REPORTS, Winckler, P.; Lartigue, L.; Giannone, G.; De Giorgi, F.; Ichas, F.; Sibarita, J.-B.; Lounis, B.; Cognet, L. Identification and super-resolution imaging of ligand-activated receptor dimers in live cells. *Scientific Reports* **2013** , *3* , 2387, 1−5 (ref 79). Copyright 2013.

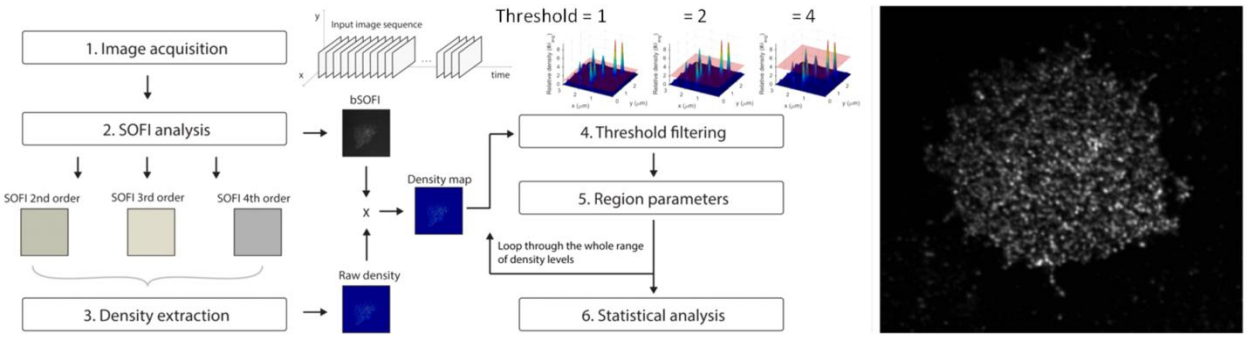

Figure 1.3 Representative steps in balanced SOFI data analysis using higher order statistics. First, a series of images of stochastically switching emitters is acquired in a similar fashion to SMLM experiments. The images are corrected for drift, for example using gold nanoparticle fiducial markers, which is problematic for super resolution imaging techniques that require collecting data over time with a microscope. The series of images is then divided into sub-series, each with a smaller number of frames than the total, which is necessary to account for photobleaching in the subsequent analysis. The SOFI analysis defines 2nd order and higher cumulants for each sub-series, the cumulants are averaged across each sub-series, and the averages are used to generate density maps that show the number of emitting fluorophores per pixel. Thresholds are applied to the density maps, and then regions of interest are analyzed for each threshold to define the number of "high density regions". The resultant image does not contain background and has a reduced noise level. The spatial resolution depends on the highest order cumulant, which can be increased with a larger data series consisting of more images (at the expense of collection time and additional photobleaching). At right is a bSOFI image collected with total internal reflection (TIRF) illumination showing CD4-mEos2 fusion protein clustering in a Jurkat T cell. Reprinted with modifications by permission from Macmillan Publishers Ltd: NATURE COMMUNICATIONS, Lukeš, T.; Glatzová, D.; Kvíčalová, Z.; Levet, F.; Benda, A.; Letschert, S.; Sauer, M.; Brdička, T.; Lasser, T.; Cebecauer, M., Nature Communications 2017, 8, 1731, 1-7 (Reference 90). Copyright 2017.

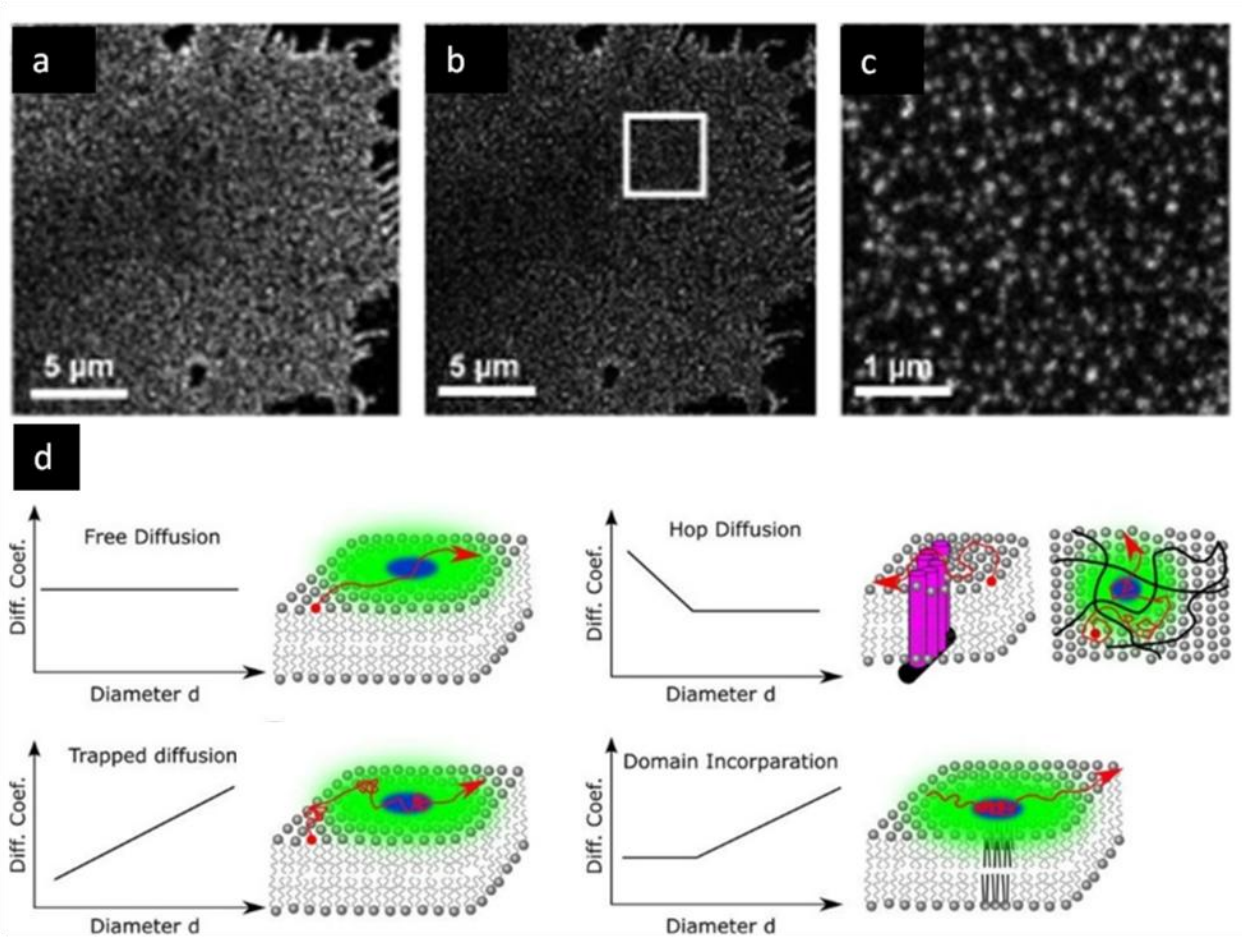

Figure 1.4 Examples of how STED can be used to measure (top) nanoscale organization of membrane components and (bottom) nanoscale dynamics. Syntaxin clusters imaged in the cell membrane of HepG2 cells using (a) confocal and (b) STED microscopy. Syntaxin is a SNARE protein that plays a role in vesicle fusion. (c) Magnified area of the white boxed area in image b. Reproduced from Merklinger, E.; Schloetel, J. G.; Weber, P.; Batoulis, H.; Holz, S.; Karnowski, N.; Finke, J.; Lang, T. The packing density of a supramolecular membrane protein cluster is controlled by cytoplasmic interactions. *Elife* **2017**, *6* , e20705 (ref 112),with permission from Creative Commons Attribution license, copyright 2017. (d) Information about membrane

dynamics can be measured using STED FCS wherein a region represented by the blue circle is analyzed. STED FCS reveals details about modes of membrane diffusion that are averaged or not measured by confocal imaging using a diffraction-limited imaging area represented by the green circle. When the diffusion coefficient is measured across analysis regions of varying size (i.e., diameters), Brownian “free” diffusion can be differentiated from diffusion associated with a transient immobile or slow species, hop diffusion that may result from, for example, membrane components that form compartments by anchoring to the actin cytoskeleton (black lines), and localization into a nanodomain that may be formed from different membrane compositions. The small analysis regions that are required to differentiate these modes of diffusion are generally not achieved with diffraction-limited imaging techniques,—but are generally achievable by STED. In STED FCS, the area of the analyzed region can be varied using different STED laser irradiances. Reproduced from Schneider, F.; Waithe, D.; Clausen, M. P.; Galiani, S.; Koller, T.; Ozhan, G.; Eggeling, C.; Sezgin, E. *Mol. Biol. Cell* **2017**, *28*, 1507−1518. (ref 115), with permission from Creative Commons Attribution license, copyright 2017.

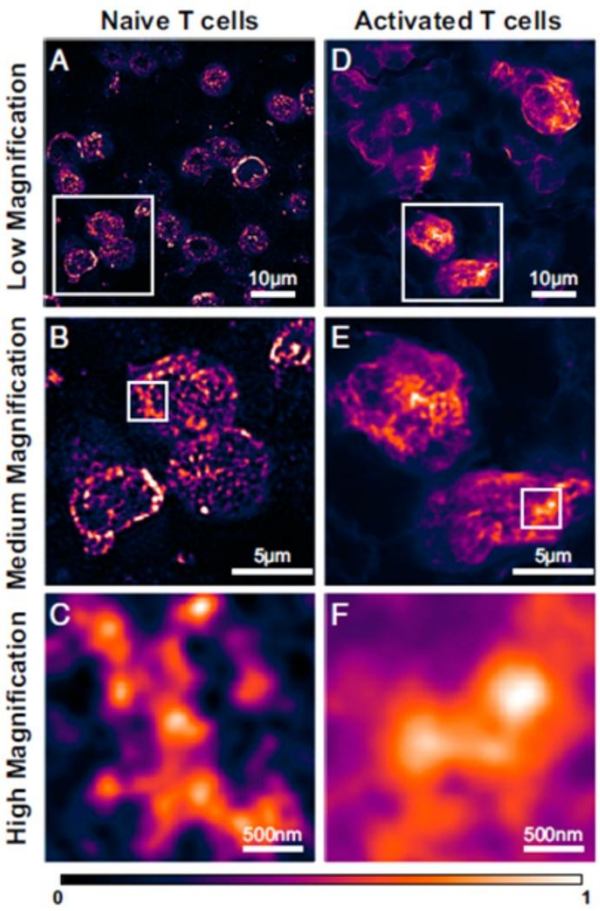

Figure 1.5 SIM images of the nanoscale distribution of the T-cell receptor in lymph-node-resident T cells. (A−C) before and (D−F) after in vivo T-cell activation. The images show that there is a change in the nanoscale organization after in vivo activation. B and E are magnified areas of the white boxes labeled in images A and D, respectively. Areas labeled with white boxes in B and E are enlarged in images C and F, respectively. The authors used SIM to ensure their reported SMLM images (specifically STORM) were not reporting artificial clusters, although the spatial resolution of the SIM images was not as good as what was achieved in STORM. Reproduced with permission from Proceedings of the National Academy of Sciences USA Hu, Y. S.; Cang, H.; Lillemeier, B. F. Superresolution imaging reveals nanometer- and micrometer-scale spatial distributions of T-cell receptors in lymph nodes. *Proceedings of the National Academy of Sciences* **2016**, *113*, 7201−7206 (ref 126). Copyright 2016 National Academy of Sciences of the United States of America.

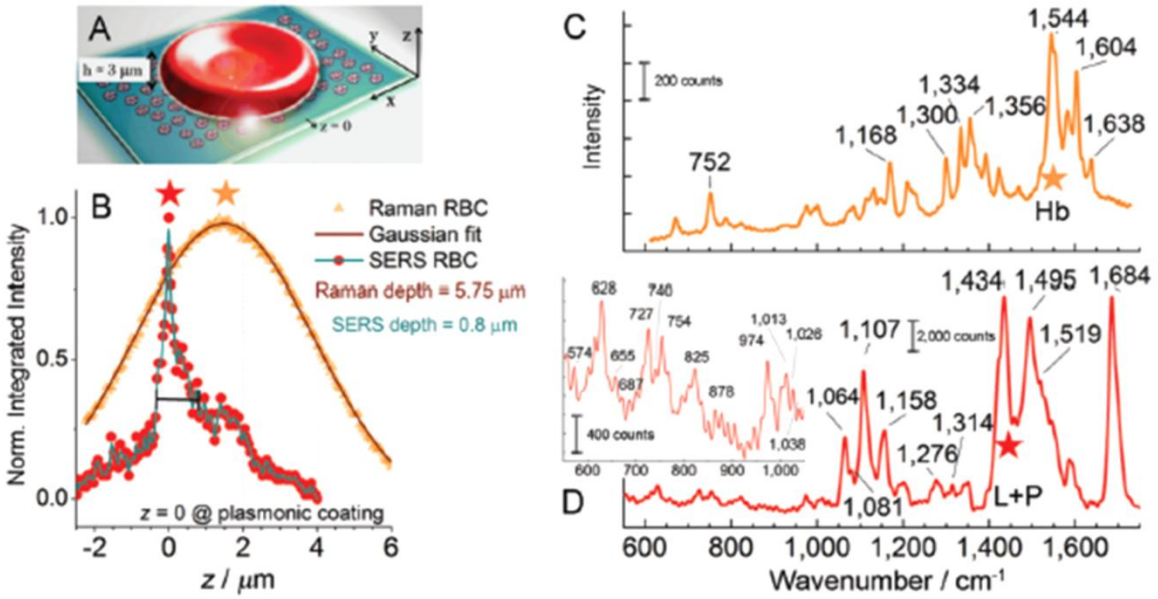

Figure 1.6 Comparison of membrane-selective SERS imaging and confocal Raman imaging. (A) An inverted confocal microscope was used to collect the Raman signal from red blood cells coated on a glass substrate (confocal) or SERS substrate. (B) The SERS signal measured molecules with a 0.8 μm focal depth, and provided better axial resolution and selectivity for the cell membrane compared to confocal Raman imaging. (C) The confocal Raman spectrum had peaks that are characteristic of intracellular species (i.e., hemoglobin) whereas the (D) SERS spectrum showed peaks that were characteristic of membrane lipids and also proteins. The laser irradiance was approximately 2 orders of magnitude lower, and the acquisition time was approximately 10-fold faster for the SERS measurement. Reproduced from Zito, G.; Rusciano, G.; Pesce, G.; Dochshanov, A.; Sasso, A. Surface-enhanced Raman imaging of cell membrane by a highly homogeneous and isotropic silver nanostructure. *Nanoscale* **2015**, *7*, 8593−8606 (ref 144), with permission of The Royal Society of Chemistry.

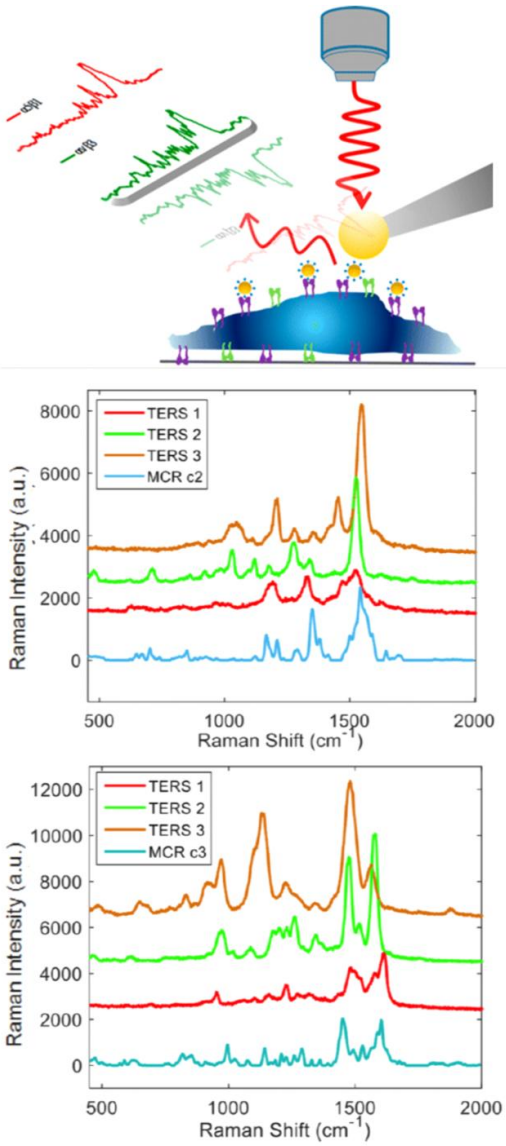

Figure 1.7 (Top) TERS measurements of two arginine−glycine−aspartate -binding integrin receptors (α5β1 and αvβ3) on fixed SW480 human colon cancer cells. The TERS tips consisted of a cyclo-(arginine−glycine−aspartic acid−phenylalanine−cysteine)-coated gold nanoparticle to tag the integrin receptors. Integrins were identified using multivariant curve resolution (MCR) analysis. The middle panel of extracted spectra corresponds to α5β1 integrin, and the bottom panel corresponds to αvβ3 integrin. Differences in the extracted spectra enable the selective imaging of these two different types of integrins. Reproduced with modifications from Xiao, L.; Wang, H.; Schultz, Z. D. *Anal. Chem.* **2016**, *88*, 6547−6553. (ref 179). Copyright 2016 American Chemical Society.

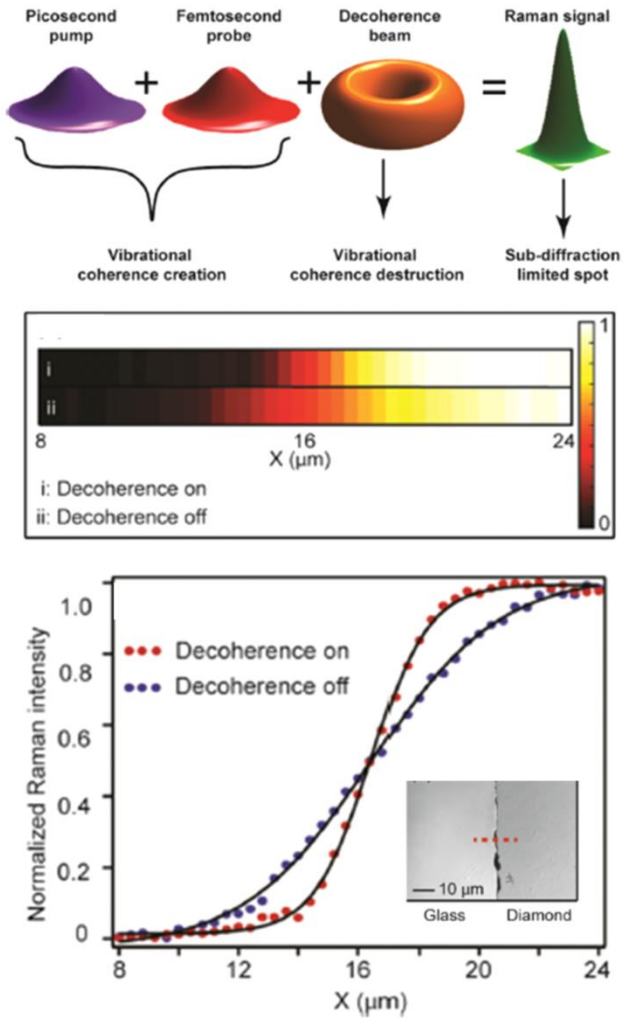

Figure 1.8 Femotsecond stimulated Raman spectroscopy (FSRS) imaging with a doughnut-shaped decoherence pulse to improve the spatial resolution. (Top) The picosecond pump and femtosecond probe pulses generate vibrational coherence and the FSRS signal. The coherence is removed around the periphery of the pump and probe pulses with a doughnut-shaped decoherence beam. The resulting FSRS signal is collected from a subdiffraction region. (Middle) The collected Raman signal from a diamond sample with a step edge with the decoherence beam (i) on or (ii) off. (Bottom) Signal cross sections showing that the spatial resolution is improved when the decoherence beam is on. The inset shows an optical image of the diamond sample with the step edge. Reproduced with modifications from Silva, W. R.; Graefe, C. T.; Frontiera, R. R. Toward Label-Free Super-Resolution Microscopy. *ACS Photonics* **2016**, *3*, 79−86 (ref 184). Copyright 2016 American Chemical Society.

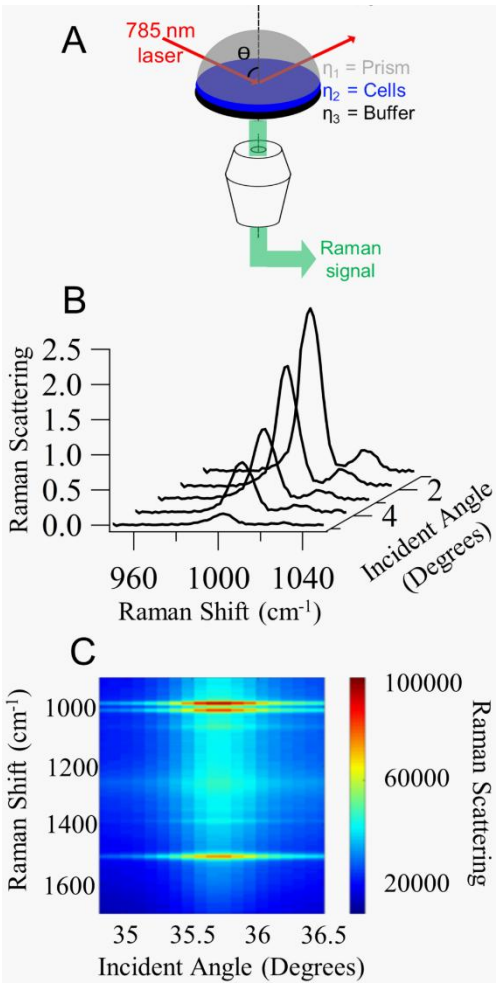

Figure 1.9 (A) A representative experimental setup of the total internal reflection illumination geometry wherein a laser propagates through a high refractive index material (η1) to a lower refractive index material (η2/η3) at an angle greater than the critical angle. Using a prism/sample interface allows a larger range of incident angles to be achieved compared to sending the laser through the microscope objective off the optical axis. Under total internal reflection conditions, Raman scattering is generated from molecules located within the evanescent wave that is confined to approximately the wavelength of light or less from the prism interface. (B) In scanning angle Raman imaging, the incident angle (θ) of light is scanned at angles above the critical angle while simultaneously collecting the Raman spectra. Different axial thicknesses can be measured by scanning the incident angle of light, as demonstrated using a homogeneous solution of benzonitrile to acquire Raman spectra at selected incident angles: (1) 37.47°, (2)

38.43°, (3) 41.31°, (4) 42.67°, and (5) 58.67°. With increasing incident angle, the Raman signal decreases due to the reduced volume over which the signal is collected from the homogeneous sample. Reprinted from McKee, K. J.; Smith, E. A., *Review of Scientific Instruments* **2010**, *81* (4), 043106 (ref 190), with the permission of AIP Publishing. Copyright 2010 The American Institute of Physics (AIP) Publishing. (C) Plot of the Raman signal as a function of Raman shift and incident angle for a self-assembled monolayer of thiophenol adsorbed on smooth planar gold film. The maximum Raman scattering intensity is observed at the surface plasmon resonance angle (35.56°), where surface plasmons are generated in the metal film and the reflected light is maximally attenuated. Reproduced from Nyamekye, C. K. A.; Weibel, S. C.; Bobbitt, J. M.; Smith, E. A. *Analyst* **2018**, *143* (2), 400−408 (ref 189), with permission of The Royal Society of Chemistry. Copyright 2018 The Royal Society of Chemistry.

CHAPTER 2. COUMARIN-BASED FLUORESCENT PROBES FOR SELECTIVELY TARGETING AND IMAGING THE ENDOPLASMIC RETICULUM IN MAMMALIAN CELLS

Modified from a manuscript published in Photochemistry and Photobiology

Chamari S. Wijesooriya[1], Megan Nieszala[2], Alex Stafford[2], Jake R. Zimmerman[2],

Emily A. Smith*[1]

[1] Department of Chemistry, Iowa State University, Ames, IA 50011, USA

[2] Department of Chemistry and Biochemistry, Ohio Northern University, Ada, OH 45810, USA

2.1 Abstract

Developing improved fluorescent probes for imaging the endoplasmic reticulum (ER) is necessary for structure-activity studies of this dynamic organelle. Two coumarin-based compounds with sulfonamide side groups were synthesized and characterized as ER-targeting probes. Their selectivity to target the ER in HeLa and GM07373 mammalian cells was shown with co-localization experiments using commercially available probes that localize in the ER, mitochondria, or lysozymes. The hydrophobicity of the coumarin-based probes was comparable to known probes that partition into the ER membrane. Their cytotoxity in mammalian cells was low with IC50 values that range from 205-252 μM. The fluorescent quantum yields of the coumarin-based probes when excited with 400 nm light were 0.60, and they have a much narrower emission spectrum (from 435-525 nm in methanol) than that of the only commercially available ER probe that is exited with 400 nm light (ER-Tracker™ Blue-White DPX). Thus, the coumarin-based probes are more useful for multicolor imaging with yellow and red emitting fluorophores. In addition to the above benefits, ER labeling was achieved with the coumarin-

based probes in both live cells and fixed cells, revealing their versatility for a wide range of cellular imaging applications.

2.2 Introduction

The endoplasmic reticulum (ER) is the largest organelle in most eukaryotic cells (*1*, *2*). It consists of a network of tubules and sacs enclosed with a continuous single lipid membrane that constitutes approximately half of the total area of lipid membranes in the cell (*3*). The ER plays a vital role in maintaining cellular processes, including posttranslational processing, folding and trafficking of proteins into other organelles (*4*) and synthesizing lipids (*5*). It is also responsible for stabilizing the intracellular calcium concentration (*6*). There are two structurally and functionally distinct components of the ER. Processes related to protein modification occur in the rough ER, which is a stacked sheet-like structure located in the perinuclear region of the cell. The smooth ER consists of a tubular component extending from the rough ER throughout the cytoplasm and is involved in lipid metabolism (*1*).

Several physiological conditions such as oxygen deficiency, altered glucose and calcium levels, excessive acidity as well as some pathological conditions can alter protein folding in the ER (*7*). This results in the accumulation of unfolded or misfolded proteins in the ER lumen and generates stress, which alters the size of the ER structure. Specially, the sheet-like structures expand (*8*). Visualizing this dynamic organelle is important to understand the relationship between its structure and biological activity (*9*).

Fluorescence imaging is a non-invasive and versatile technique for imaging cellular organelles, including the ER. The commercially available ER targeting probes (ER-Tracker™ Blue-White DPX, ER-Tracker™ Green/BODIPY™ FL Glibenclamide, and ER-Tracker™ Red/BODIPY™ TR Glibenclamide) shown in Figure **S1** contain the sulfonamide group in their

structures, and are targeted to the sulfonylurea receptors on the ER membrane (*10*). Several recently reported ER-targeting probes contain a sulfonamide linker attached to a fluorophore (*11-13*). Due to the lower cholesterol composition in the ER membrane (*14*), moderately lipophilic fluorescent probes such as ER Thermo Yellow (*15*) and BODIPY Nile Red (*16*) have been identified to selectively accumulate in the ER. Carbocyanine fluorophores such as DiOC6 and DiOC5 also have also been reported to target the ER membrane (*17*), but they are not selective for ER imaging because they are also retained in other cellular organelles (*18*). Developing ER probes emitting at different wavelengths is important for multicolor imaging (e.g., dual labeling). Among the currently available commercial ER probes, ER-Tracker™ Blue-White DPX is excited around 400 nm (*19, 20*). This probe, however, has a very broad emission profile ranging from 430-640 nm, and is not very useful for multicolor imaging with other fluorescent probes. Another disadvantage of commercial ER probes is their high cost due in part to their complex synthesis procedures.

Herein we introduce two coumarin-based compounds as ER-selective fluorescent probes (Figure **1**, Compound **1a** and **1b**). Previous studies showed that the methoxy group attached to the sulfonamido side group had a higher membrane permeability than the methyl group attached at the same position (*21*). Therefore, we studied compounds 1a and 1b with methyl and methoxy groups attached to the sulfonamide side group, respectively. The synthesis of the probes involves a simple two-step process based on an inverse-demand hetero-Diels-Alder reaction. The probe has low toxicity in HeLa and GM07373 mammalian cell lines. Its excitation is around 400 nm and it has a narrower emission range (from 435-525 nm in methanol) compared to ER-Tracker™ Blue-White DPX. These coumarin-based probes will be valuable imaging tools for tracking the

ER structure over time due to their selectivity, low cytotoxicity, bright emission in the blue region and the simple synthetic procedure.

2.3 Materials and Methods

2.3.1 Synthesis

7-Diethylamino-3-formylcoumarin, methyl trimethylsilyl dimethylketene acetal, sulfonamides and solvents were purchased from Sigma-Aldrich and Acros and used without further purification. 7-Diethylamino-3-formylcoumarin (**1**) (0.5 mmol), sulfonamide (0.6 mmol) (p-methyl or p-methoxy sulfonamide), pyridinium p-tolunesulfonate (PPTS) (0.1 mmol), molecular sieves (MS4Å), and toluene (5 mL) were added to a 25 mL round bottom flask. The flask was then equipped with a condenser, and the reaction was heated to reflux in an oil bath. After approximately 18-24 h the reaction was cooled to room temperature and then to 0 ˚C. The resulting bright red solid was filtered off and was then immediately transferred to a new 25 mL round bottom flask. Dichloromethane (2 mL) and THF (2 mL) were then added followed by methyl trimethylsilyl dimethylketene acetal (2.5 mmol) and $Y(OTf)_3$ (0.1 mmol). The reaction was stirred at room temperature for 20-30 min until it was deemed complete via monitoring by TLC. The reaction was quenched on a pad of silica (~1g), the solvent was evaporated and the crude mixture was purified via column chromatography (30% EtOAc/70% hexanes ramped to 100% ethyl acetate).

^{1}H-NMR were recorded on a Bruker Advance 400 MHz instrument (Figure **S2**). Chemical shifts are reported in parts per million (ppm) down field from TMS, using residual $CDCl_3$ (7.27 ppm) as an internal standard. Data are reported as follows: Chemical shift, multiplicity (s = singlet, d = doublet, t = triplet, q = quartet, m = multiplet, dd = doublet of doublet, bs = broad singlet), coupling constant and integration. ^{13}C-NMR was recorded on a

Bruker Advance 400 MHz (100 MHz) instrument using broadband proton decoupling (Figure **S3**). Chemical shifts are reported in parts per million (ppm) downfield from TMS, using the middle resonance of $CDCl_3$ (77.0) as an internal standard. Infrared spectra were recorded on a Thermofisher IR100 FTIR instrument using NaCl pellets. Absorption peaks are given in wavenumbers (cm^{-1}). Flash chromatography was performed using a CombiFlash® Companion (Teledyne-Isco) chromatography system with RediSep® (Teledyne-Isco) disposable flash chromatography columns. High resolution mass spectra were collected using the Agilent QTOF 6540 (Santa Clara, CA) mass spectrometer, equipped with an Agilent LC 1200 series HPLC system (Figure **S4**).

2.3.2 Characterization of the Optical Properties of Compound 1a and 1b

Absorbance and fluorescence spectra of Compound **1a** and **1b** (3 μM) in different solvents were obtained using the Agilent 8453 UV-vis spectrophotometer (Santa Clara, CA) and FluoroMax-4 spectrofluorometer (Jobin Yvon Horiba), respectively. Emission spectra of Compound **1a** and **1b** in HeLa cells were measured using a Nikon Eclipse Ti microscope (Melville, NY) operated in a wide-field, epi-fluorescence mode with a Kymera 193i adaptive focus imaging spectrograph and Newton CCD camera (Andor, Belfast, UK).

Coumarin 153 was used as the standard (Φ_{fl} =0.53, ethanol) to measure the fluorescence quantum yields of Compound **1a** and **1b**. A series of concentrations of Compounds **1a** and **1b** (0.05 μM- 0.5 μM) and coumarin 153 (0.05 μM- 0.5 μM) were prepared in ethanol and the absorbance spectra and the fluorescence spectra at 400 nm excitation were determined. Calibration curves were prepared by plotting the integrated fluorescence intensity vs absorbance at 400 nm, and were fit using a linear least squares regression. The slope of the fit line was used to calculate the fluorescence quantum yield using the following equation.

$$\Phi_x = \Phi_{std}\left(\frac{slope_x}{slope_{std}}\right)$$

Where the subscripts x and std represents the test compound and standard, respectively and Φ is the fluorescence quantum yield.

A home-made, time-correlated, single-photon counting (TCSPC) instrument with a SPC-630 TCSPC module (Becker & Hickl GmbH) was used to collect the fluorescence time-resolved data (*22*). Scattered light at the center excitation wavelength of 400 nm was collected (without the 450-nm long-pass emission filter used to collect the fluorescence lifetimes) to measure the instrument response function (IRF). Generally, the full-width at half-maximum of the IRF was approximately 50 ps. The TCSPC data were collected in 1024 channels (bins), with a time resolution of 98 ps/channel, and a full-scale time window of 100 ns. The peak-channel counts were set to 65,535. Data were fit with both a single and double exponential curve, and the fit with the lowest chi-square value was considered to be the best fit.

2.3.3 Cell Culture

HeLa (Human cervix epithelial cell line) and GM07373 (Bovine endothelial cell line) cell lines were cultured in Dulbecco's Modified Eagle's Medium (DMEM) supplemented with 10% fetal bovine serum, 12.5 mM streptomycin, and 36.5 mM penicillin (Fisher Scientific, Pittsburgh, PA) and incubated in a humidified incubator with 5% CO_2 at 37 ^{o}C (Thermo Scientific, Waltham, MA). These cell cultures were sub-cultured every two days using a 0.25% (w/v) trypsin-EDTA (Life Technology, Carlsbad, CA) solution.

2.3.4 Cell Viability Assay

The viability of cells treated with Compound **1a** or **1b** was determined using the MTT (3-(4,5-dimethylthiazol-2-yl)-2,5-diphenyltetrazolium bromide) assay. HeLa cells (4×10^4 cells /mL) or GM07373 cells (7×10^4 cells /mL) were treated with concentrations of Compound **1a** or **1b** from 3-1600 µM in complete DMEM medium in a 96 well plate and incubated for 24 h at 37^{o}C. After a 24 h incubation period, MTT in a PBS (5 mg/mL) solution was added to the wells and incubated at 37^{o}C for 3 h. Then the medium was removed from the wells and the formazan crystals were solubilized using a solubilization solution (16% (w/v) sodium dodecyl sulfate (SDS) in 40% (v/v) dimethylformamide (DMF) and 2% (v/v) glacial acetic acid, pH = 4.7). Absorbance was measured at 570 nm to determine the amount of produced formazan in each well. The percent viability was calculated based on the following equation.

$$\textbf{Percent viability} = \frac{\textbf{absorbance of compound 4a or 4b treated well}}{\textbf{absorbance of untreated control well}} \times \textbf{100}$$

The IC50 value (i.e., the concentration of a drug that is required for 50% inhibition of cell viability) was calculated by fitting the dose response curve with the Hill equation (*23*).

2.3.5 Preparation of Cells for Microscopy Studies

HeLa and GM07373 cells were plated on custom-made glass-bottom culture dishes and incubated overnight before performing microscopy experiments. On the day of the microscopy experiment, the growth medium was replaced with 2-5 µM Compound **1a** or **1b** in Hank's Balanced Salt Solution (HBSS) and incubated for 1 h at 37 ^{o}C. Cells were rinsed with HBSS medium and microscopy experiments were performed in HBSS medium. GM07373 cells were

incubated with Compound **1a** or **1b** in HBSS medium for 1 h at 37 ^{o}C then fixed with 4% paraformaldehyde for 10 min. After fixation, they were rinsed and imaged in PBS medium.

2.3.6 Microscopy Experiments

Wide-field imaging experiments were performed on a Nikon Eclipse TE2000U microscope (Melville, NY) operating in wide-field epi-fluorescence mode and equipped with a 100× Apo 1.49-numerical-aperture oil-immersion objective. Cell samples were illuminated with a mercury lamp (X-Cite 120 PC, EXFO Photonic Solutions Inc., Mississauga, Ontario, Canada). Compound **1a** and **1b** were excited using a 365 ± 35 nm filter and the signal was collected with a 470 ± 50 nm filter from Omega Optical (Brattleboro, VT). Fluorescence images were collected using a PhotonMAX 512 EMCCD camera (Princeton Instruments, Trenton, NJ) with acquisition times that ranged from 0.4 s to 2 s. Images were further analyzed with ImageJ software (National Institute of Health).

A Leica SP5 X MP inverted confocal microscope was used to collect confocal images. A 405 nm laser was used to excite Compounds **1a** and **1b**. ER-Tracker^{TM} Red was excited with a white light laser passing 580 nm. Emission of Compounds **1a** and **1b** was collected in the range from 460 to 480 nm and that of ER-Tracker^{TM} Red was collected from 610 to 630 nm.

2.3.7 Co-localization Experiment for Organelle-Specific Fluorophores

GM07373 cells were simultaneously incubated with Compound **1a** (1 μM) and the organelle-specific fluorophore in HBSS medium for 30 min at 37 ^{o}C. The organelle-specific fluorophores were: 1 μM ER-Tracker^{TM} Red (Invitrogen, Carlsbad, CA), 0.5 μM MitoTracker^{TM} Green FM (Invitrogen, Carlsbad, CA), and 50 nM LysoTracker^{TM} Red DND-99 (Invitrogen, Carlsbad, CA). Then the cells were rinsed and imaged in HBSS medium. Excitation/emission

filters passed 365 ± 45 nm/470 ± 20 nm (Compound **1a**), 562 ± 40 nm /629 ± 56 nm (ER-Tracker™ Red), 500 ± 20 nm/535 ± 35 nm (MitoTracker™ Green FM), and 562 ± 40 nm/629 ± 56 nm (LysoTracker™ Red DND-99).

2.4 Results and Discussion

2.4.1 Synthesis and Characterization

Compounds **1a** and **1b** were synthesized using a simple, two step reaction (Scheme **1**) and the chemical yields were 47% and 53%, respectively. These compounds were characterized using 1H NMR (Figure **S2**), 13C NMR (Figure **S3**), and high-resolution mass spectrometry (Figure S4). The high-resolution mass spectra of positive ions of Compound 1a and 1b confirmed the molecular masses of the structures (Figure **S4**). The observed mass for Compound 1a was 501.2060 and the calculated mass was 501.2054. The observed and calculated masses for Compound 1b were 517.2002 and 517.2003, respectively.

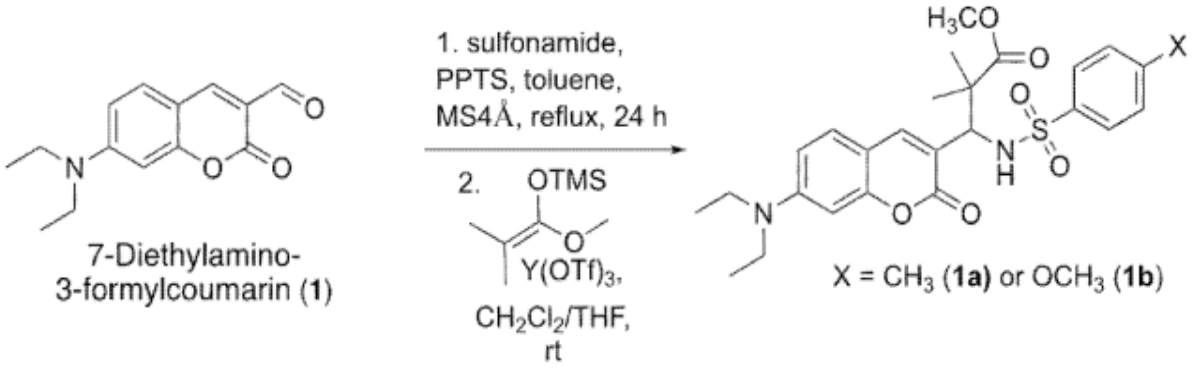

Scheme **1**: Synthetic procedure for Compound 1a and 1b.

The excitation spectra of Compound **1a** and **1b** had a λ_{max} of 410 nm, and the emission spectra had a λ_{max} of 486 ± 1 nm in water (Figure **1**). For both compounds, the full-width at half-maximum was 62 ± 1 nm for the fluorescence spectrum, and fluorescence quantum yields were

measured as 0.60 using coumarin 153 as a standard. Compounds **1a** and **1b** had extinction coefficients of 29,530 $M^{-1}cm^{-1}$ and 25,100 $M^{-1}cm^{-1}$, respectively.

2.4.2 Cell Viability Assay

The cytotoxicity of Compounds **1a** and **1b** in GM 07373 and HeLa cells was evaluated using an MTT assay (Figure **S5**). The half maximal inhibitory concentrations (IC_{50}) were detected as 215 ± 2 μM (Compound **1a**) and 252 ± 2 μM (Compound **1b**) for GM 07373 cells. The IC_{50} of Compound **1a** and **1b** for the HeLa cell line were 205 ± 2 μM and 239 ± 1 μM, respectively. These IC_{50} values were significantly higher than the concentrations of the probes used for imaging studies (0.5-5 μM), indicating the compounds exhibit negligible toxicity at concentrations relevant for imaging experiments within these tested cell lines. Trypan Blue exclusion assays were used to check the cell viability in HBSS medium over the timescales relevant for the imaging experiment (Supplementary page 3). The results (Table **S1**) show there is no significant difference between the cell viability of **1a** or **1b** treated cells and the control cells. The low cytotoxicity under imaging conditions means these probes are applicable for live cell studies.

2.4.3 Microscopy Experiments Showing Localization to the ER

Based on the presence of the sulfonamide group and the coumarin structure, Compounds **1a** and **1b** were hypothesized to be ER-targeting fluorescent probes. In order to test this, HeLa and GM07373 cells were incubated with 2 μM Compounds **1a** or **1b**, and live cells were imaged using a wide-field microscope. Both compounds penetrated the cell membrane and produced a fluorescence signal that was mainly observed in the perinuclear region of the cells, targeted to a

tubular structure (Figure **2**). As a control experiment, HeLa and GM07373 cells were incubated with 2 μM 7-diethylamino-3-formylcoumarin and live cells were imaged. As shown in figure **S6**, the fluorescent signal was observed inside the cell but did not localized into any specific intracellular structure. This observation supports the hypothesis that the sulfonamide side group in Compound **1a** and **1b** is essential for targeting the probe into the ER.

Co-localization experiments were performed using commercially available organelle trackers to identify the intracellular location of Compound **1a** (Figure **3**). The GM07373 cell images corresponding to the emission signal of ER-Tracker^{TM} Red and that of the Compound **1a** were well overlapped and the Pearson's correlation coefficient was 0.94. Images of cells labeled with MitoTracker^{TM} Green FM and LysoTracker^{TM} Red DND-99 fluorophores were not well overlapped with the images corresponding to Compound **1a** and the Pearson's correlation coefficients were 0.37 and 0.29, respectively.

The results for Compound **1b** were consistent with Compound **1a** (Figure **S7)**. Confocal microscopy images, which have improved axial spatial resolution compared to wide-field microscopy, also indicate that Compound **1a** and **1b** colocalize with known ER probes within the cells (Figure **S8** and **S9**). A movie of a live GM07373 cell treated with Compound **1a** is provided in the supplementary information, and highlights the ability to visualize the dynamics of the ER structure with this probe.

We further examined the compatibility of these compounds with fixation protocols. The fluorescence signal corresponding to Compound **1a** and **1b** were detected in the ER region even after fixation with 4% formaldehyde (Figure **4**).

2.4.4 Effects of Solvent Polarity on Optical Properties

The absorption and emission spectra of the Compound **1a** and **1b** were measured in solvents with various polarities (Figure **S10**). In water, both probes showed the maximum absorption at 410 nm and maximum fluorescence at 486 ± 1 nm, as discussed above. When the polarity of the solvent decreased, the absorption and fluorescence emission curves were blue shifted. The λ_{max} of fluorescence was: 467 nm in methanol, 457 nm in DMSO, 444 nm in methylene chloride and 432 nm in toluene. The bathochromic shift of the absorption and fluorescence spectra with increased solvent polarity is consistent with reports in literature for 7-alkylamino coumarins (*24, 25*). For the higher polarity solvents, the lower energy of the excited state fluorophore is due to the relaxation or reorientation of the excited state by the solvent dipoles (*26*). The fluorescence spectra measured for Compound **1a** and **1b** inside the cells were compatible with the fluorescence spectra collected in methanol or DMSO (Figure **5**).

This observation is consistent with Compound **1a** and **1b** being targeted to the ER membrane, which is less polar than the cytoplasm but not as nonpolar as the cell membrane due to its lower cholesterol concentration (*14*). In addition, the cLogD values reporting the partitioning between n-octanol and water were 4.2 and 3.8 for Compounds **1a** and **1b,** respectively. These values are consistent with other ER labeling probes (e.g., the cLogD of ER-Tracker™ Blue-White DPX is 4.0), and indicate the hydrophobic nature of these compounds make them compatible for partitioning into the ER membrane environment.

In order to show the utility of Compounds **1a** and **1b** for fluorescence lifetime imaging (FLIM), their lifetimes were also measured using the time-correlated single-photon counting (TCSPC) method (Figure **S11**). In an aqueous medium, data collected for both probes were well

fit to a double exponential decay with average lifetimes of 1.55 and 1.56 ns for Compound **1a** and **1b,** respectively. Approximately 90% of the population had a shorter lifetime (about 1.46 ns). About 10% of the population had lifetimes of 2.56 ns for Compound **1a** and 2.31 ns for Compound **1b**. The observation of two decay components in water is comparable to the results observed for 7-(diethylamino)coumarin-3-carboxylic acid molecule (*27*). In a high-polar protic medium, a planer intramolecular charge-transfer (ICT) excited state can be changed to a twisted charge transfer (TICT) excited state by rotating the bond orientation at the 7-diethylamino group of the probe. The ICT excited state is highly emissive but the TICT excited state undergoes nonradiative decay and is nonfluorescent (*24*). These two excited state populations likely explain the two populations measured in water. The lifetime data collected for Compound **1a** and **1b** in less polar aprotic and nonpolar solvents were well fit to a single exponential decay curve. In less polar aprotic solvents both the ground and excited states are likely in planer ICT structures (*28*) and the resulting lifetimes were 3.66 to 3.41 nm for Compound **1a** and 3.68 to 3.44 ns for Compound **1b**. In nonpolar solvents like toluene, 7-diethylamino group adopts a pyramidal configuration and forms a nonplanar structure in the ground and excited states (*28*). Therefore the observed lifetimes in toluene (2.94 nm for Compound **1a** and 2.99 ns for Compound **1b)** were lower than that of less polar aprotic solvents ((Figure **S11**). The lifetime of Compound **1a** and **1b** could not be measured in the cellular environment with the available instrument, however, the results discussed above suggest that the probes are suitable for FLIM and may report on the environment of the probe.

2.5 Conclusion

Two coumarin derivatives were synthesized, characterized and their optical properties were evaluated as ER targeting probes in live and fixed mammalian cells. The synthetic

procedure is not complex with only two involved steps. These compounds have comparable hydrophobicities as commercially available ER probes. A bright and narrow emission profile in the blue region (from 435-525 nm in methanol) was detected with excitation around 400 nm, indicating that these probes will be suitable for multi-color imaging with other probes. In these studies, there was no measureable difference in the membrane permeability of 1a and 1b in the tested cell lines. The quantum yields were also the same for both compounds, but 1a has a slightly higher extinction coefficient than that of 1b. Therefore, compound 1a has a slightly higher quantum efficiency (i.e., quantum yield times extinction coefficient). To further enhance the applicability of these probes in multi-color imaging, a series of ER probes with varying absorption/emission profiles could be developed by extending the conjugation in the coumarin core.

Acknowledgments

This work was initiated with funding from NSF grant CHE-1412084 and continued with funding from NSF grant CHE-1709099. We acknowledge the technical assistance from ISU Chemical Instrumentation Facility staff member *Dr. K. Harrata* for the mass spectroscopy measurements, the W. M. Keck Metabolomics Research Laboratory at Iowa State University for the use of their micro-plate reader, and Dr. J. Petrich and Dr. K. Santra for their assistance with the time-correlated, single-photon counting measurements.

2.6 References

1. Cooper, G. M. (2000) Endoplasmic Reticulum, in *The Cell: A Molecular Approach.* Second ed., Sinauer Associates, Sunderland (MA).
2. Schwarz, D. S., and Blower, M. D. (2016) The endoplasmic reticulum: structure, function and response to cellular signaling, *Cell Mol Life Sci 73*, 79-94.

3. Voeltz, G. K., Rolls, M. M., and Rapoport, T. A. (2002) Structural organization of the endoplasmic reticulum, *EMBO Rep 3*, 944-950.

4. Braakman, I., and Bulleid, N. J. (2011) Protein folding and modification in the mammalian endoplasmic reticulum, *Annu Rev Biochem 80*, 71-99.

5. Vance, J. E. (2015) Phospholipid synthesis and transport in mammalian cells, *Traffic 16*, 1-18.

6. He, H., Lam, M., McCormick, T. S., and Distelhorst, C. W. (1997) Maintenance of calcium homeostasis in the endoplasmic reticulum by Bcl-2, *J Cell Biol 138*, 1219-1228.

7. Sovolyova, N., Healy, S., Samali, A., and Logue, S. E. (2014) Stressed to death - mechanisms of ER stress-induced cell death, *Biol Chem 395*, 1-13.

8. Schuck, S., Prinz, W. A., Thorn, K. S., Voss, C., and Walter, P. (2009) Membrane expansion alleviates endoplasmic reticulum stress independently of the unfolded protein response, *J Cell Biol 187*, 525-536.

9. Van Bergeijk, P., Hoogenraad, C. C., and Kapitein, L. C. (2016) Right Time, Right Place: Probing the Functions of Organelle Positioning, *Trends Cell Biol 26*, 121-134.

10. Guiot, Y., Stevens, M., Marhfour, I., Stiernet, P., Mikhailov, M., Ashcroft, S. J. H., Rahier, J., Henquin, J. C., and Sempoux, C. (2007) Morphological localisation of sulfonylurea receptor 1 in endocrine cells of human, mouse and rat pancreas, *Diabetologia 50*, 1889-1899.

11. Tang, Y., Xu, A., Ma, Y., Xu, G., Gao, S., and Lin, W. (2017) A turn-on endoplasmic reticulum-targeted two-photon fluorescent probe for hydrogen sulfide and bio-imaging applications in living cells, tissues, and zebrafish, *Sci Rep 7*, 12944.

12. Xiao, H. B., Li, P., Hu, X. F., Shi, X. H., Zhang, W., and Tang, B. (2016) Simultaneous fluorescence imaging of hydrogen peroxide in mitochondria and endoplasmic reticulum during apoptosis, *Chem Sci 7*, 6153-6159.

13. Xu, S., Liu, H. W., Hu, X. X., Huan, S. Y., Zhang, J., Liu, Y. C., Yuan, L., Qu, F. L., Zhang, X. B., and Tan, W. (2017) Visualization of Endoplasmic Reticulum Aminopeptidase 1 under Different Redox Conditions with a Two-Photon Fluorescent Probe, *Anal Chem 89*, 7641-7648.

14. Van Meer, G., and de Kroon, A. I. (2011) Lipid map of the mammalian cell, *J Cell Sci 124*, 5-8.

15. Arai, S., Lee, S. C., Zhai, D., Suzuki, M., and Chang, Y. T. (2014) A molecular fluorescent probe for targeted visualization of temperature at the endoplasmic reticulum, *Sci Rep 4*, 6701.

16. Yang, Z., He, Y., Lee, J. H., Chae, W. S., Ren, W. X., Lee, J. H., Kang, C., and Kim, J. S. (2014) A Nile Red/BODIPY-based bimodal probe sensitive to changes in the micropolarity and microviscosity of the endoplasmic reticulum, *Chem Commun (Camb) 50*, 11672-11675.

17. Terasaki, M., Song, J., Wong, J. R., Weiss, M. J., and Chen, L. B. (1984) Localization of endoplasmic reticulum in living and glutaraldehyde-fixed cells with fluorescent dyes, *Cell 38*, 101-108.

18. Soltys, B. J., and Gupta, R. S. (1992) Interrelationships of endoplasmic reticulum, mitochondria, intermediate filaments, and microtubules--a quadruple fluorescence labeling study, *Biochem Cell Biol 70*, 1174-1186.

19. Cole, L., Davies, D., Hyde, G. J., and Ashford, A. E. (2000) Brefeldin A affects growth, endoplasmic reticulum, Golgi bodies, tubular vacuole system, and secretory pathway in Pisolithus tinctorius, *Fungal Genet Biol 29*, 95-106.

20. Cole, L., Davies, D., Hyde, G. J., and Ashford, A. E. (2000) ER-Tracker dye and BODIPY-brefeldin A differentiate the endoplasmic reticulum and golgi bodies from the tubular-vacuole system in living hyphae of Pisolithus tinctorius, *J Microsc 197*, 239-249.

21. Zimmerman, J. R., Johntony, O., Steigerwald, D., Criss, C., Myers, B. J., and Kinder, D. H. (2015) The Synthesis of a New Class of Highly Fluorescent Chromones via an Inverse-Demand Hetero-Diels-Alder Reaction, *Org Lett 17*, 3256-3259.

22. Santra, K., Smith, E. A., Petrich, J. W., and Song, X. (2017) Photon Counting Data Analysis: Application of the Maximum Likelihood and Related Methods for the Determination of Lifetimes in Mixtures of Rose Bengal and Rhodamine B, *J Phys Chem A 121*, 122-132.

23. Motulsky, H., Christopoulos, A. (2004) Fitting Dose Response Curves, in *Fitting Models to Biological Data Using Linear and Nonlinear Regression, A practical guide to curve fitting*, pp 256-265, Oxford University Press, New York.

24. Jones, G., Jackson, W. R., Choi, C., and Bergmark, W. R. (1985) Solvent Effects on Emission Yield and Lifetime for Coumarin Laser-Dyes - Requirements for a Rotatory Decay Mechanism, *J Phys Chem-Us 89*, 294-300.

25. Reichardt, C. (1994) Solvatochromic Dyes as Solvent Polarity Indicators, *Chem Rev 94*, 2319-2358.

26. Lakowicz, J. R. (2006) Solvents and Environmental Effects, in *Principles of Fluorescence Spectroscopy* Third ed., pp 205-231, Springer Science+Business Media, New York.

27. Chatterjee, A., and Seth, D. (2013) Photophysical properties of 7-(diethylamino)coumarin-3-carboxylic acid in the nanocage of cyclodextrins and in different solvents and solvent mixtures, *Photochem Photobiol 89*, 280-293.

28. Senthilkumar, S., Nath, S., and Pal, H. (2004) Photophysical properties of coumarin-30 dye in aprotic and protic solvents of varying polarities, *Photochem Photobiol 80*, 104-111.

2.7 Figures

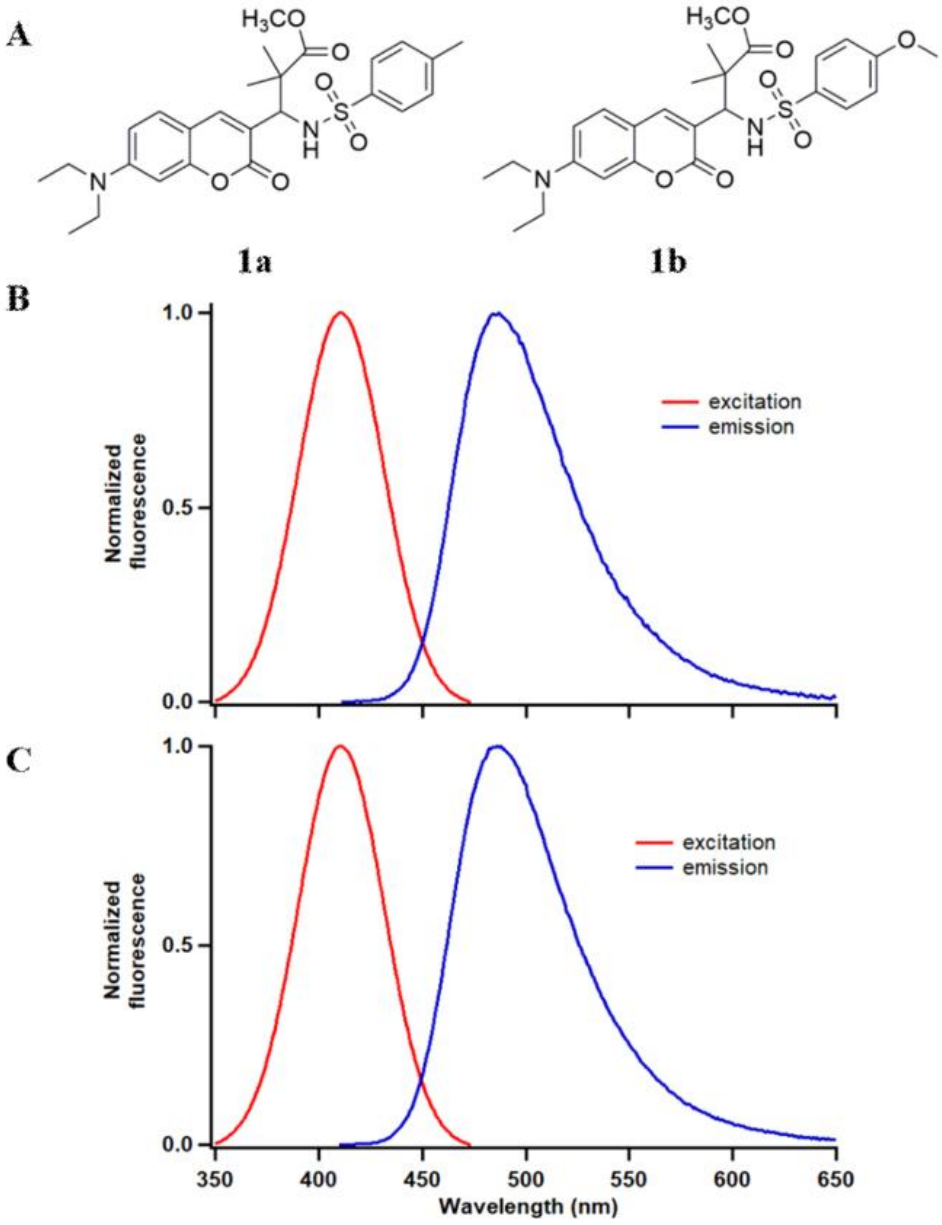

Figure 2.1 (A) Structures of coumarin-based Compounds **1a** and **1b**. The normalized excitation and fluorescence spectra of (B) Compound **1a** and (C) Compound **1b**.

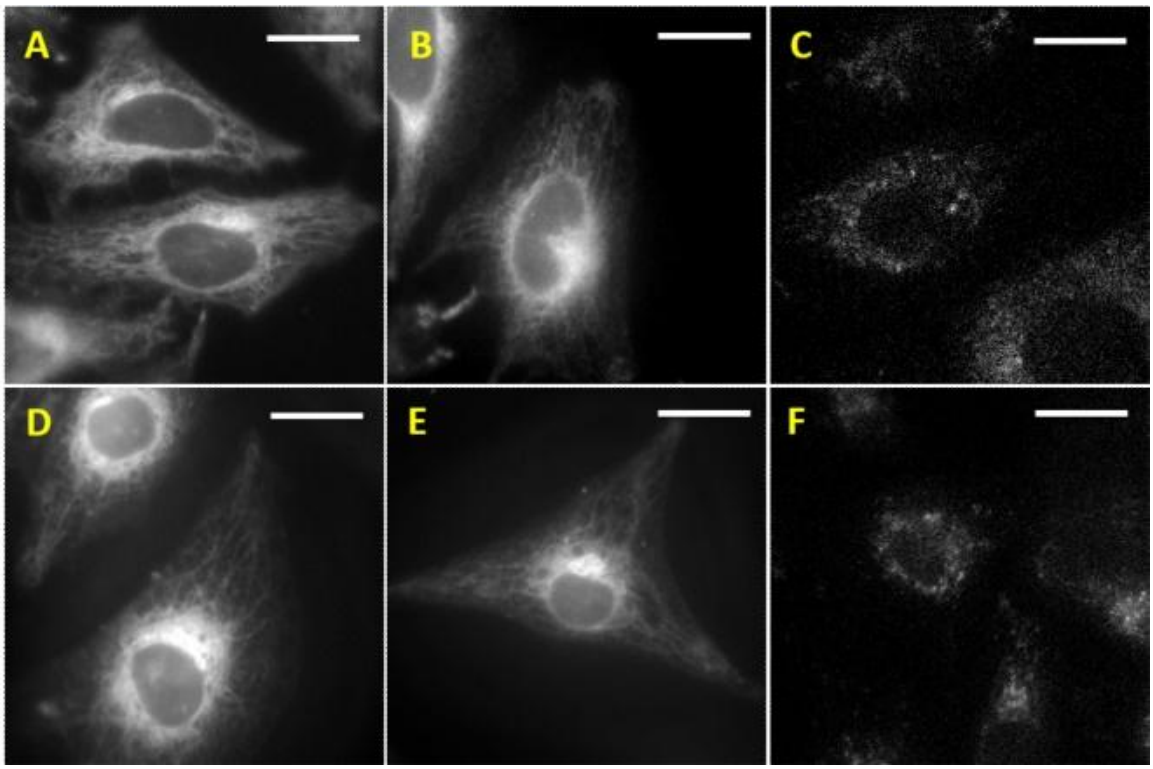

Figure 2.2 Images of (A, B, C) live HeLa cells and (D, E, F) live GM07373 cells treated with (A & D) 2 μM Compound 1a, (B & E) 2 μM Compound 1b and (C & F) control showing cellular autofluorescence. All images are shown in the same intensity scale. Scale bar is 20 μm in all the images.

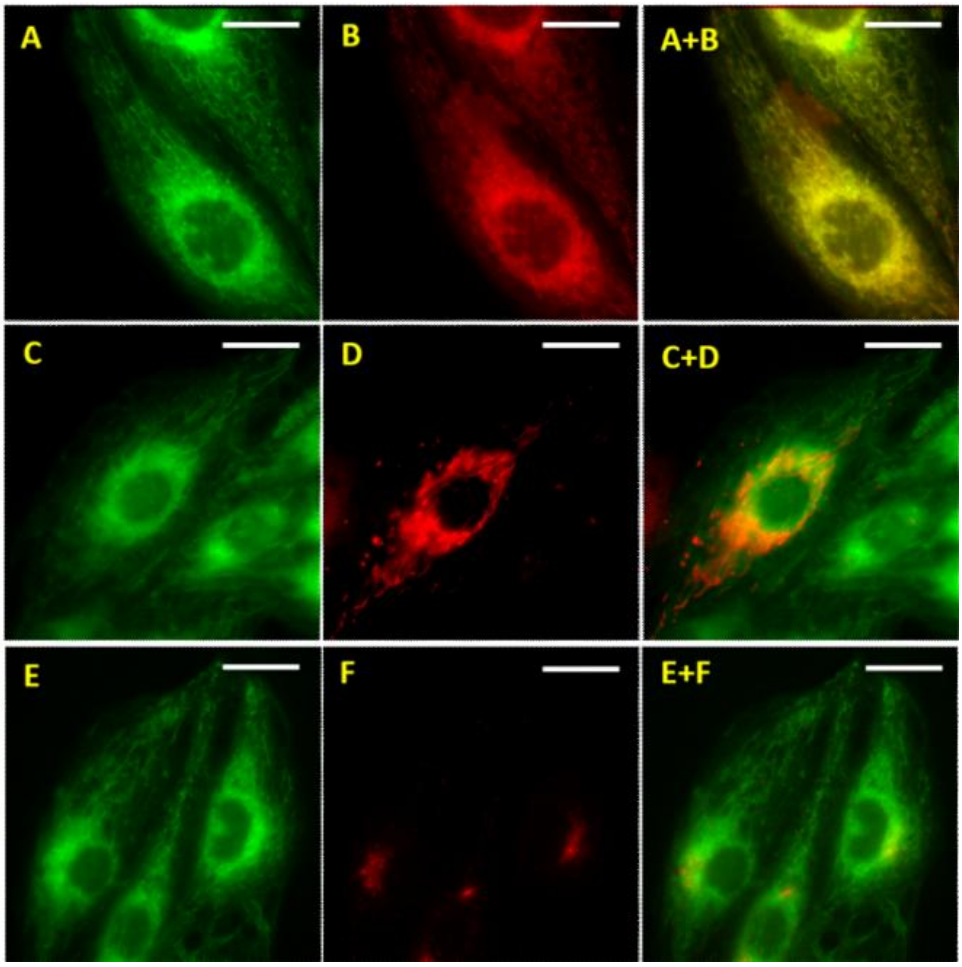

Figure 2.3 Images of live GM07373 cells co-labeled with Compound **1a** and commercially available organelle-specific fluorophores. The images A, C and E show the fluorescence signal corresponding to Compound **1a**. The images B, D and F show the fluorescence signal from ER-Tracker™ (endoplasmic reticulum), MitoTracker™ (mitochondria) and LysoTracker™ (lysosomes), respectively. The yellow color in the images in the right column shows where there is overlap in the signal for Compound **1a** and the organelle specific fluorophore. Scale bar is 20 μm in all the images.

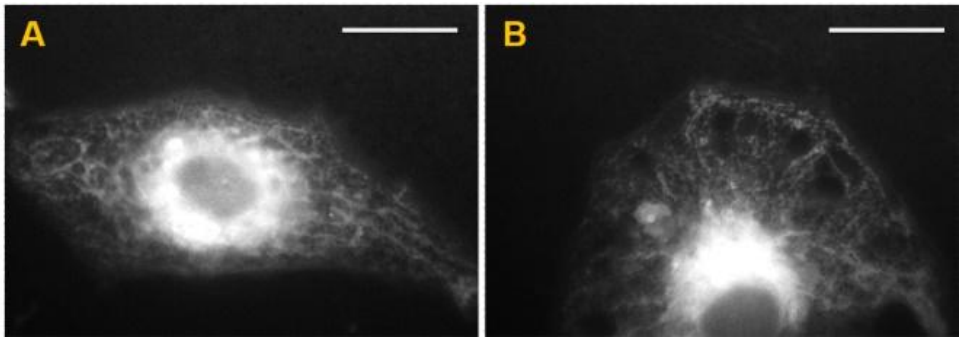

Figure 2.4 Images of GM07373 cells incubated with (A) Compound **1a** and (B) Compound **1b** for 1 h and then fixed with 4% paraformaldehyde. Scale bar is 20 μm in both images.

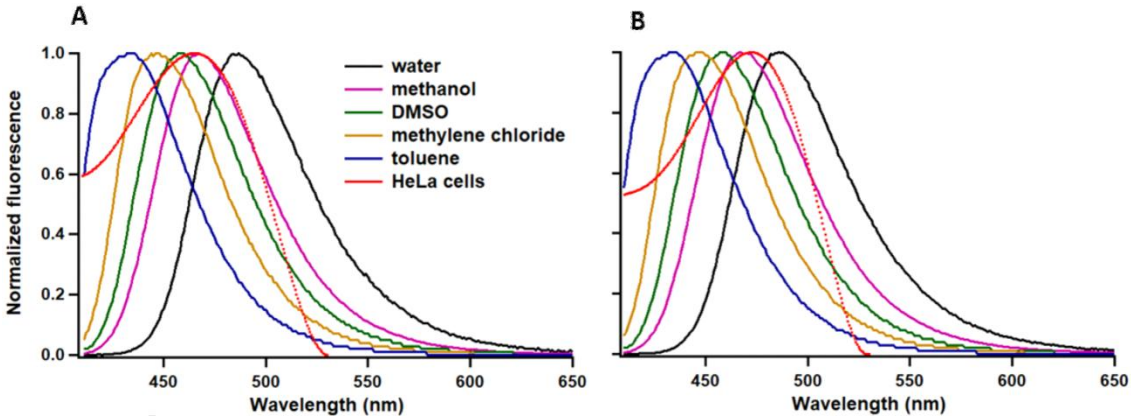

Figure 2.5 Normalized fluorescence spectra of (A) Compound **1a** and (B) Compound **1b** dissolved in solvents with different polarities (solid lines) and inside the HeLa cells as measured by microspectroscopy (dotted lines).

2.8 Supplementary Information

2.8.1 Characterization of Compound 1a and 1b

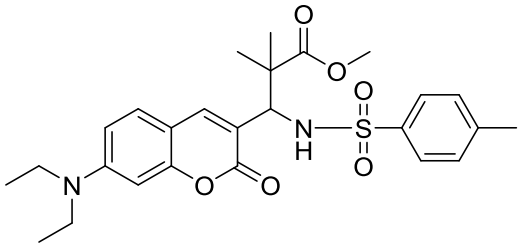

(1a) methyl 3-(7-(diethylamino)-2-oxo-2H-chromen-3-yl)-2,2-dimethyl-3-((4-methylphenyl)sulfonamido)propanoate: 47% yield; IR (cm^{-1}) 3281, 2958, 2926, 2856, 1728, 1604, 1519, 1261, 1133. ^{1}H NMR (400 MHz, Chloroform-*d*) δ 7.56 (d, *J* = 8.2, 2H), 7.06 (d, *J* = 8.8, 1H), 7.02 (s, 1H), 6.95 (d, *J* = 8.0 Hz, 2H), 6.53 (dd, *J* = 8.8, 2.5 Hz, 1H), 6.48 (s, 1H), 6.35 (d, *J* = 2.4 Hz, 1H), 4.30 (d, *J* = 10.6, 1H), 3.62 (s, 3H), 3.40 (q, *J* = 7.1 Hz, 4H), 1.98 (s, 3H), 1.27 (s, 3H), 1.22 (s, 3H), 1.20 (t, *J* = 7.3 Hz, 6H). ^{13}C NMR (101 MHz, $CDCl_3$) δ 176.1, 161.8, 155.9, 150.9, 143.4, 143.2, 137.4, 129.3, 129.0, 127.4, 126.6, 115.0, 109.2, 107.9, 96.8, 52.3, 48.2, 45.0, 23.2, 23.1, 21.2, 12.6; HRMS Exact mass calcd for $C_{26}H_{33}N_2O_6SN[M + H]^+$: 501.2054 Found: 501.2060.

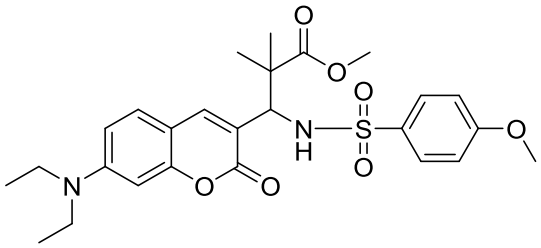

(1b) methyl 3-(7-(diethylamino)-2-oxo-2H-chromen-3-yl)-3-((4-methoxyphenyl)sulfonamido)-2,2-dimethylpropanoate: 53% yield; IR (cm^{-1}) 3434, 2957, 2929, 2875, 1727, 1273, 1181, 1093, 1038. ^{1}H NMR (400 MHz, Chloroform-*d*) δ 7.61 (d, *J* = 8.9 Hz, 2H), 7.09 (s, 1H), 7.06 (s, 1H), 6.62 (d, *J* = 8.9 Hz, 2H), 6.54 (dd, *J* = 8.8, 2.5 Hz, 1H), 6.49 (d, *J* = 10.7 Hz, 1H), 6.35 (d, *J* = 2.4 Hz, 1H), 4.30 (d, *J* = 10.6 Hz, 1H), 3.63 (s, 3H), 3.49 (s, 3H), 3.40 (q, *J* = 7.1 Hz, 4H), 1.27 (s, 3H), 1.22 (s, 3H), 1.20 (t, *J* = 7.4 Hz, 6H). ^{13}C NMR (101 MHz, $CDCl_3$) δ 176.1, 162.6, 161.8, 155.9, 150.9, 143.4, 132.1, 131.0, 129.4, 128.9, 114.4, 113.8, 109.2, 107.9, 96.8, 55.3, 52.3, 48.2, 45.0, 23.2, 23.0, 12.5; HRMS Exact mass calcd for $C_{26}H_{33}N_2O_7S$ $[M + H]^+$: 517.2003 Found: 517.2002.

2.8.2 Trypan Blue Assay

HeLa and GM07373 were incubated with 5 μM Compound **1a** or **1b** for an hour (i.e., the duration of the imaging experiment) at 37 ^{o}C in HBSS medium or in complete DMEM medium. Trypan Blue exclusion assays were used to determine the viable cell population after the incubation. After trypsinization, equal volumes of the cell suspension and 0.4% Trypan Blue stain were incubated for 3 minutes at room temperature. The number of viable cells that excluded the dye was counted with the aid of a hemocytometer and an optical microscope.

Table S2.1 Cell viability of compounds **1a** and **1b** as measured with trypan blue exclusion assay

Cell Culture	Cell viability (%) Compound 1a		Cell viability (%) Compound 1b		Cell viability (%) Control	
	HBSS medium	DMEM complete medium	HBSS medium	DMEM complete medium	HBSS medium	DMEM complete medium
GM07373	92.1 (±5.6)	93.0 (±4.1)	94.3 (±2.6)	95.7 (±1.8)	91.5 (±6.5)	92.2 (±4.2)
HeLa	94.1 (±4.0)	96.8 (±2.0)	94.0 (±3.4)	94.9 (±5.0)	95.0 (±3.8)	94.0 (±6.3)

2.8.3 Supplementary Figures

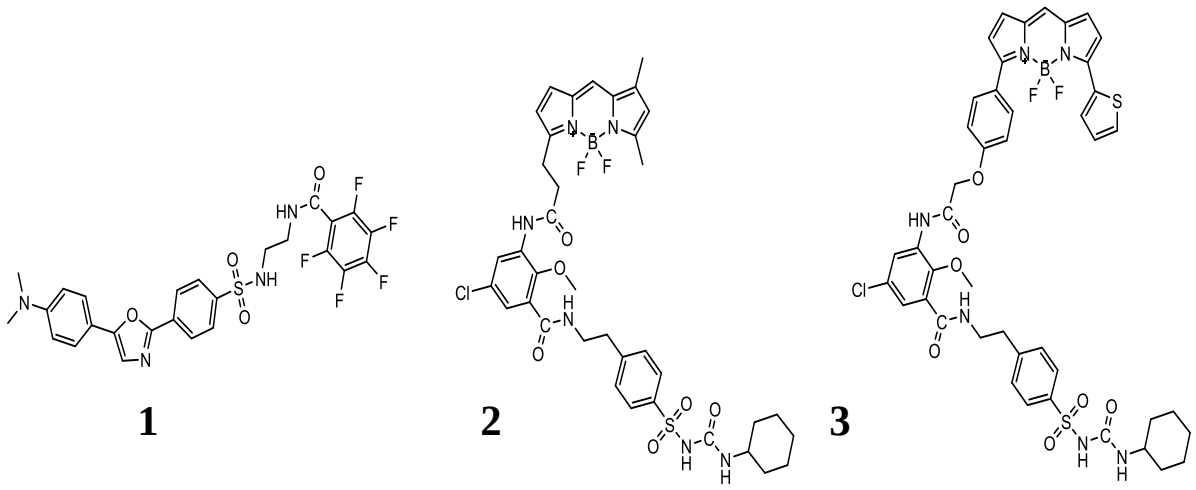

Figure S2.1 Structures of commercially available ER targeting probes: (**1)** ER-Tracker™ Blue-White DPX, (**2**) ER-Tracker™ Green, and (**3**) ER-Tracker™ Red.

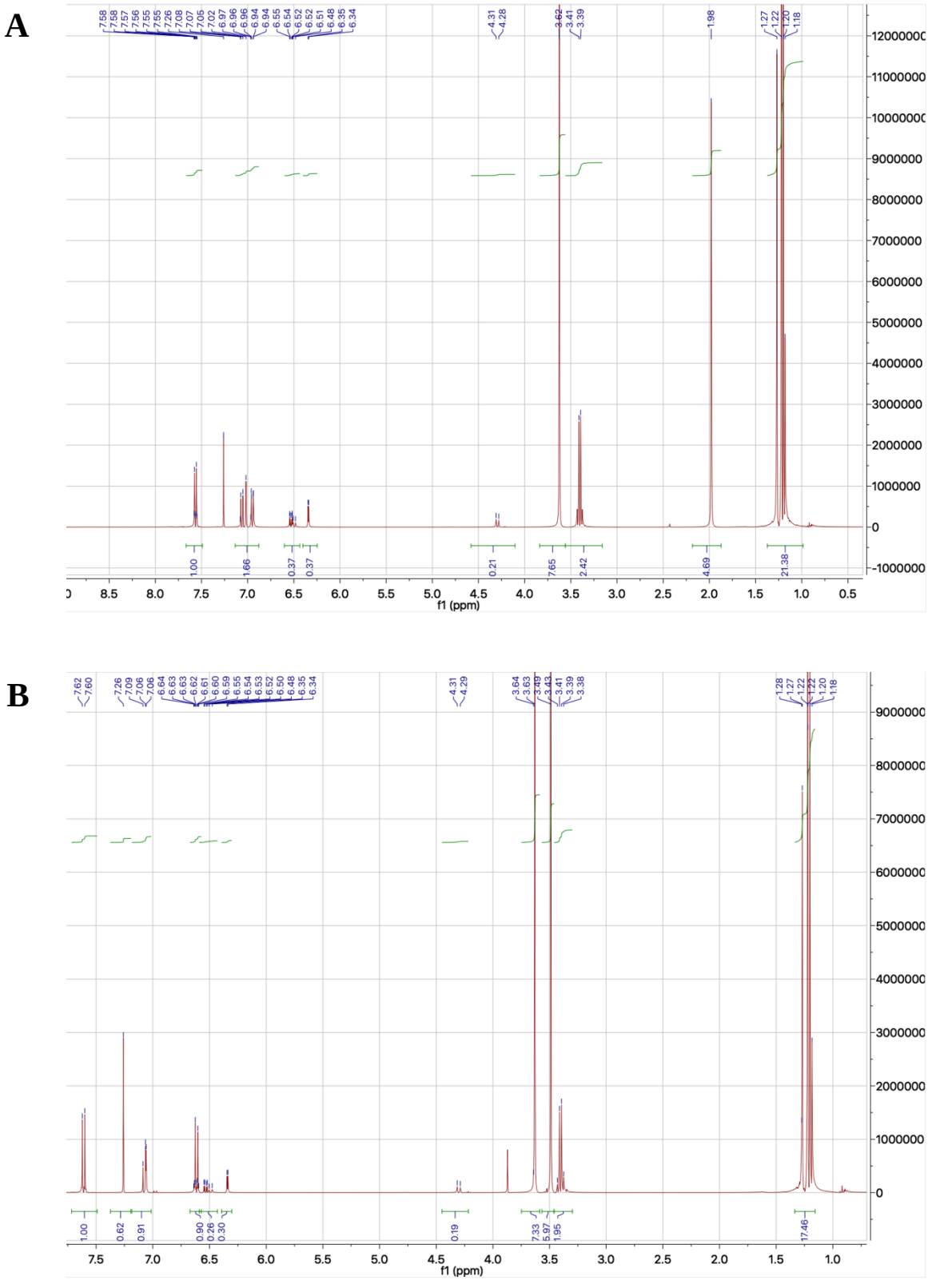

Figure S2.2 H1 NMR spectra of (A) Compound **1a** and (B) Compound **1b.**

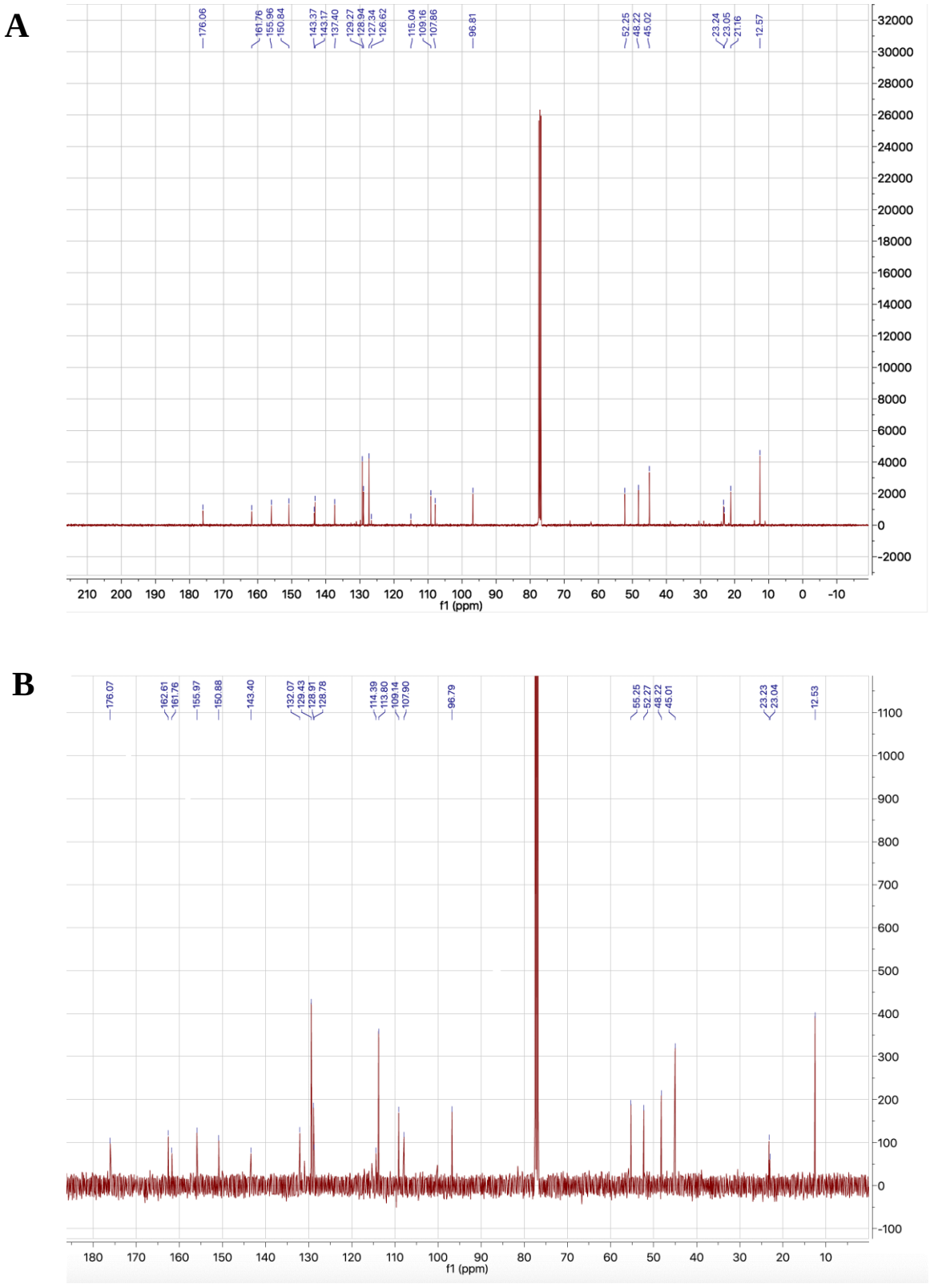

Figure S2.3 C13 NMR spectra of (A) Compound **1a** and (B) Compound **1b.**

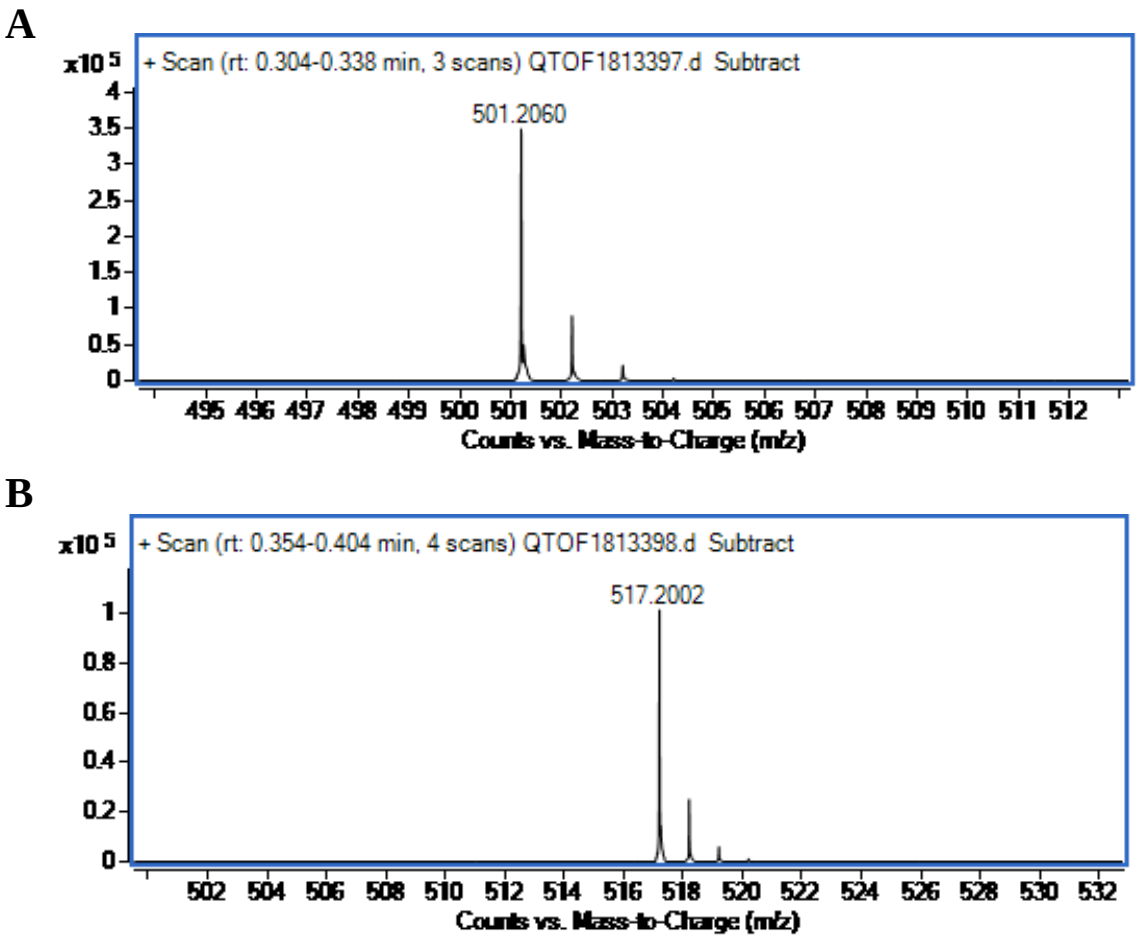

Figure S2.4 High resolution mass spectra of: (A) Compound **1a** and (B) Compound **1b** dissolved in methanol.

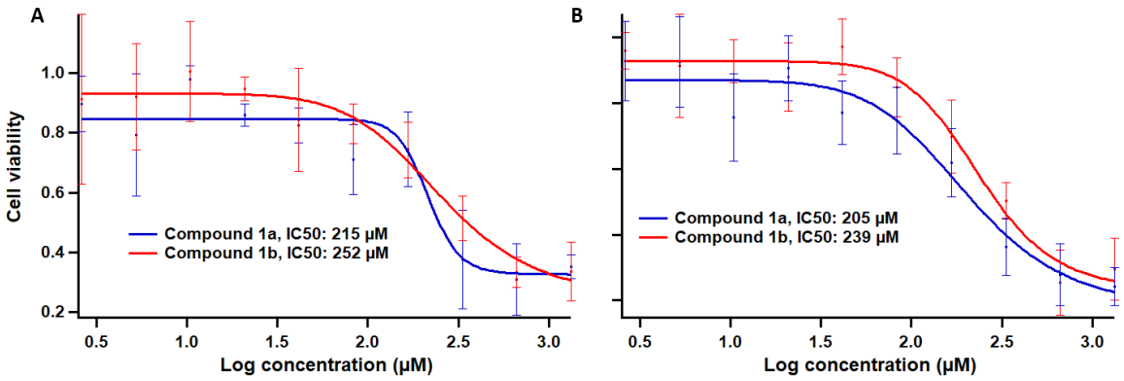

Figure S2.5 IC_{50} curves for Compound **1a** and **1b** in (A) GM07373 and (B) HeLa cells after incubation for 24 h. Error bars represent one standard deviation. The solid line represents the fit of the data to the Hill equation.

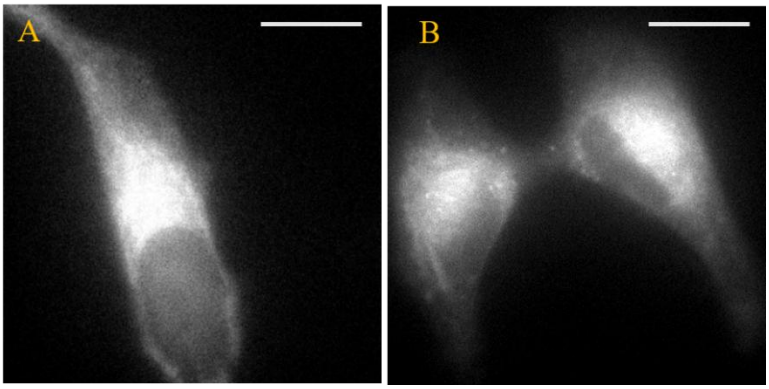

Figure S2.6 Images of (A) GM07373 cells and (B) HeLa cells incubated with 2 µM of 7-Diethylamino-3-formylcoumarin for 1 hour. Scale bar is 20 µm in both images.

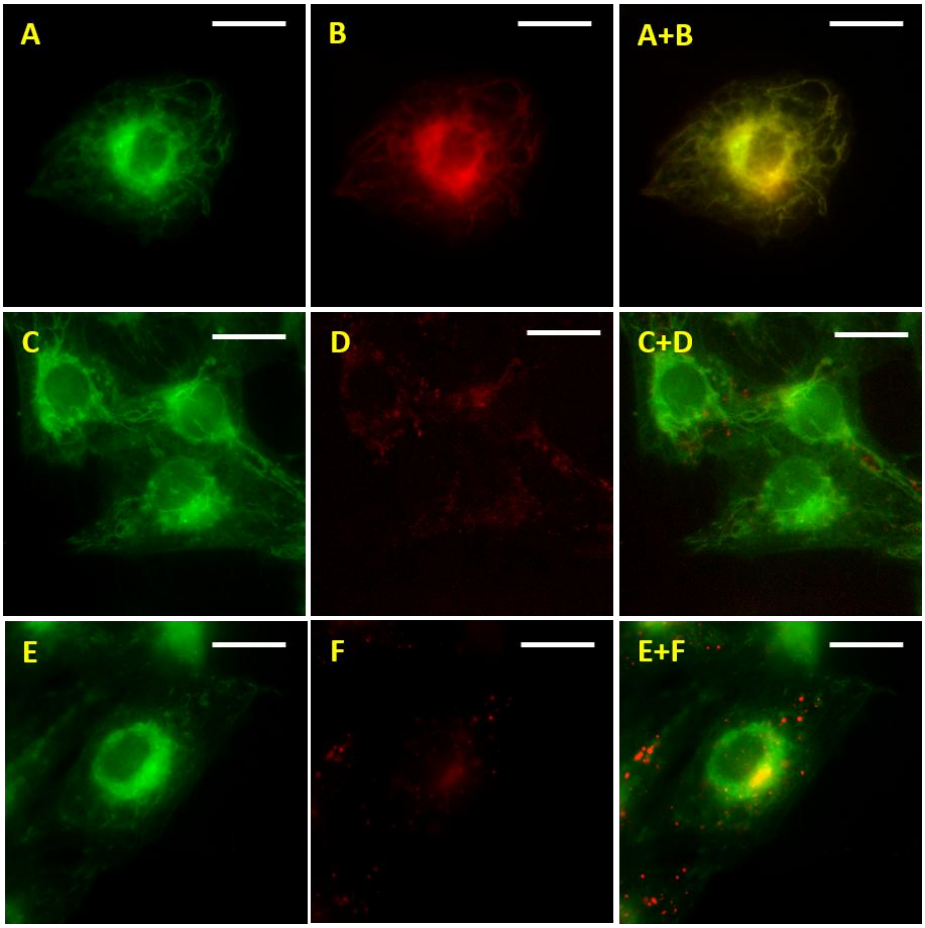

Figure S2.7 Images of live GM07373 cells co-labeled with Compound **1b** and commercially available organelle-specific fluorophores. The images A, C, and E show the fluorescence signal corresponding to Compound **1b**. The images B, D, and F show the fluorescence signal from ER-Tracker™ (endoplasmic reticulum), MitoTracker™ (mitochondria) and LysoTracker™ (lysosomes), respectively. The yellow color in the images in the right column shows where these is overlap in the signal for Compound **1b** and the organelle specific fluorophore. Scale bar is 20 μm in all the images.

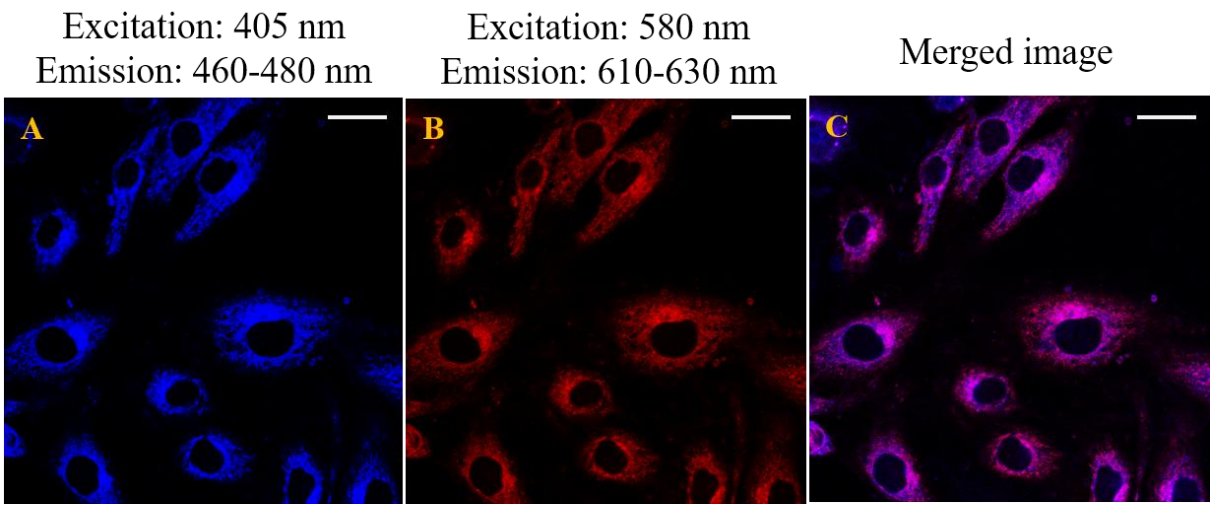

Figure S2.8 Confocal microscopy images of GM07373 cells incubated with Compound **1a** and ER-tracker red. The fluorescence images collected at the excitation and emission channels corresponding to (A) Compound **1a** and (B) ER-tracker red. C is the merged image of A and B. Scale bar is 25 μm in all the images.

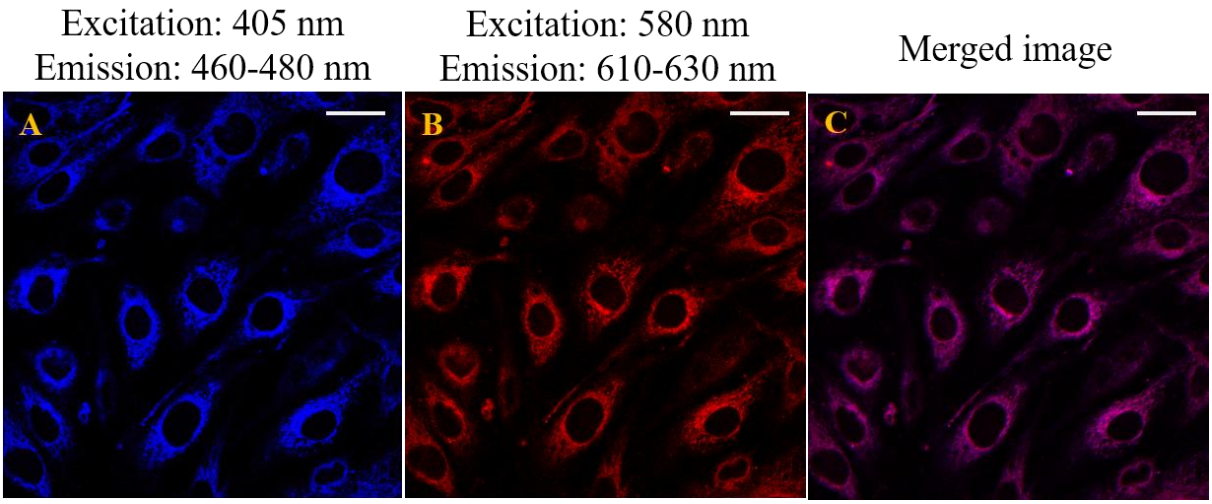

Figure S2.9 Confocal microscopy images of GM07373 cells incubated with Compound **1b** and ER-tracker red. The fluorescence images collected at the excitation and emission channels corresponding to (A) Compound **1b** and (B) ER-tracker red. C is the merged image of A and B. Scale bar is 25 μm in all the images.

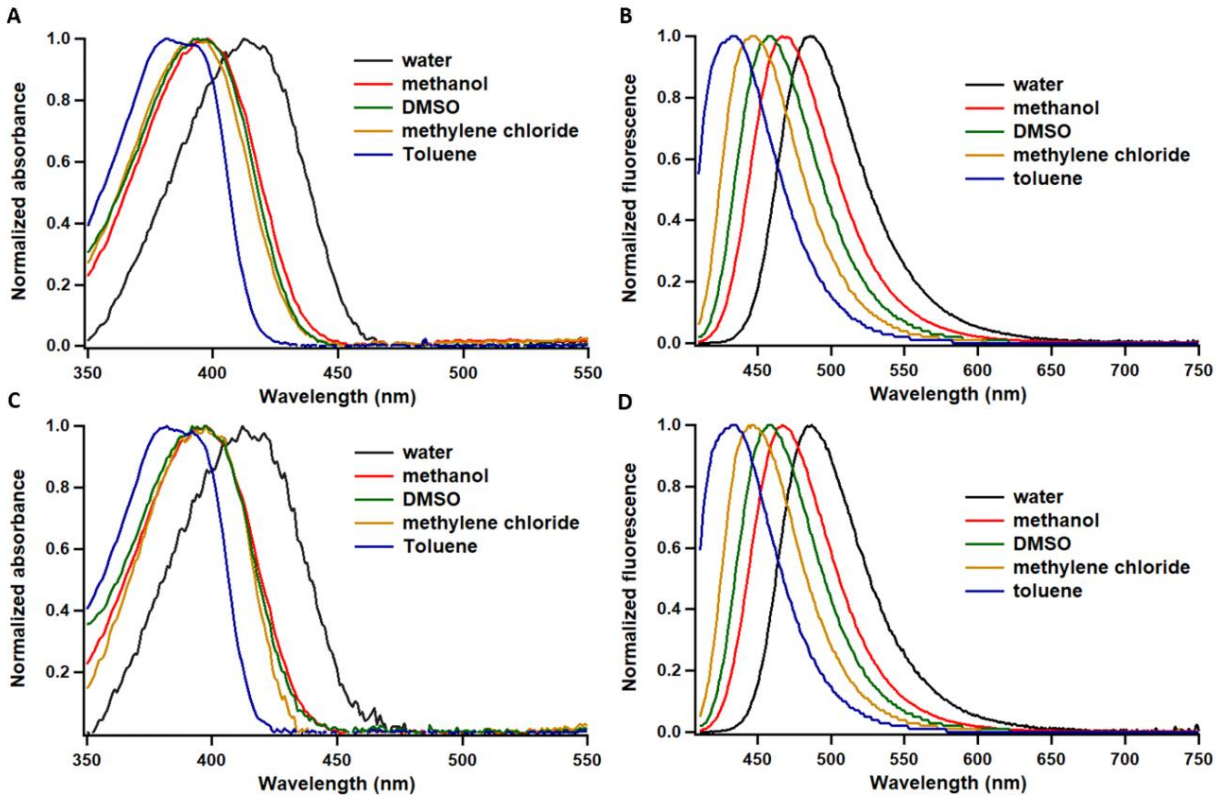

Figure S2.10 Normalized absorbance (A and C) and fluorescence (B and D) spectra of Compound **1a** and Compound **1b** in different solvents.

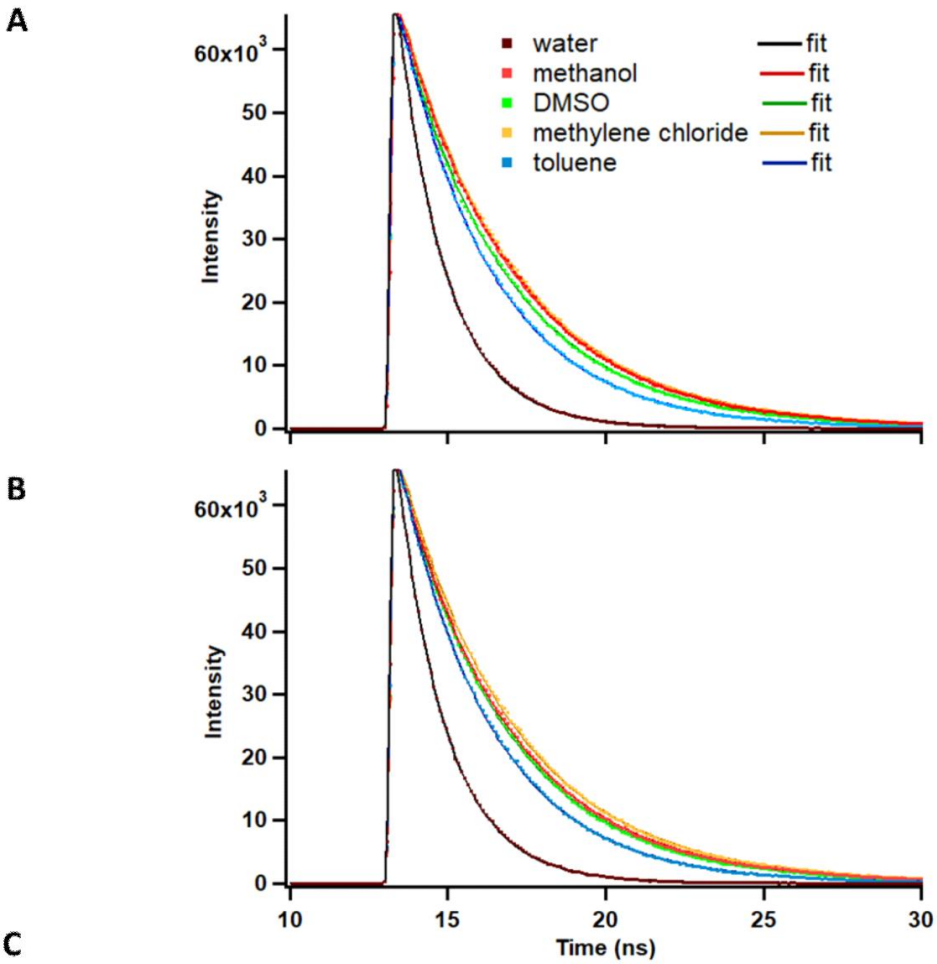

C

Solvent	Lifetime (ns)	
	Compound **1a**	Compound **1b**
water	1.47 (90.2 %)	1.45 (90.3 %)
	2.31 (9.8 %)	2.56 (9.7 %)
methanol	3.52	3.63
DMSO	3.41	3.44
methylene chloride	3.66	3.68
toluene	2.94	2.99

Figure S2.11 Fluorescence lifetimes curves in different solvents for (A) Compound **1a** and (B) Compound **1b.** (C) Lifetimes of Compound **1a** and **1b** obtained from the fits to the data shown in (A) and (B). Data collected in water were fit to a double exponential curve and the data collected in the other solvents were fit to a single exponential curve.

CHAPTER 3. A PHOTOACTIVATABLE BODIPY PROBE FOR LOCALIZATION-BASED SUPER-RESOLUTION CELLULAR IMAGING

Modified from a manuscript published in Angewandte Chemie International Edition

Chamari S. Wijesooriya,[1] Julie A. Peterson,[1] Pradeep Shrestha, Elizabeth J. Gehrmann,

Arthur H. Winter*, and Emily A. Smith*

Department of Chemistry, Iowa State University, Ames, Iowa 50011 USA

[1] These authors have contributed equally to the work.

3.1 Abstract

The synthesis and application of a photoactivatable boron-alkylated BODIPY probe for localization-based super-resolution microscopy is reported. Photoactivation and excitation of the probe is achieved by a previously-unknown boron-photodealkylation reaction with a single low-power visible laser and without requiring the addition of reducing agents or oxygen scavengers in the imaging buffer. These features lead to a versatile probe for localization-based microscopy of biological systems. The probe can be easily linked to nucleophile-containing molecules to target specific cellular organelles. By attaching paclitaxel to the photoactivatable BODIPY, *in vitro* and *in vivo* super-resolution imaging of microtubules is demonstrated. This is the first example of single molecule localization-based super-resolution microscopy using a visible-light activated BODIPY compound as a fluorescent probe.

3.2 Introduction

Fluorescence microscopy is a useful tool for imaging cellular components in their native environments. The spatial resolution of conventional optical microscopy is limited by the diffraction limit of light, which depends on the wavelength of light and the numerical aperture of the objective. Over the past two decades, optical imaging techniques with sub-diffraction spatial resolution, or super-resolution, have been developed.[1-4] Among these techniques, single molecule localization microscopies (SMLM) such as stochastic optical reconstruction microscopy (STORM)[4-5] and photoactivated localization microscopy (PALM)[2, 6-7] sequentially activate sparse subsets of fluorophores, localize their positions with high precision, and generate an image by summing the positions of the localized molecules in each frame.

Fluorescent probes play an important role in SMLM. Ideal probes should have low fluorescence in the 'off' state and high photon release in the 'on' state. Only a sparse subset of fluorophores should be 'on' in any frame to ensure high localization precision. Photoswitchable probes[8-12] (Figure 1A,B) have no fluorescence in the 'off' state. Common photoswitchable probes require a UV laser to convert the molecules into the 'on' state from the 'off' state and a second laser to excite the active fluorophore. While the use of two lasers decouples the switching rate and the signal intensity, a high-power UV laser affects cell health and may increase the autofluorescence in the cells. Typical laser irradiances used with common SMLM probes are listed in Table S1. These probes also often necessitate the use of additives in the imaging media to ensure switching to the 'off' state.

Photocages[13-18] (Figure 1C) releasing fluorescent compounds have been used as fluorescent probes, including probes for SMLM.[19] Photoactivated fluorescent probes are most

commonly derived from the o-nitrobenzyl photocage.[14, 19] This photocage has high quantum yields of release, but requires UV light activation and has potentially toxic nitrosoarene photoproducts. In addition, a second high power laser is necessary to excite the activated fluorophore. It would be beneficial to have a SMLM probe that only necessitates a single low power visible light laser. The use of a single laser is beneficial because it simplifies the instrumentation, but it also couples the mechanism to achieve photoactivation and the signal intensity.

Previously, *meso*-substituted BODIPY fluorophores have been introduced as photocages.[20-22] We recently discovered that BODIPY compounds with alkyl groups on the boron have higher quantum yields of photorelease than their fluoro analogues.[23] Serendipitously, we found that these dyes have a significant increase in fluorescence after irradiation with green light, independent of substitution at the *meso*-position. Herein, we describe a BODIPY fluorescent probe with photoactivation using ~500 nm light and its application for SMLM. We show the laser flux can be optimized to achieve a sufficient single molecule density and signal intensities that permit accurate localization of a sufficient number of fluorophores with a short analysis time.

3.3 Results and Discussion

The photophysics of the parent boron-alkylated BODIPY compound and its photoproduct were measured in methanol, a solvent wherein both compounds were well dissolved. Product studies showed that upon irradiation, the alkyl groups on the boron are cleaved and replaced with the solvent adduct (Figure 1D, Figure S1). The photophysical properties of compound **1** and **2** are typical of BODIPY dyes (Table 1), though it is notable that compound **2** has an ~6-fold higher fluorescence quantum yield than compound **1** in methanol. The photoactivation quantum

yield measured in methanol using a 532 nm Nd:YAG laser with a ferrioxalate actinometer was 0.79 ± 0.02%. This photoactivation quantum yield is lower than typical o-nitro benzyl derivatives[24], however the much higher extinction coefficient of BODIPY leads to a similar photoactivation quantum efficiency (i.e., the photoactivation quantum yield times the extinction coefficient), and the use of visible light and lack of the nitrosoarene byproduct makes the BODIPY probe more compatible with biological samples.

The photoreaction of compound 1 occurs in aqueous media, which is a requirement for biological imaging. The photoactivation quantum yield in 90:10 acetonitrile:water was 0.8 ± 0.1%, similar to the activation quantum yield in methanol. The fluorescence quantum yields of **1** and its photoproduct were measured in 90:10 acetonitrile:water to be 0.06 and 0.35, respectively. While the quantum yield was diminished in aqueous solution compared to methanol, the 6-fold increase in quantum yield when comparing **1** and its photoproduct was consistent with both media. The fluorescence intensity increased ~3-fold upon irradiation in PBS buffer compared to the initial fluorescence intensity of compound **1** (Figure S3), which was similar to the reaction in methanol. Competitive photoactivation and photobleaching during the irradiation likely explains the discrepancy between the ~3-fold increase in fluorescence measured after 5 minutes of irradiation in an aqueous medium (Figure S3) and the ~6-fold increase in the fluorescence quantum yield (Table 1). Mass spectrometry analysis indicates that the photoproduct in aqueous media is the expected dihydroxy species (Scheme S3, Figure S2).

A 4-(N-hydroxysuccinamidylcarbonyl)styryl group was added to **1** to facilitate the attachment of nucleophile-containing compounds that could be used to target the photoactivatable BODIPY probe to specific cellular structures. In order to show that the B-alkylated BODIPY compounds could be used for SMLM imaging we chose to target

microtubules for a proof of principle. Microtubules are rigid structures with an approximately 25 nm diameter.[25]They are a good target for testing super-resolution imaging approaches since their size is below the diffraction limit of light. Paclitaxel was chosen as an inexpensive and readily available microtubule probe. Compound **3** was synthesized with paclitaxel attached in a manner that preserves the binding sites to microtubules (Figure 1E).

Compound **3** initially has a lower fluorescence than **1** due to the styryl group on the *meso* position.[26] To verify that the molecule still undergoes photoactivation, it was irradiated in a cuvette in PBS buffer. Similar to the irradiation of **1**, the fluorescence intensity was enhanced three-fold over the initial fluorescence intensity at the start of the illumination (Figure 2A). After photoactivation, the excitation maximum was 498 nm and the emission maximum was 517 nm (Figure S5).

In addition, the photoactivation quantum yield of an analogue of 3 without paclitaxel attached in 90:10 acetonitrile:water was 0.12 ± 0.02%. The photoactivation quantum yield is likely lower than that of **1** (0.80%) due to the additional vibrational relaxation introduced with the styryl group in the *meso* position.

In order to optimize the laser irradiance for SMLM, compound **3** was drop cast on a clean glass coverslip and imaged using a home-built SMLM microscope. The laser irradiance affects the number and density of photoactivation events recorded in each frame of the movie. Highly inclined and laminated optical sheet (HILO) illumination was used to reduce background while generating signal from up to a 3 micron depth from the glass slide (i.e., the same illumination used for the cell studies). The fluorescence was detected using an electron multiplying charge coupled device (EMCCD) detector. No photoactivation of compound **3** was observed with laser irradiances lower than 28 W/cm^2. Graphs of the number of photoactivation events in each frame

of the movie were constructed for laser irradiances between 28 to 790 W/cm^2 (Figure 2B). All irradiances generated numerous photoactivation events and conditions not suitable for localization within the first 3 s, but sparse photoactivation events at subsequent times (Figure S6). A laser irradiance of 28, 160, 475, 790 W/cm^2 was suitable to activate an average of 21, 12, 5 and 3 molecules sparsely distributed throughout the frame over the 5 min movie. The number of localizable events in each frame decreased with increasing laser irradiance because the number of photoactivation events that occur in the first three seconds increases with increasing laser irradiance, leaving a smaller subset of molecules at later times to undergo photoactivation. For all irradiances between 28 to 790 W/cm^2 most molecules were on for less than 30 milliseconds before photobleaching (Figure S7).

The localization precision for each localizable photoactivation event was determined using the ThunderSTORM plug-in for Image J.[27] A histogram of the localization precision was generated for each laser irradiance (Figure 2C). The smallest median localization precision (14 nm) was obtained with 160 W/cm^2 irradiance.

Combining the results for the number of localization events in each frame and their precision, a laser irradiance of 160 W/cm^2 was used in subsequent imaging experiments. Importantly, this irradiance is significantly lower compared to those used for many conventional SMLM experiments, which are generally greater than kW/cm^2 (Table S1, S2).[28-29] The lower irradiance used in these experiments means photodamage to biological cells and tissues should be minimized.

The ability of compound **3** to bind to microtubules and retain the optical properties required for SMLM was tested using in vitro assembled microtubules spread on a glass slide (Figure 3A,D). Total internal reflection (TIR) illumination was used to reduce background and

achieve a median signal-to-noise ratio of 48 upon photoactivation (Figure S8). Fifty thousand frames were collected at which point no additional molecules could be detected. Localization data were used to reconstruct the super-resolution images. The microtubules were imaged with an average full-width-at-half maximum (FWHM) diameter of 45 ± 10 nm. This is smaller than the diffraction limit of light, but larger than the reported microtubule diameter (25 nm). The additional distance that separates the microtubule and the fluorescent label is minimal using compound **3** when compared to antibody-coupled fluorescent probes.[30-31] The microtubule was not immobilized on the glass slide, and the larger measured FWHM may be the result of the movement of the microtubule as a result of the presence of imaging buffer. SMLM was performed using HeLa cells fixed with 0.5 % glutaraldehyde and subsequently incubated with 1 μM compound **3** for 1 hour. The fluorescence signal was observed in the nucleus and was highly concentrated in the nucleoli (Figure S9). This result was consistent with previous reports[32-33] stating formaldehyde and glutaraldehyde fixation agents destroy the paclitaxel binding site on microtubules. Using ethylene glycol bis (succinimidyl succinate) (EGS) to fix the cells, however, the paclitaxel binding site on microtubules was retained (Figure 3B,E).[33]

To determine the utility of compound **3** for SMLM of microtubules in live cells, HeLa cells were incubated with 1 μM compound **3** in complete growth medium. Paclitaxel is a known substrate of the p-glycoprotein efflux transporter, therefore the p-glycoprotein inhibitor verapamil was used to enhance the concentration of compound **3** in the intracellular environment.[33-34] The diffraction-limited image showed the intracellular concentration was suitable for imaging the microtubules (Figure 3G). Super-resolution images of microtubules were generated using the localization data (Figure 3C,F). The data demonstrate that the photoactivatable BODIPY probe enables live cell SMLM. This will facilitate measuring cellular

structures that are altered by fixation procedures, although the dynamics of the imaged features should be slow relative to the data collection time.

Alexa Fluor 488 and ATTO 488 SMLM probes have similar excitation and emission profiles as the BODIPY probe used in this study. Alexa Fluor 488 and ATTO 488, however, require higher laser irradiances (1.2 to 3 kW/cm^2)[28, 35] to achieve the switching properties preferable for SMLM compared to the BODIPY photoactivatable probe (0.16 kW/cm^2). In addition, Alexa Fluor 488 and ATTO 488 require two lasers for SMLM. A UV laser is used to achieve the switching between ‘on' and ‘off’ states, which is not preferable for cell imaging. Photoactivatable probes used for SMLM, such as coumarin oxazine[36] and rhodamine-based photocages[12, 14, 37-39] also require UV irradiation (355 nm to 405 nm) and two lasers for the activation and excitation of the probe (Table S2). The photoactivatable BODIPY can be activated and excited with a single laser in the visible range, which overcomes the drawbacks of UV activation. Moreover, the BODIPY probe does not require reducing agents or oxygen scavengers as required for the photoswitchable class of SMLM probes.

3.4 Conclusion

In summary, the photoactivatable BODIPY probe is versatile and can be easily attached to nucleophile-containing molecules, thus it can be used to image various biological targets. We have demonstrated the utility of a B-alkylated BODIPY probe for SMLM by attaching paclitaxel for super-resolution imaging of microtubules. When the dynamics of the structure being imaged are sufficiently slow on the timescale of the imaging experiment, the photoactivatable BODIPY can be used to image live cells with a range of imaging buffers that do not contain reducing agents or oxygen scavengers. In addition, activation and excitation of the photoactivatable BODIPY probe is achieved with a single visible laser at comparably lower irradiances than

alternative SMLM approaches, so it is suitable for a variety of biological samples that might otherwise be damaged by the high power or UV lasers used with many current SMLM probes. The photophysical properties of BODIPY are easily tuned, which opens opportunities to making probes with various wavelengths of visible light activation. To further enhance the applicability of this probe, structural modifications to the BODIPY structure could be made to enhance water solubility, increase the brightness of the activated fluorophore in order to increase the localization precision, and introduce a palette of photoactivatable BODIPY with varying emission maxima for multicolor SMLM imaging.

Acknowledgements

This research is supported by the U.S. Department of Energy, Office of Science, Office of Biological and Environmental Research (BER) through an award to Ames Laboratory and Iowa State University. The Ames Laboratory is operated for the U.S. Department of Energy by Iowa State University under Contract No. DE-AC02-07CH11358. AHW is supported by National Science Foundation CHE-1464956. CSW was supported by National Science Foundation CHE-1412084 and CHE-1709099.

3.5 References

1. Hell, S. W., Toward fluorescence nanoscopy. *Nat Biotechnol* **2003,** *21* (11), 1347-55.

2. Betzig, E.; Patterson, G. H.; Sougrat, R.; Lindwasser, O. W.; Olenych, S.; Bonifacino, J. S.; Davidson, M. W.; Lippincott-Schwartz, J.; Hess, H. F., Imaging intracellular fluorescent proteins at nanometer resolution. *Science* **2006,** *313* (5793), 1642-5.

3. Pavani, S. R.; Thompson, M. A.; Biteen, J. S.; Lord, S. J.; Liu, N.; Twieg, R. J.; Piestun, R.; Moerner, W. E., Three-dimensional, single-molecule fluorescence imaging beyond the diffraction limit by using a double-helix point spread function. *Proc Natl Acad Sci U S A* **2009,** *106* (9), 2995-9.

4. Rust, M. J.; Bates, M.; Zhuang, X., Sub-diffraction-limit imaging by stochastic optical reconstruction microscopy (STORM). *Nat Methods* **2006,** *3* (10), 793-5.

5. Heilemann, M.; van de Linde, S.; Schuttpelz, M.; Kasper, R.; Seefeldt, B.; Mukherjee, A.; Tinnefeld, P.; Sauer, M., Subdiffraction-resolution fluorescence imaging with conventional fluorescent probes. *Angew Chem Int Ed Engl* **2008,** *47* (33), 6172-6.

6. Hess, S. T.; Girirajan, T. P.; Mason, M. D., Ultra-high resolution imaging by fluorescence photoactivation localization microscopy. *Biophys J* **2006,** *91* (11), 4258-72.

7. Deschout, H.; Lukes, T.; Sharipov, A.; Szlag, D.; Feletti, L.; Vandenberg, W.; Dedecker, P.; Hofkens, J.; Leutenegger, M.; Lasser, T.; Radenovic, A., Complementarity of PALM and SOFI for super-resolution live-cell imaging of focal adhesions. *Nat Commun* **2016,** *7*, 13693.

8. Dempsey, G. T.; Bates, M.; Kowtoniuk, W. E.; Liu, D. R.; Tsien, R. Y.; Zhuang, X., Photoswitching mechanism of cyanine dyes. *J Am Chem Soc* **2009,** *131* (51), 18192-3.

9. Vaughan, J. C.; Dempsey, G. T.; Sun, E.; Zhuang, X., Phosphine quenching of cyanine dyes as a versatile tool for fluorescence microscopy. *J Am Chem Soc* **2013,** *135* (4), 1197-200.

10. Roubinet, B.; Weber, M.; Shojaei, H.; Bates, M.; Bossi, M. L.; Belov, V. N.; Irie, M.; Hell, S. W., Fluorescent Photoswitchable Diarylethenes for Biolabeling and Single-Molecule Localization Microscopies with Optical Superresolution. *J Am Chem Soc* **2017,** *139* (19), 6611-6620.

11. Lee, M. K.; Rai, P.; Williams, J.; Twieg, R. J.; Moerner, W. E., Small-molecule labeling of live cell surfaces for three-dimensional super-resolution microscopy. *J Am Chem Soc* **2014,** *136* (40), 14003-6.

12. Folling, J.; Belov, V.; Kunetsky, R.; Medda, R.; Schonle, A.; Egner, A.; Eggeling, C.; Bossi, M.; Hell, S. W., Photochromic rhodamines provide nanoscopy with optical sectioning. *Angew Chem Int Ed Engl* **2007,** *46* (33), 6266-70.

13. Banala, S.; Maurel, D.; Manley, S.; Johnsson, K., A caged, localizable rhodamine derivative for superresolution microscopy. *ACS Chem Biol* **2012,** *7* (2), 289-93.

14. Grimm, J. B.; Klein, T.; Kopek, B. G.; Shtengel, G.; Hess, H. F.; Sauer, M.; Lavis, L. D., Synthesis of a Far-Red Photoactivatable Silicon-Containing Rhodamine for Super-Resolution Microscopy. *Angew Chem Int Ed Engl* **2016,** *55* (5), 1723-7.

15. Hauke, S.; von Appen, A.; Quidwai, T.; Ries, J.; Wombacher, R., Specific protein labeling with caged fluorophores for dual-color imaging and super-resolution microscopy in living cells. *Chem Sci* **2017,** *8* (1), 559-566.

16. Kobayashi, T.; Komatsu, T.; Kamiya, M.; Campos, C.; Gonzalez-Gaitan, M.; Terai, T.; Hanaoka, K.; Nagano, T.; Urano, Y., Highly activatable and environment-insensitive optical highlighters for selective spatiotemporal imaging of target proteins. *J Am Chem Soc* **2012,** *134* (27), 11153-60.

17. Belov, V. N.; Mitronova, G. Y.; Bossi, M. L.; Boyarskiy, V. P.; Hebisch, E.; Geisler, C.; Kolmakov, K.; Wurm, C. A.; Willig, K. I.; Hell, S. W., Masked rhodamine dyes of five principal colors revealed by photolysis of a 2-diazo-1-indanone caging group: synthesis, photophysics, and light microscopy applications. *Chemistry* **2014,** *20* (41), 13162-73.

18. Klotzner, D. P.; Klehs, K.; Heilemann, M.; Heckel, A., A new photoactivatable near-infrared-emitting QCy7 fluorophore for single-molecule super-resolution microscopy. *Chem Commun (Camb)* **2017,** *53* (71), 9874-9877.

19. Li, W. H.; Zheng, G., Photoactivatable fluorophores and techniques for biological imaging applications. *Photochem Photobiol Sci* **2012,** *11* (3), 460-71.

20. Goswami, P. P.; Syed, A.; Beck, C. L.; Albright, T. R.; Mahoney, K. M.; Unash, R.; Smith, E. A.; Winter, A. H., BODIPY-derived photoremovable protecting groups unmasked with green light. *J Am Chem Soc* **2015,** *137* (11), 3783-6.

21. Palao, E.; Slanina, T.; Muchova, L.; Solomek, T.; Vitek, L.; Klan, P., Transition-Metal-Free CO-Releasing BODIPY Derivatives Activatable by Visible to NIR Light as Promising Bioactive Molecules. *J Am Chem Soc* **2016,** *138* (1), 126-33.

22. Rubinstein, N.; Liu, P.; Miller, E. W.; Weinstain, R., meso-Methylhydroxy BODIPY: a scaffold for photo-labile protecting groups. *Chem Commun (Camb)* **2015,** *51* (29), 6369-72.

23. Slanina, T.; Shrestha, P.; Palao, E.; Kand, D.; Peterson, J. A.; Dutton, A. S.; Rubinstein, N.; Weinstain, R.; Winter, A. H.; Klan, P., In Search of the Perfect Photocage: Structure-Reactivity Relationships in meso-Methyl BODIPY Photoremovable Protecting Groups. *J Am Chem Soc* **2017,** *139* (42), 15168-15175.

24. Klan, P.; Solomek, T.; Bochet, C. G.; Blanc, A.; Givens, R.; Rubina, M.; Popik, V.; Kostikov, A.; Wirz, J., Photoremovable protecting groups in chemistry and biology: reaction mechanisms and efficacy. *Chem Rev* **2013,** *113* (1), 119-91.

25. Waterman-Storer, C. M., Microtubules and microscopes: how the development of light microscopic imaging technologies has contributed to discoveries about microtubule dynamics in living cells. *Mol Biol Cell* **1998,** *9* (12), 3263-71.

26. Lincoln, R.; Greene, L. E.; Bain, C.; Flores-Rizo, J. O.; Bohle, D. S.; Cosa, G., When push comes to shove: unravelling the mechanism and scope of nonemissive meso-unsaturated BODIPY dyes. *J Phys Chem B* **2015,** *119* (13), 4758-65.

27. Ovesny, M.; Krizek, P.; Borkovec, J.; Svindrych, Z.; Hagen, G. M., ThunderSTORM: a comprehensive ImageJ plug-in for PALM and STORM data analysis and super-resolution imaging. *Bioinformatics* **2014,** *30* (16), 2389-90.

28. Dempsey, G. T.; Vaughan, J. C.; Chen, K. H.; Bates, M.; Zhuang, X., Evaluation of fluorophores for optimal performance in localization-based super-resolution imaging. *Nat Methods* **2011,** *8* (12), 1027-36.

29. van de Linde, S.; Loschberger, A.; Klein, T.; Heidbreder, M.; Wolter, S.; Heilemann, M.; Sauer, M., Direct stochastic optical reconstruction microscopy with standard fluorescent probes. *Nat Protoc* **2011,** *6* (7), 991-1009.

30. Chen, Z.; Cornish, V. W.; Min, W., Chemical tags: inspiration for advanced imaging techniques. *Curr Opin Chem Biol* **2013,** *17* (4), 637-43.

31. Chozinski, T. J.; Gagnon, L. A.; Vaughan, J. C., Twinkle, twinkle little star: photoswitchable fluorophores for super-resolution imaging. *FEBS Lett* **2014,** *588* (19), 3603-12.

32. Guy, R.; Scott, Z.; Sloboda, R.; Nicolaou, K., Fluorescent taxoids. *Chem Biol* **1996,** *3* (12), 1021-31.

33. Lukinavicius, G.; Reymond, L.; D'Este, E.; Masharina, A.; Gottfert, F.; Ta, H.; Guther, A.; Fournier, M.; Rizzo, S.; Waldmann, H.; Blaukopf, C.; Sommer, C.; Gerlich, D. W.; Arndt, H. D.; Hell, S. W.; Johnsson, K., Fluorogenic probes for live-cell imaging of the cytoskeleton. *Nat Methods* **2014,** *11* (7), 731-3.

34. Lee, M. M.; Gao, Z.; Peterson, B. R., Synthesis of a Fluorescent Analogue of Paclitaxel That Selectively Binds Microtubules and Sensitively Detects Efflux by P-Glycoprotein. *Angew Chem Int Ed Engl* **2017,** *56* (24), 6927-6931.

35. Heilemann, M.; van de Linde, S.; Mukherjee, A.; Sauer, M., Super-resolution imaging with small organic fluorophores. *Angew Chem Int Ed Engl* **2009,** *48* (37), 6903-8.

36. Deniz, E.; Tomasulo, M.; Cusido, J.; Yildiz, I.; Petriella, M.; Bossi, M. L.; Sortino, S.; Raymo, F. M., Photoactivatable Fluorophores for Super-Resolution Imaging Based on Oxazine Auxochromes. *J Phys Chem C* **2012,** *116* (10), 6058-6068.

37. He, H.; Ye, Z.; Zheng, Y.; Xu, X.; Guo, C.; Xiao, Y.; Yang, W.; Qian, X.; Yang, Y., Super-resolution imaging of lysosomes with a nitroso-caged rhodamine. *Chem Commun (Camb)* **2018,** *54* (23), 2842-2845.

38. Pan, D.; Hu, Z.; Qiu, F.; Huang, Z. L.; Ma, Y.; Wang, Y.; Qin, L.; Zhang, Z.; Zeng, S.; Zhang, Y. H., A general strategy for developing cell-permeable photo-modulatable organic fluorescent probes for live-cell super-resolution imaging. *Nat Commun* **2014,** *5*, 5573.

39. Roubinet, B.; Bischoff, M.; Nizamov, S.; Yan, S.; Geisler, C.; Stoldt, S.; Mitronova, G. Y.; Belov, V. N.; Bossi, M. L.; Hell, S. W., Photoactivatable Rhodamine Spiroamides and Diazoketones Decorated with "Universal Hydrophilizer" or Hydroxyl Groups. *J Org Chem* **2018,** *83* (12), 6466-6476.

3.6 Tables and Figures

Table 3.1 Photophysical properties of compounds **1, 2** and **3**

	λ_{ex} (nm)	λ_{em} (nm)	ε ($M^{-1}cm^{-1}$)	Φ_f[a]
1	490	505	52000	0.15
2	495	510	53000	0.96
3	498	517	15000	0.002

[a] Fluorescence quantum yield calculated in methanol using fluorescein as a fluorescent standard.

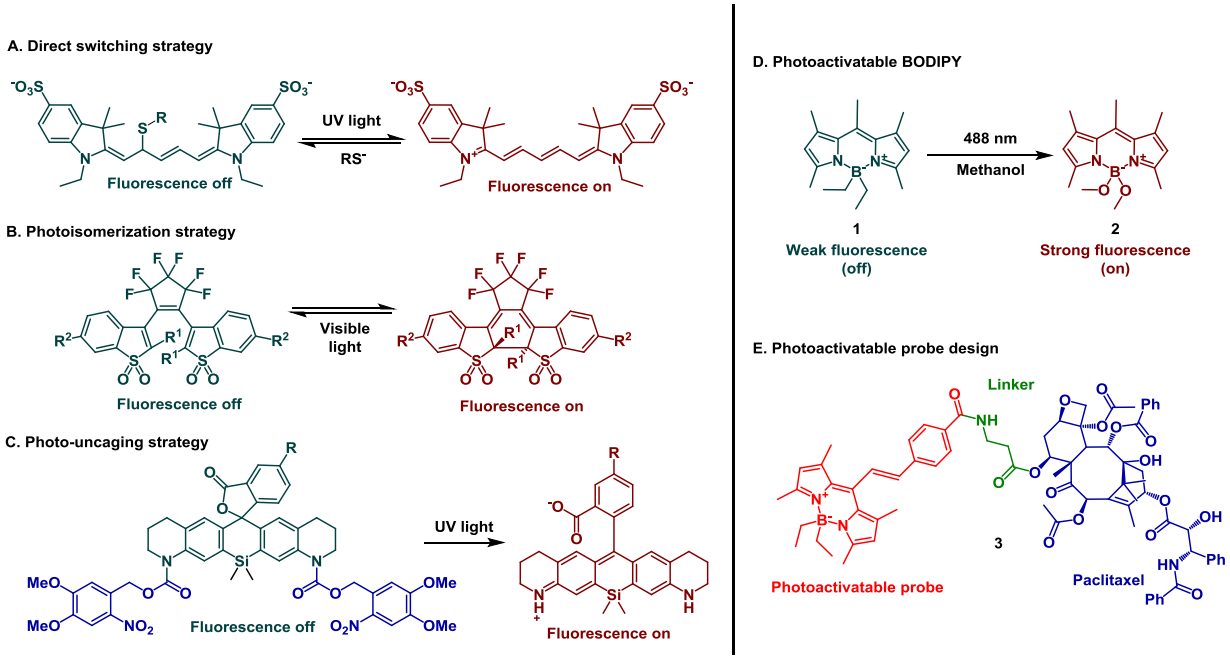

Figure 3.1 Examples of SMLM probes based on (A) direct switching[8-9], (B) photoisomerization[10], and (C) photo-uncaging[14]. (D) photoactivation of B-dialkylated BODIPY with visible light generates a fluorescent signal. (E) Photoactivatable BODIPY probe for SMLM imaging of microtubules.

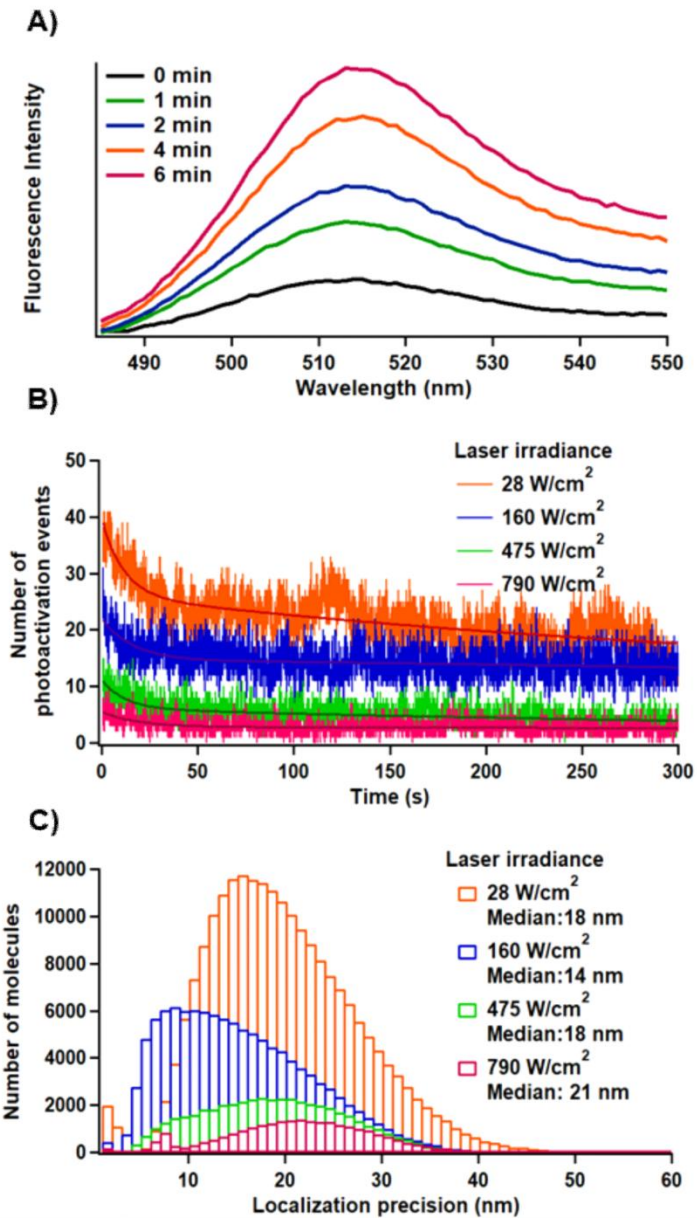

Figure 3.2 (A) Fluorescence increase of compound **3** irradiated with a 500 W halogen arc lamp in a quartz cuvette. The start of illumination is 0 min. The fluorescence was measured using a 470 nm excitation wavelength. (B) Plots of the number of photoactivated BODIPY over time (measured in each frame starting after 3 s) using a 488 nm laser with the indicated irradiance. There is an exponential decay in photoactivation events with illumination time after 3 s. (C) Histogram of the localization precision of the photoactivated molecules.

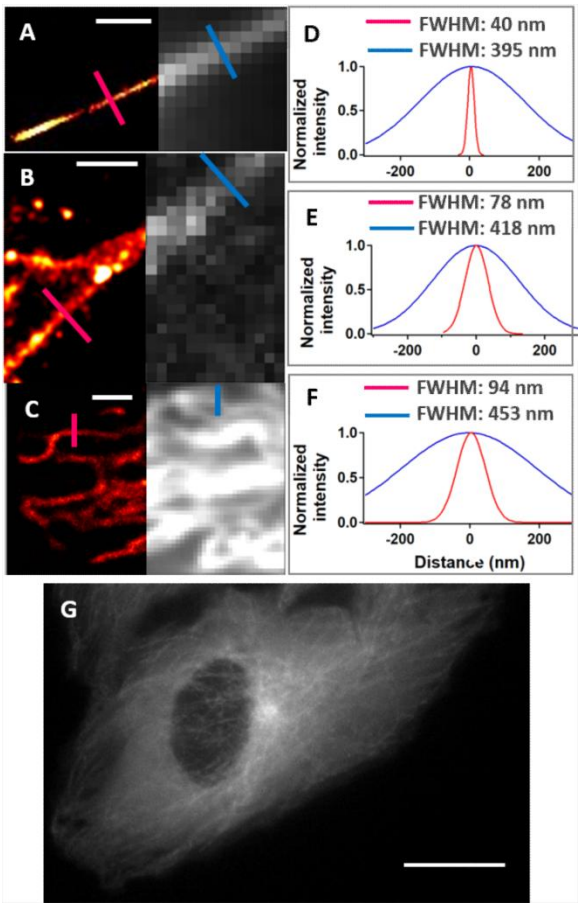

Figure 3.3 (A) In vitro, (B) fixed HeLa cell, and (C) live HeLa cell SMLM images of compound 3-labeled microtubules (color scale images). Gray scale images are the diffraction-limited images generated by summing all the frames in the movie without localizing the fluorophores. HEPES buffer was used as the imaging medium for live cells and PBS buffer was used for in vitro and fixed cell images. A single 160 W/cm^{-2} 488 nm laser was used for activation and excitation. (D), (E) and (F) are the Gaussian fits of line-scan intensities across the indicated areas in the SMLM images (red line) and corresponding diffraction limited images (blue line) of (A), (B) and (C), respectively. Images (B) and (C) show only a small area of the cell; (G) is the diffraction-limited image of microtubules showing the entire cell. Scale bar: (A) and (B) 500 nm, (C) 1 μm, (G) 20 μm.

3.7 Supplementary Information

3.7.1 Probe Synthesis

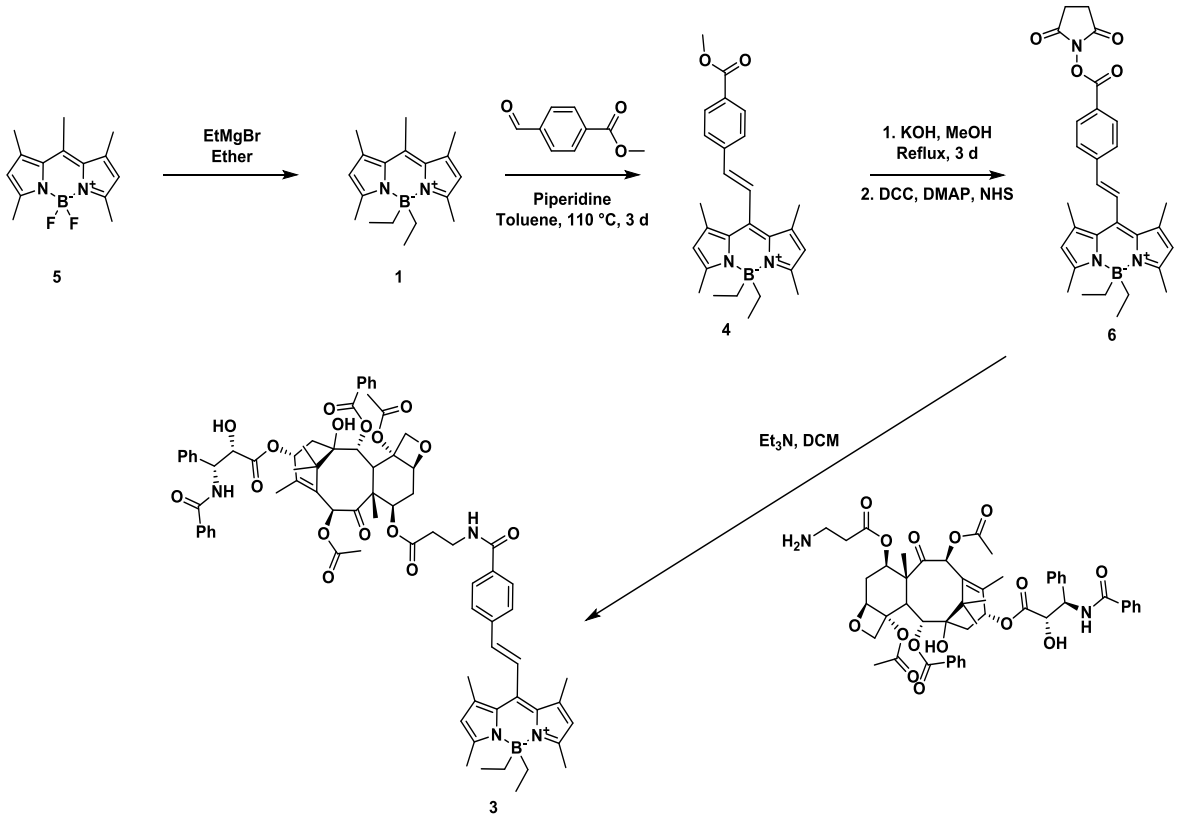

Scheme S3.1 Synthesis of BODIPY-paclitaxel conjugate for use in single molecule localization microscopy (SMLM).

B,B-diethyl-1,3,5,7,8-pentamethyl BODIPY (1): To a solution of 1,3,5,7,8-pentamethylBODIPY **5** (200 mg, 0.76 mmol, 1 eq) stirring in 10 mL dry ether under argon was added 3M ethylmagnesium bromide (2.5 mL, 10 eq.) dissolved in dry THF. The solution was stirred for 2 h at room temperature. The reaction was quenched with a small portion of saturated ammonium chloride and washed 3 times with ammonium chloride and once with brine. The combined organic layer was dried over sodium sulfate, filtered, and the solvent was removed

under vacuum. The resulting mixture was purified with silica gel chromatography (hexanes), affording 150 mg (70%) of the bright orange-yellow product. Characterization matched the previously reported compound.[3]

B,B-diethyl-8-(*E*)-(4-(methoxycarbonyl)styryl)**-1,3,5,7-tetramethylBODIPY (4):** To a solution of **1** (100 mg, 0.35 mmol, 1 eq) in 2 mL toluene was added methyl 4-formylbenzoate (500 mg, 3.0 mmol, 8.5 eq) and 1 mL piperidine. The solution was equipped with a dean stark trap and refluxed for 72 h. The toluene was removed under vacuum and the mixture was purified by column chromatography with silica gel (80:20 toluene:DCM), affording **4** as a red solid (70 mg, 47%). ^{1}H NMR (500 MHz, $CDCl_3$) δ, 0.38 (t, *J* = 8, 6 H), 0.83 (q, *J* = 8, 4 H), 2.19 (s, 6 H), 2.47 (s, 6 H), 3.93 (s, 3 H), 6.06 (s, 2 H), 6.70 (d, *J* = 16, 1 H), 7.26 (d, *J* = 16, 1 H), 7.55 (d, *J* = 8, 2 H), 8.07 (d, *J* = 8, 2 H). ^{13}C NMR (500 MHz, $CDCl_3$) δ, 0.04, 9.20, 16.49, 17.68, 52.26, 121.64, 126.38, 126.55, 129.94, 130.34, 131.59, 135.58, 137.36, 139.61, 140.65, 151.77, 166.71; HRMS-ESI (*m/z*): [$C_{27}H_{33}BN_2O_2$] calc, 428.2744; found, 428.2742.

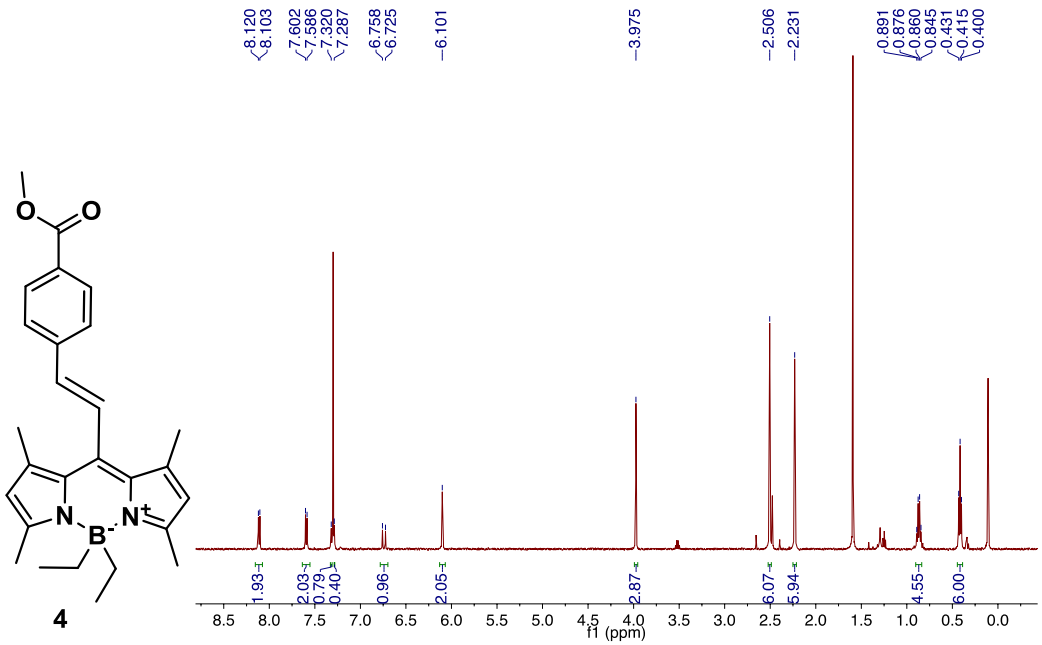

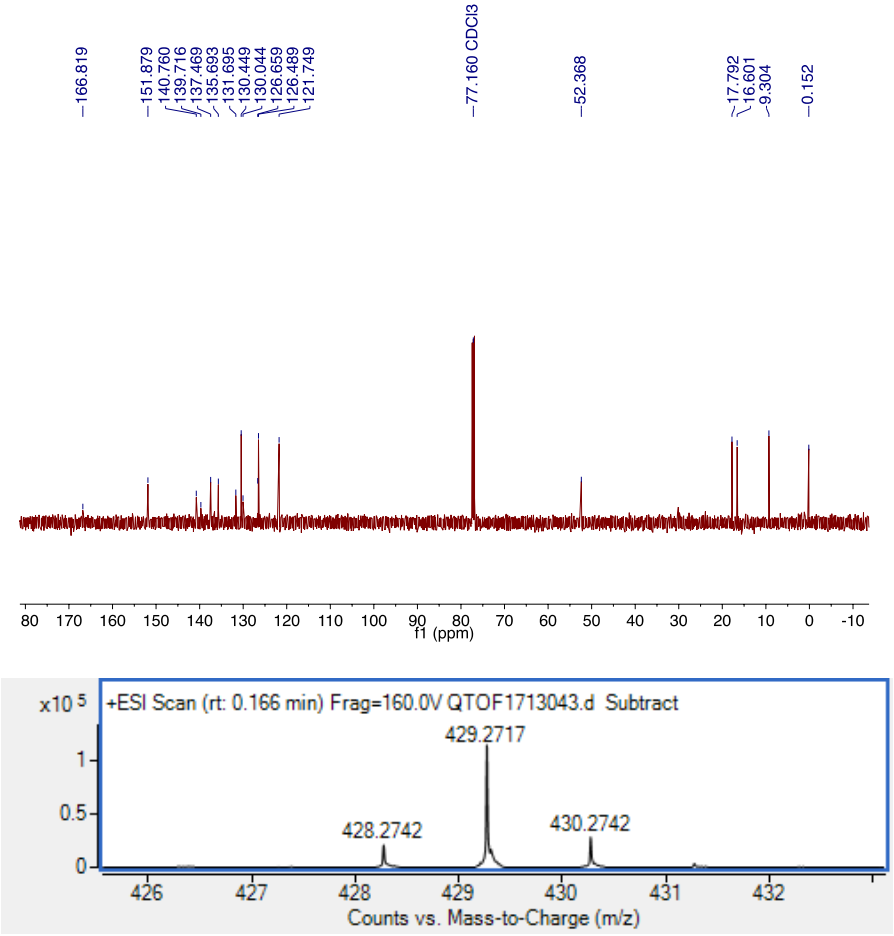

B,B-diethyl-8-(*E*)-(4-(**N-hydroxysuccinamidyl**carbonyl)styryl)**-1,3,5,7-tetramethylBODIPY (6):** To a solution of **4** (50 mg, 0.12 mmol, 1 eq) in 1 mL methanol was added 1 g KOH. The mixture was refluxed for 72 h. The solution was brought to room temperature and acidified with 1 mL HCl, diluted with 10 mL dichloromethane and extracted with dichloromethane 3 times and washed with brine. The organic layer was dried over sodium sulfate, filtered, and the solvent was removed under vacuum to yield 30 mg (60%) of a red solid. The resulting compound was dissolved in dry dichloromethane, to which was added 4-(dimethylamino)pyridine (1 mg, 0.01 mmol, 0.1 eq), dicyclohexylcarbodiimide (22.3 mg, 0.11 mmol, 1.5 eq), and N-hydroxysuccinimide (13 mg, 0.11 mmol, 1.5 eq). The solution was stirred overnight at room

temperature. The mixture was left in the freezer for 1 h, and filtered, after which solvent was removed under vacuum. **6** was purified with silica chromatography (DCM) to yield 17 mg (29% yield over two steps) of a red solid. ^{1}H NMR (500 MHz, $CDCl_3$) δ, 0.42 (t, *J* = 8, 6 H), 0.87 (q, *J* = 8, 4 H), 2.23 (s, 6 H), 2.51 (s, 6 H), 2.96 (s, 4 H), 6.11 (s, 2 H), 6.76 (d, *J* = 16, 1 H) 7.36 (d, *J* = 16, 1 H), 7.66 (d, *J* = 8, 2 H), 8.22 (d, *J* = 8, 2 H). ^{13}C NMR (500 MHz, $CDCl_3$) δ, 0.15, 9.30, 16.61, 17.75, 25.84, 121.186, 124.81, 126.84, 128.13, 131.52, 135.21, 137.42, 139.19, 141.78, 142.70, 152.09, 161.62, 169.34. HRMS-ESI (m/z) [$C_{30}H_{34}BN_3O_4$ + H^+] calc, 512.2715; found,512.2732.

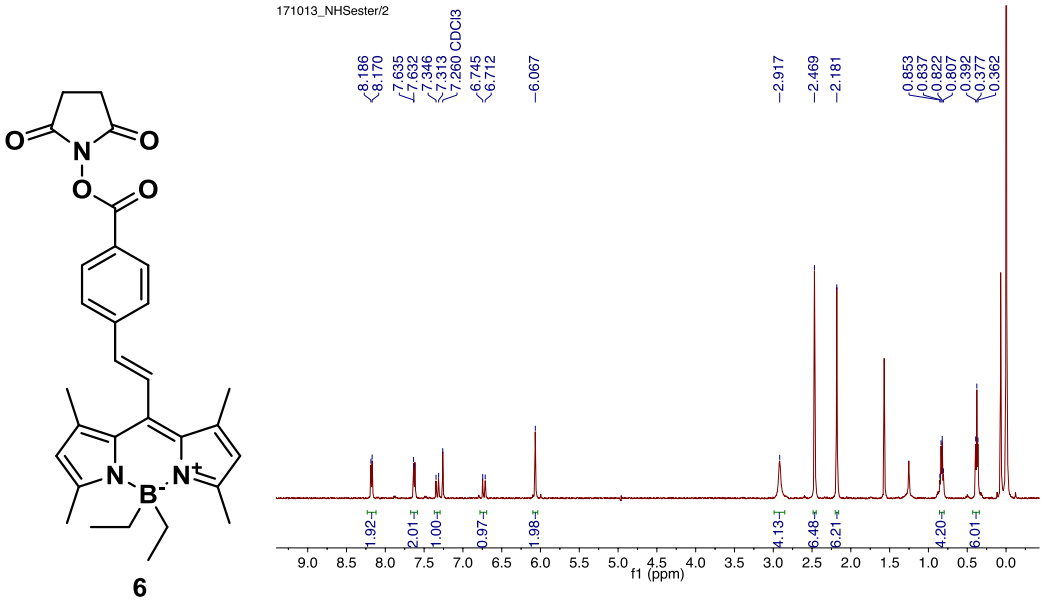

6

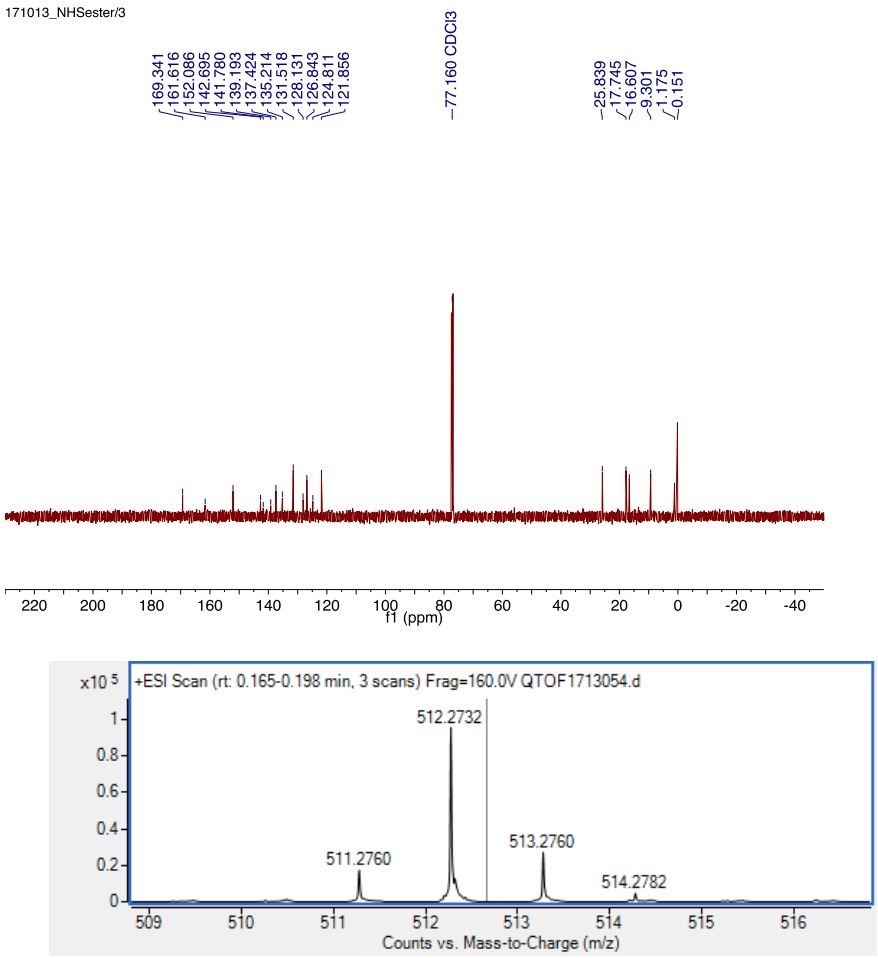

Compound 3: To a solution of **6** (10 mg, 0.02 mmol, 1 eq) stirring in 5 mL dry dichloromethane was added 7-β-alanyltaxol (20 mg, 0.022 mmol, 1.1 eq) and 100 µL triethylamine. The solution was stirred 12 h at room temperature. The solvent was removed under vacuum and the solid was purified by column chromatograpy (99:1 DCM:MeOH) yielding 7 mg of **3** (26% yield). The solid was additionally purified by prep-HPLC for use in fluorescent imaging studies. ^{1}H NMR (500 MHz, $CDCl_3$) δ, 0.37 (t, *J* = 8, 6 H), 0.83 (q, *J* = 8, 4 H), 1.14 (m, 6 H), 1.68 (s, 3 H), 1.85-2.05 (m, 2 H), 1.99 (s, 3 H), 2.13 (s, 1 H), 2.18 (s, 6 H), 2.23 (s, 3 H), 2.36 (s, 3 H), 2.47 (s, 6 H), 2.49-2.62 (m, 3 H), 3.15 (m, 1 H), 3.35 (s, 1 H), 3.83 (m, 1 H), 4.20 (d, *J* = 9, 1 H), 4.32 (d, *J* =

9, 1 H), 4.98 (m, 1 H), 5.68 (m, 2 H), 6.05 (m, 3 H), 6.28 (m, 2 H), 6.70 (d, *J* = 20, 1 H), 7.00 (d, *J* = 9, 1 H,) 7.17 (m, 2 H), 7.30-7.65 (band, 13 H), 7.76 (d, *J* = 8, 2 H), 8.03 (d, *J* = 9), 8.13 (d, *J* = 8, 2 H)). ^{13}C NMR (500 MHz, $CDCl_3$) δ, 8.86, 9.29, 9.77, 14.26, 15.06, 16.60, 17.76, 20.97, 22.85, 25.10, 25.79, 29.86, 32.09, 34.12, 43.35, 46.51, 49.35, 56.14, 58.71, 72.09, 72.30, 73.39, 74.91, 75.30, 75.77, 76.60, 79.44, 81.25, 84.63, 121.86, 126.79, 127.07, 127.24, 128.82, 128.92, 129.32, 130.37, 130.77, 131.66, 132.18, 132.95, 133.85, 133.90, 135.38, 137.10, 137.38, 139.37, 141.80, 143.02, 152.09, 156.84, 165.35, 167.23, 168.24, 169.94, 171.41, 173.58, 203.96; HRMS-ESI (*m/z*) [$C_{76}H_{85}BN_4O_{16}$ + H^+] calc, 1321.6126; found, 1321.6146.

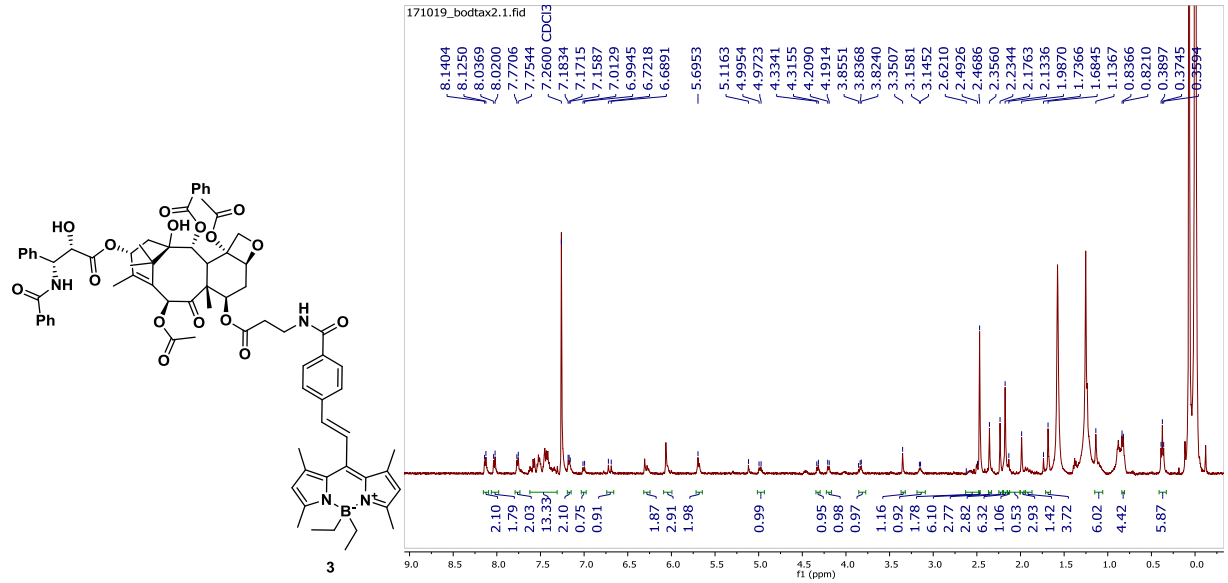

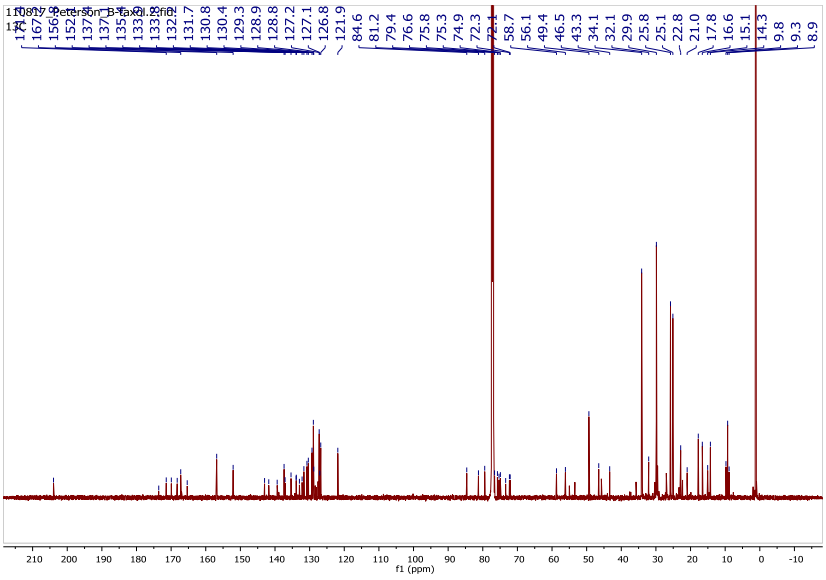

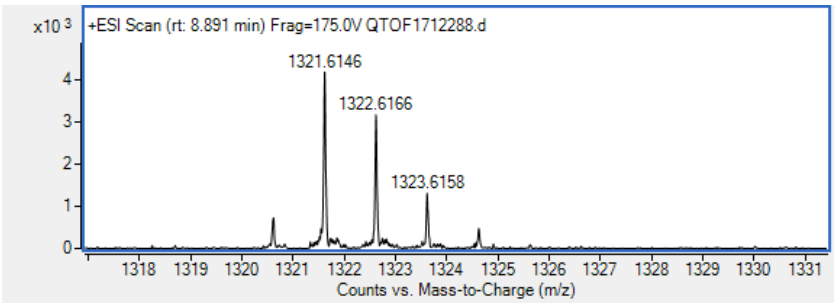

3.7.2 Fluorescence and Photoactivation Quantum Yield Measurements

Fluorescence quantum yields (Φ_f)

Fluorescence quantum yields were determined as an average of three trials. Compounds **1**-**3** were prepared in methanol at concentrations between 1-30 µM and the absorbance spectra and fluorescence spectra with 450 nm excitation were collected. Calibration plots were constructed using the integrated fluorescence peak area from 475-600 nm versus the absorbance at 450 nm. Calibration curves were compared to those for a fluorescein standard. In addition, the quantum yield of the aqueous photoproduct of **1** was determined by irradiating a solution of **1** in 90:10

acetonitrile: water for 30 minutes. As described above, the calibration curve was plotted using the integrated fluorescence peak area from 475-600 nm and the absorbance at 450 nm.

Photoactivation quantum yield

The photoactivation quantum yield was determined using an average of three trials. Compounds **1** and **4** (an analogue of **3** without paclitaxel attached) between 1-4 mg were dissolved in 1 mL dichloromethane and diluted to 25 mL with methanol, or 45 mL acetonitrile and diluted to 50 mL with water. 3 mL of the solutions were transferred to a quartz cuvette. The initial absorbance was recorded at 532 nm. The solutions were then irradiated with a 532 nm Nd:YAG laser or a 530 nm 5 lamp Luzchem LED setup. At intervals, 10 µL of the solutions were removed and diluted to 25 mL with methanol or 90:10 acetonitrile:water and the fluorescence intensity at 510 nm was measured with 450 nm excitation. Time points were taken until the fluorescence began to decrease due to photobleaching, at which time it was assumed that the maximum fluorescence intensity was 100% conversion. The percent conversion was converted into moles reacted, which was plotted versus irradiation time. The photoactivation quantum yield was determined against a ferrioxalate actinometer, taking into account the low absorbance of compounds **1**, **4** and ferrioxalate at 532 nm. The quantum yield of photoactivation for compound **1** was 0.79 ± 0.02% in methanol and 0.8 ± 0.1% in 90:10 acetonitrile: water. The quantum yield of photoactivation for **4** was found to be 0.12 ± 0.02% in 90:10 acetonitrile: water. Compound 4 was used instead of compound 3 because synthesis of milligram quantities of compound 3 was not feasible.

Photoproduct studies

Compound **1** (25 mg) was dissolved in 10 mL dichloromethane, which was diluted to 100 mL with methanol. The solution was stirred in an Erlenmeyer flask overnight under a 532 nm LED. The solvent was removed under vacuum and the remaining solid was purified via column chromatography with silica gel (60:40 Hex: EtOAc). Two major photoproducts were isolated and

characterized by NMR (Figure S1), corresponding to the single and disubstituted compounds. 2 mg (8% yield) of **7** and 21 mg (83% yield) of **2** were isolated, suggesting that the photoactivation to **2** is a sequential two-photon process.

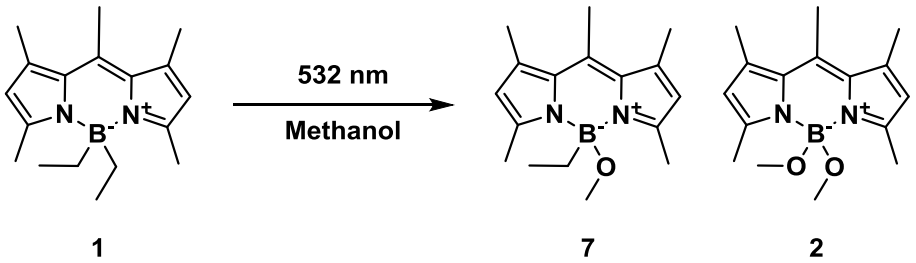

Scheme S3.2 Photoproducts of **1** in methanol when irradiated with green light.

The solubility of **1** in water is low, so verification that the dihydroxy product is formed in water was performed by collecting a mass spectrum of the compound after irradiation in 90:10 acetonitrile: water. Photoproduct studies were conducted by dissolving 1 mg of **1** in 9 mL of acetonitrile to which was added 1 mL of water. The solution was irradiated in a pyrex test tube with green light for 3 h. A high resolution mass spectrum (HRMS, Figure S2) was measured of the solution to confirm that the dihydroxy species is formed upon irradiation in water. HRMS, ESI: C_{14} H_{19} B N_2 O_2 Na + Calc: 281.1437 Found: 281.1431

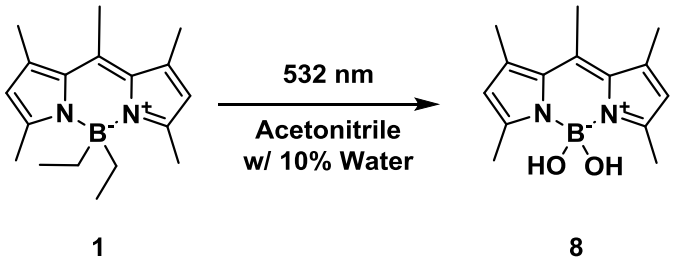

Scheme S3.3 Photoproduct of **1** when irradiated with green light in acetonitrile with 10% water.

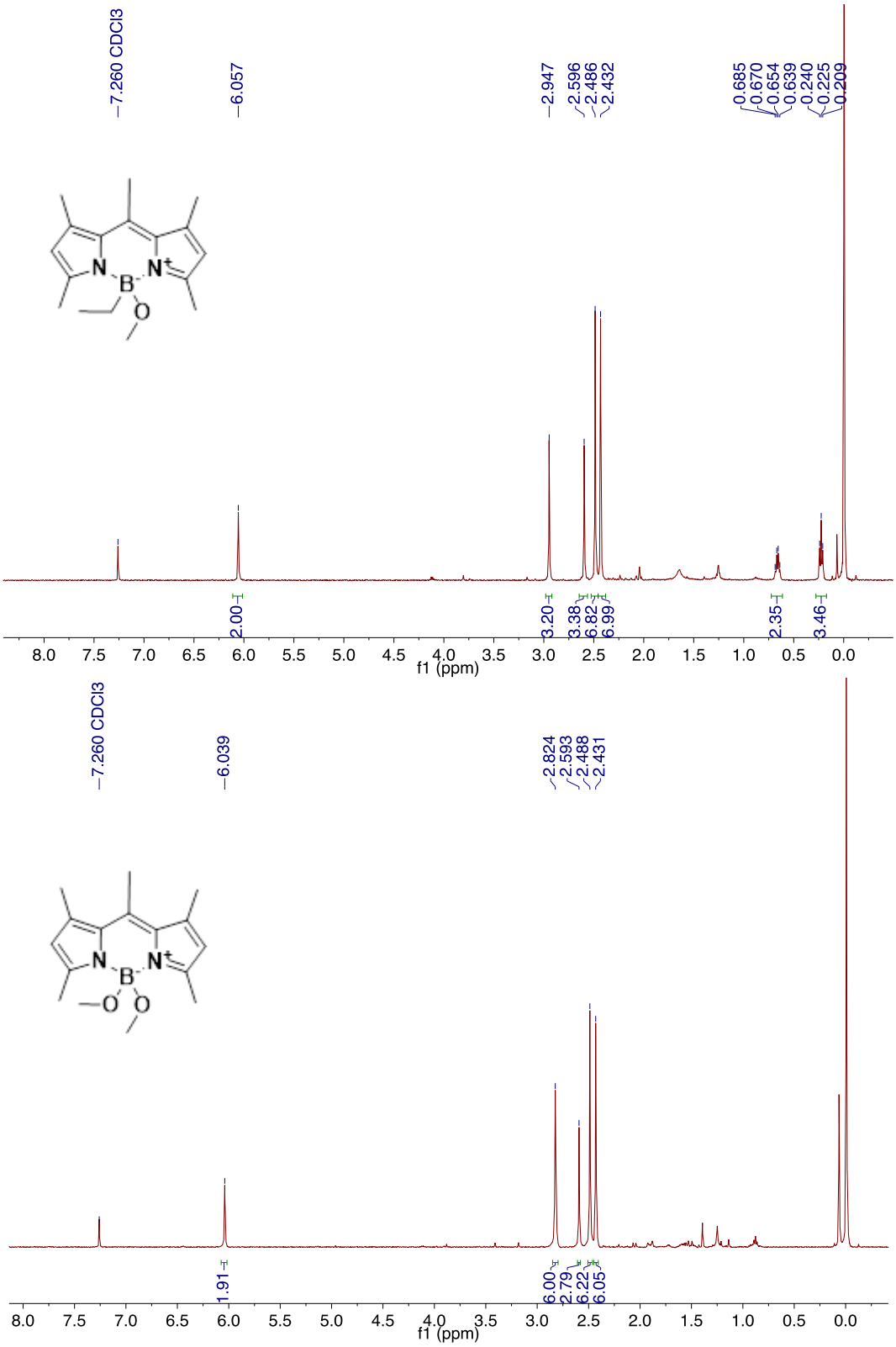

Figure S3.1 NMR spectra of the photoproducts of **1** in methanol: (top) **7** and (bottom) **2**.

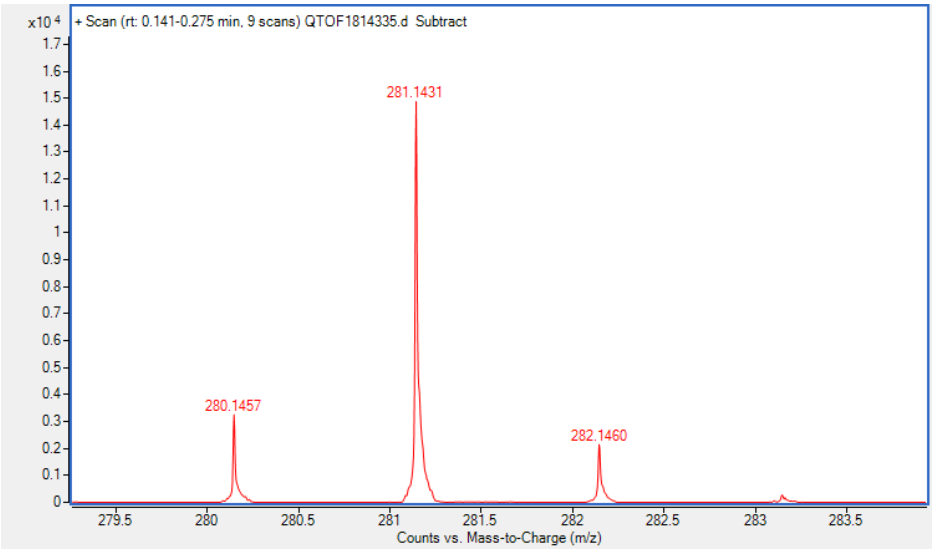

Figure S3.2 High resolution mass spectrum of the photoproduct of **1** in an aqueous medium showing the formation of the dihydroxy product **8**.

3.7.3 Single Molecule Localization Microscopy

Table S3.1 Examples of the laser irradiances used for SMLM experiments with commonly used photoswitchable fluorescent probes.

SMLM probe	Excitation Laser irradiance used for SMLM experiments	Reference
Alexa Fluor 488	1.2 kW/cm^2, 3 kW/cm^2	[4] [5]
ATTO 488	1.2 kW/cm^2	[4]
ATTO 520	3 kW/cm^2	[5]
Alexa Fluor 532	1.5 kW/cm^2	[5]
ATTO 532	10 kW/cm^2	[6]
Tetramethyl Rhodamine	~ 1 kW/cm^2	[7]
Cy3B	1.7 kW/cm^2, 2.2 kW/cm^2	[8] [4]
ATTO 565	1.5 kW/cm^2	[5]
Alexa Fluor 568	1.5 kW/cm^2	[5]
ATTO 590	4 kW/cm^2	[5]
ATTO 655	1.5 kW/cm^2	[9]
Alexa Fluor 647	0.8 kW/cm^2	[4]
Cy5	0.8 kW/cm^2	[4]
ATTO 680	0.8 kW/cm^2	[4]
ATTO 700	4 kW/cm^2	[5]
Cy7	1.3 kW/cm^2	[4]
Alexa Flour 750	1.3 kW/cm^2	[4]

Table S3.2 Examples of the laser wavelengths and irradiances used for SMLM experiments with photoactivatable fluorescent probes.

Probe	Activation wavelength	Probe λ_{ex}	Probe λ_{em}	Activation laser irradiance	Excitation laser irradiance	Reference
Compound **3**	488 nm	498 nm	517 nm	0.16 kW/cm^2	NA	This study
NVOC caged si-Rhodamine	405 nm	637 nm	654 nm	1 W/cm^2	4 kW/cm^2	[10]
Rhodamine diazoketone	405 nm	558 nm	583 nm	0.1 W/cm^2	2 kW/cm^2	[11]
Caged Rh110	405 nm	473 nm	520 nm	5.5-23 W/cm^2	0.38 kW/cm^2	[12]
Nitroso-caged rhodamine	405 nm	532 nm	550 nm	0.1 W/cm^2	2 kW/cm^2	[13]
Rhodamine lactam	375 nm	532 nm	620 nm	50 W/cm^2	18 kW/cm^2	[14]
Coumarin oxazine	355 nm	532 nm	645 nm	10-100 W/cm^2	5 kW/cm^2	[15]

Data collection and analysis

Microscopy experiments were performed on a Nikon Eclipse TE2000U microscope (Melville, NY) equipped with an Argon ion laser (Uniphase, San Jose, CA). A schematic of the instrument is shown below. The laser irradiance was determined as previously reported.[16] An Andor iXon^{EM}+ DU-897 back illuminated electron-multiplying charge coupled device (EMCCD) was used to collect the filtered emitted light. A 30 ms acquisition time per frame and 10,000 - 50,000 frames were collected for each movie. SMLM movies were analyzed using ThunderSTORM plug-in for ImageJ.[17] Fitting point spread function model, integrated Gaussian by least square methods was used to achieve the sub-pixel localization of molecules. Merging was used to remove the localized molecules that appeared in sequential frames. This ensured that the same

localized molecule did not contribute to the constructed SMLM image more than once. Diffracted limited images were constructed by summing all the frames into a single image using ImageJ.

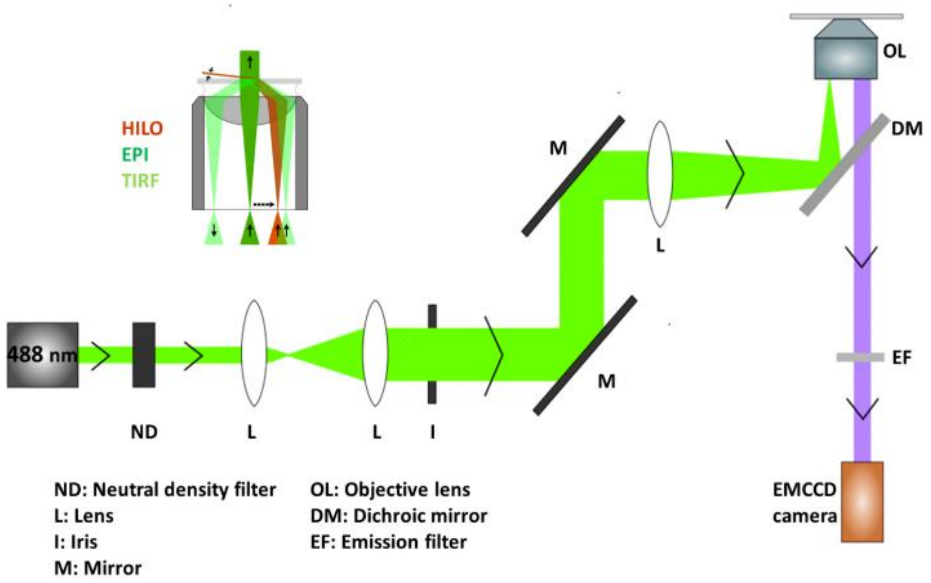

A schematic of the fluorescence microscope used for single molecule localization microscopy.

Uncertainty of the localized single molecules (s) is calculated using the equation:

$$\sigma = \sqrt{\left(\frac{s^2}{N}\right) + \left(\frac{a^2/12}{N}\right) + \left(\frac{8\pi s^4 b^2}{a^2 N^2}\right)}$$

where s is the standard deviation of the point spread function, N is the number of photons detected, a is the pixel size, and b is the standard deviation of the image background[18]. For our experimental conditions, the expected localization prevision is between 14-22 nm.

Cell sample preparation

HeLa cells (ATCC® CCL-2™, Manassas, VA) were cultured in Dulbecco's Modified Eagle Medium (DMEM, Invitrogen, Carlsbad, CA) supplemented with 10% fetal bovine serum, 12.5

mM streptomycin, and 36.5 mM penicillin (Fisher Scientific, Pittsburgh, PA). Cultures were maintained at 37 °C in a humidified 5% CO_2 incubator (Thermo Scientific, Waltham, MA). HeLa cells were sub-cultured using 0.25% (w/v) trypsin-EDTA (Life Technologies, Carlsbad, CA) solution every two days. Cells were seeded at 20,000 cells per well onto polylysine coated, 8-well chambered cover glass (Nunc™ Lab-Tek™ II, Thermo Scientific) a day before the microscopy experiment.

Live cell labeling

On the day of the microscopy experiment, the growth medium was replaced with 1 μM compound **3** and 25 μM verapamil hydrochloride (Sigma Aldrich, St. Louis, MO) in DMEM medium and incubated for 1 hour at 37 °C in a humidified 5% CO_2 incubator. Cells were rinsed with the imaging medium (pH = 7.4, 155 mM NaCl, 5 mM KCl, 2 mM $CaCl_2$, 1 mM $MgCl_2$, 2 mM NaH_2PO_4, 10 mM HEPES and 10 mM Glucose) several times prior to the microscopy experiment.

Glutaraldehyde fixation of cells and labeling

Growth medium was removed, and the cells were incubated in BRB-80 buffer (pH 6.8, 80 mM K-PIPES, 1 mM $MgCl_2$; 1 mM EGTA) containing 0.5% Triton X-100 for 1 min. Then cells were incubated for 10 min with BRB buffer containing 0.5% glutaraldehyde (Sigma Aldrich). Solution was replaced with a freshly prepared 0.1% sodium borohydride in PBS buffer and incubated for 5 min. This step was repeated twice to quench the unreacted glutaraldehyde. Then rinsed well with PBS and blocked with 1% BSA in PBS for 30 min. Samples were incubated for 1-2 h with 1 μM compound **3** in PBS. The cells were washed several times with PBS and imaged in PBS buffer.

Ethyleneglycol-bis-succinimidyl-succinate (EGS) fixation of cells and labeling

Growth medium of the cells was replaced with 0.5% Triton X-100 in BRB-80 buffer and incubated for 1 min. Then 2 mM ethyleneglycol-bis-succinimidyl-succinate (EGS) (Thermo Scientific) in BRB-80 buffer (freshly prepared from 250 mM EGS in DMSO) was added into the cells by replacing the previous solution and incubated for 10 min. The solution was removed and rinsed with PBS. Then, the samples were incubated with 1 μM compound **3** in PBS for 1h. The cells were rinsed several times with PBS and imaged in PBS buffer.

In vitro assembled microtubule preparation

A 2 mM stock of compound **3** was prepared in DMSO and 5 μL of this stock was added to 0.5 mL of BRB-80 buffer. This solution was added to a vial of 500 μg lyophilized microtubules (mt002, Cytoskeleton, Denver, CO). The solution was mixed gently and incubated for 15 minutes at room temperature. An 8-well chambered cover glass was sonicated for 10 minutes in 1 M potassium hydroxide (KOH) solution, then rinsed several times with Milli-Q water and air dried overnight. The microtubule solution (50 μL) was added into the well and incubated for 15 minutes. The solution was removed and the immobilized microtubules on the cover glass were fixed with 0.5% glutaraldehyde in BRB-80 buffer for 10 minutes. The fixation solution was removed and a freshly prepared 0.1% sodium borohydride in PBS was added into the well and incubated for 5 minutes. The well was rinsed with PBS and imaged in PBS buffer.

Single molecule sample preparation

A 8-well chambered cover glass was cleaned by sonicating for 10 minutes in 1 M potassium hydroxide (KOH) solution, then several times rinsing with Milli-Q water followed by air drying for overnight. Compound **3** was dissolved in spectrophotometric grade ethanol (Fisher Scientific) and diluted to obtain a final concentration of ~ 0.1 μM. This solution (100 μL) was added into

the well and after 10 minutes, the well was rinsed several times with PBS and imaged in PBS medium.

3.7.4 Additional Figures

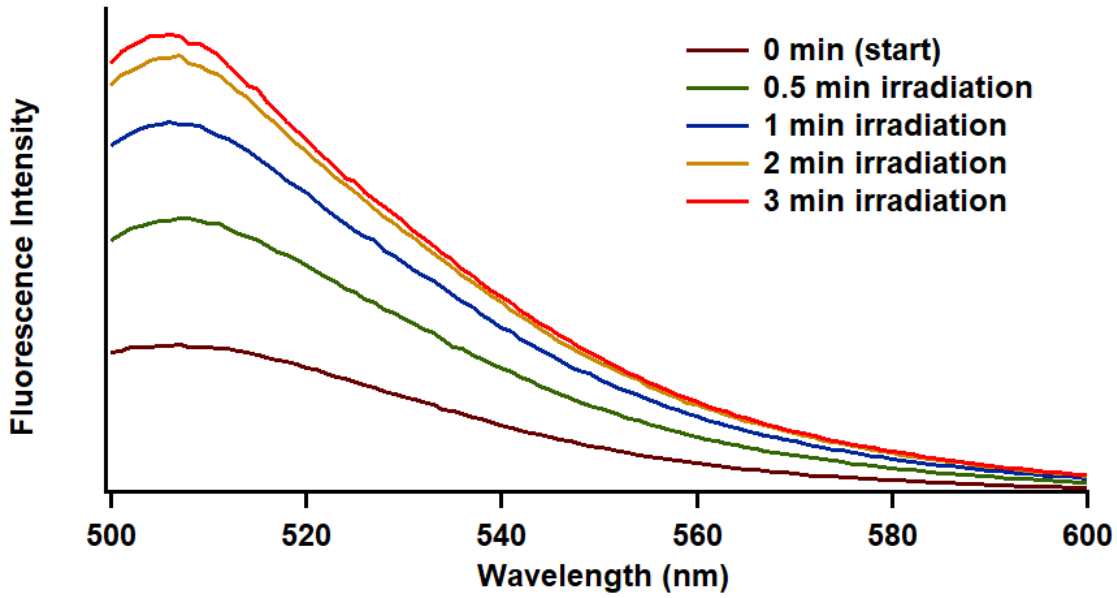

Figure S3.3 Fluorescence increase of compound **1 (5 µM)** in PBS buffer in a quartz cuvette. The cuvette was irradiated with a polychromatic halogen lamp and the emission spectra were collected after the time periods indicated in the figure.

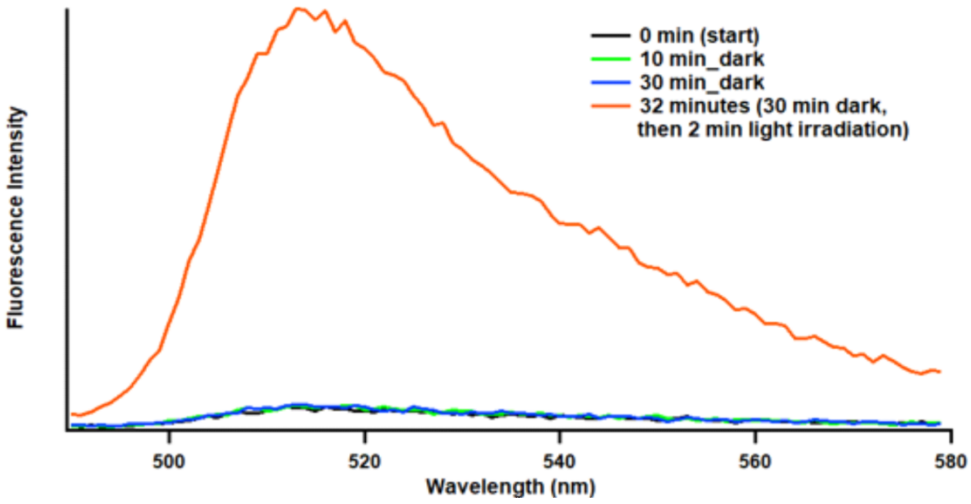

Figure S3.4 Fluorescence spectra collected by dissolving 5 μM compound **3** in PBS buffer in a quartz cuvette. The cuvette was kept in dark and the time measuring was started at 0 min. Emission spectra were collected after 10 min and 30 min. After keeping the cuvette in the dark for 30 minutes, it was irradiated for 2 minutes with a polychromatic halogen lamp and the emission spectrum was collected.

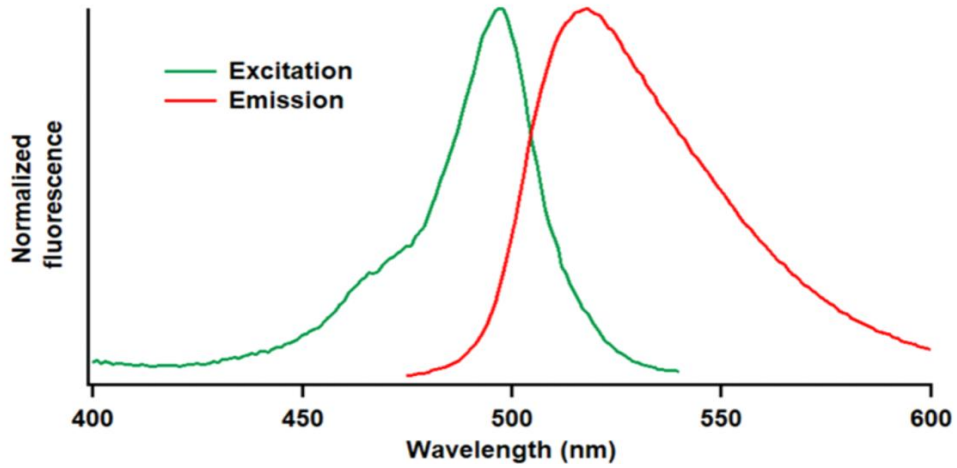

Figure S3.5 Excitation and emission spectra of Compound **3** after irradiation for 30 minutes with a polychromatic halogen lamp. The excitation spectrum was collected using a fixed 550-nm emission wavelength, and the emission spectrum was collected using a fixed 450-nm excitation wavelength.

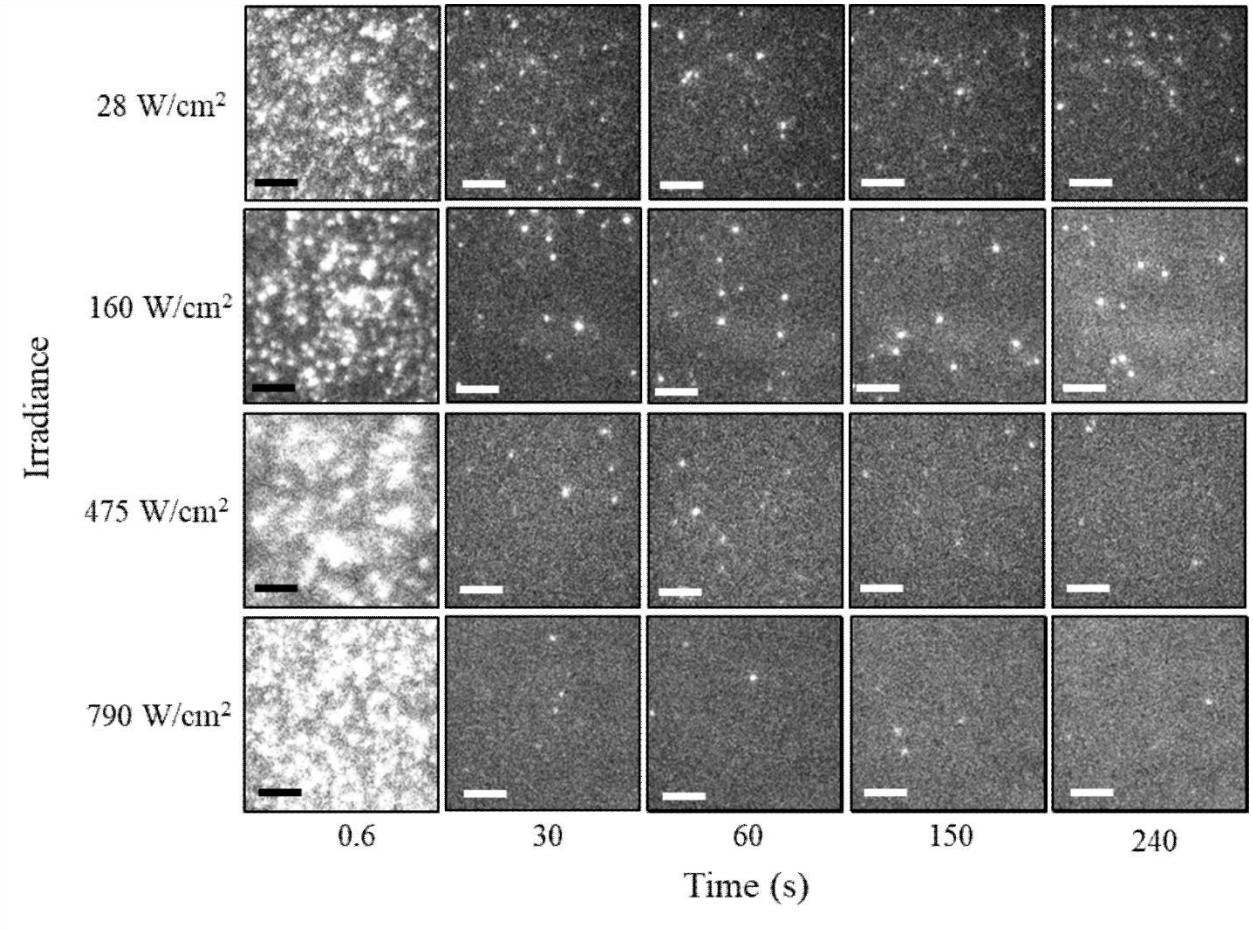

Figure S3.6 Selected frames from movies collected at 28, 160, 475, and 790 W/cm^2 laser irradiances. Compound **3** was adsorbed on a cover glass and imaged in PBS buffer. The fluorescence signal is a result of the photoactivation of Compound **3**. Time 0.6 s shows the photoactivation of numerous molecules with the amount increasing with laser irradiance. At later times (after 3 s), the photoactivation events are sparse enough for accurate localization. All images are shown using the same intensity scale. Scale bar is 3 μm.

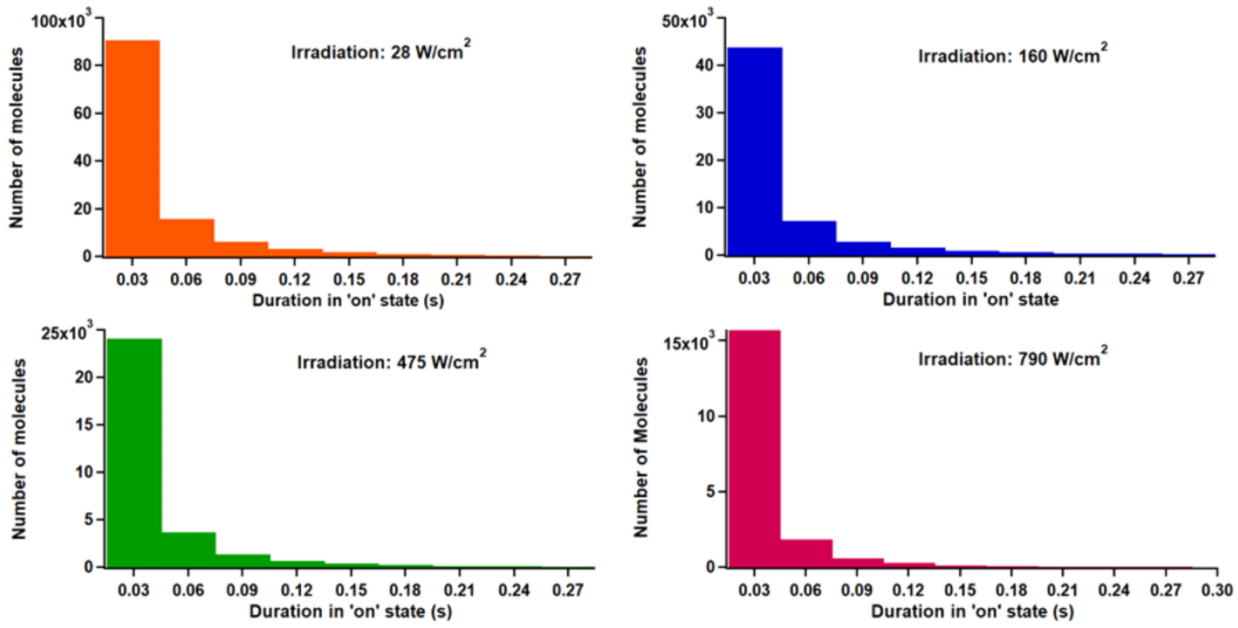

Figure S3.7 Histograms of the time photoactivated compound **3** was in the 'on' state for each laser irradiance. Each frame in the movie was captured using a 0.03 s acquisition time (i.e., most molecules were in the 'on' state for only one frame).

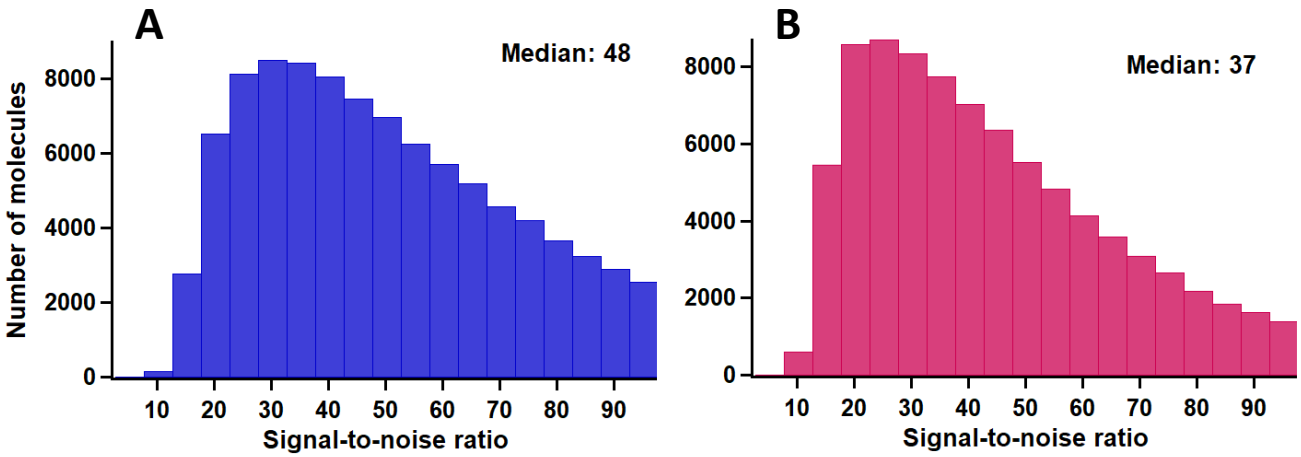

Figure S3.8 Histograms of signal-to-noise ratio of compound 3 (A) adsorbed on a cover glass and (B) bound to microtubules in HeLa cells and imaged using a 488-nm laser line. The median values of the distributions are (A) 48 and (B) 37.

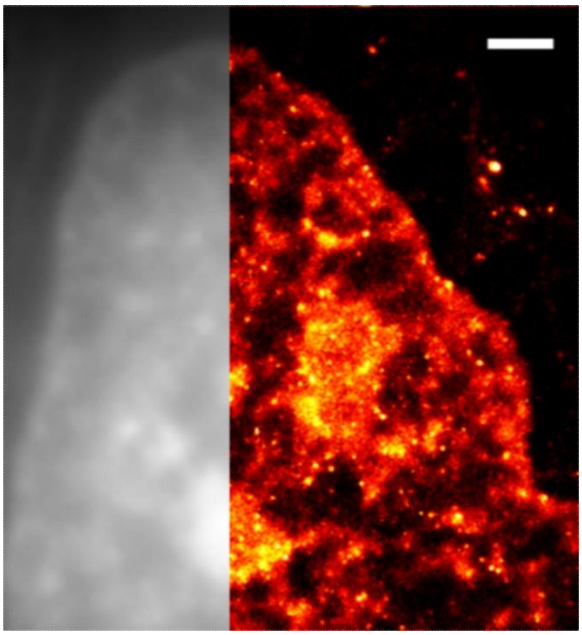

Figure S3.9 SMLM image of the nuclear area of a glutaraldehyde fixed HeLa cell labeled with compound **3** (color scale). The gray scale image is the diffraction-limited image generated by summing all the images in the movie without localizing the fluorophores. PBS buffer was used as the imaging medium. Scale bar is 1 μm.

3.7.5 References for Supplementary Information

1. S. B. Choi, J.; Kim, Y., *Chemical Science* **2014**, *5*, 751-755.
2. R. Guy, Z. Scott, R. Sloboda, K. Nicolaou, *Chem Biol* **1996**, *3*, 1021-1031.
3. A. B. More, S. Mula, S. Thakare, N. Sekar, A. K. Ray, S. Chattopadhyay, *J Org Chem* **2014**, *79*, 10981-10987.
4. G. T. Dempsey, J. C. Vaughan, K. H. Chen, M. Bates, X. Zhuang, *Nat Methods* **2011**, *8*, 1027-1036.
5. M. Heilemann, S. van de Linde, A. Mukherjee, M. Sauer, *Angew Chem Int Ed Engl* **2009**, *48*, 6903-6908.
6. J. Folling, M. Bossi, H. Bock, R. Medda, C. A. Wurm, B. Hein, S. Jakobs, C. Eggeling, S. W. Hell, *Nat Methods* **2008**, *5*, 943-945.

7. T. Klein, A. Loschberger, S. Proppert, S. Wolter, S. van de Linde, M. Sauer, *Nat Methods* **2011**, *8*, 7-9.

8. M. Lehmann, G. Lichtner, H. Klenz, J. Schmoranzer, *J Biophotonics* **2016**, *9*, 161-170.

9. S. A. Jones, S. H. Shim, J. He, X. Zhuang, *Nat Methods* **2011**, *8*, 499-508.

10. J. B. Grimm, T. Klein, B. G. Kopek, G. Shtengel, H. F. Hess, M. Sauer, L. D. Lavis, *Angew Chem Int Ed Engl* **2016**, *55*, 1723-1727.

11. B. Roubinet, M. Bischoff, S. Nizamov, S. Yan, C. Geisler, S. Stoldt, G. Y. Mitronova, V. N. Belov, M. L. Bossi, S. W. Hell, *J Org Chem* **2018**, *83*, 6466-6476.

12. D. Pan, Z. Hu, F. Qiu, Z. L. Huang, Y. Ma, Y. Wang, L. Qin, Z. Zhang, S. Zeng, Y. H. Zhang, *Nat Commun* **2014**, *5*, 5573.

13. H. He, Z. Ye, Y. Zheng, X. Xu, C. Guo, Y. Xiao, W. Yang, X. Qian, Y. Yang, *Chem Commun (Camb)* **2018**, *54*, 2842-2845.

14. J. Folling, V. Belov, R. Kunetsky, R. Medda, A. Schonle, A. Egner, C. Eggeling, M. Bossi, S. W. Hell, *Angew Chem Int Ed Engl* **2007**, *46*, 6266-6270.

15. E. Deniz, M. Tomasulo, J. Cusido, I. Yildiz, M. Petriella, M. L. Bossi, S. Sortino, F. M. Raymo, *J Phys Chem C* **2012**, *116*, 6058-6068.

16. S. van de Linde, A. Loschberger, T. Klein, M. Heidbreder, S. Wolter, M. Heilemann, M. Sauer, *Nat Protoc* **2011**, *6*, 991-1009.

17. M. Ovesny, P. Krizek, J. Borkovec, Z. Svindrych, G. M. Hagen, *Bioinformatics* **2014**, *30*, 2389-2390.

18. R. E. Thompson, D. R. Larson, W. W. Webb, *Biophys J* **2002**, *82*, 2775-2783.

CHAPTER 4. EFFECT OF AMYLOID BETA 1-40 AND 1-42 PEPTIDES ON THE LATERAL DIFFUSION AND SIGNALING OF RECEPTOR FOR ADVANCED GLYCATION ENDPRODUCTS (RAGE)

Chamari S. Wijesooriya and Emily A. Smith*

Department of Chemistry, Iowa state University, Ames, IA, 50011, United States

Manuscript in preparation

4.1 Introduction

The receptor for advanced glycation endproducts (RAGE) is a pattern-recognition receptor that belongs to the immunoglobin superfamily of cell surface molecules.[1-2] This transmembrane receptor has an extracellular domain consisting of a variable type domain (the V domain) and two constant type domains resembling immunoglobulin-like structures (the C1 and C2 domains), a single transmembrane-spanning region, and a short cytoplasmic domain. RAGE plays a major role in several chronic inflammatory and neurodegenerative disorders such as diabetes,[3] atherosclerosis,[4] rheumatoid arthritis,[5] cancer,[6] Alzheimer's disease,[7-9] multiple sclerosis[10] and stroke.[11] This receptor binds with various types of chemically-distinct ligands including advanced glycation endproducts (AGE),[12] S100/calgranlins protein family members,[13-14] high mobility group box 1 protein (HMGB1),[15] β_2-integrins[16] and amyloid beta peptides.[17] X-ray crystallographic, nuclear magnetic resonance and biochemical data showed that electrostatic interactions between the positively charged surfaces of V and C1 domains and negatively charged ligands is the main factor for the multi-ligand binding ability of the RAGE receptor.[18]

Amyloid beta peptides, consisting of various amino acid chain lengths, are derived from the transmembrane amyloid precursor protein. Two of the most prevalent forms are the 1-40 and 1-42 peptide fragments (Figure 1). Although they differ in only an extra two amino acids at the

c-terminus of the 1-42 peptide, their oligomerization tendency and mechanism are very different.[19-20] Amyloid beta 1-42 tends to form an equilibrium between monomers and pentamers/hexamers as well as larger sized oligomers. Initial oligomerization of amyloid beta 1-40 involves an equilibrium between monomers, dimers, trimers, and tetramers. These forms have different electrostatic properties, therefore they have different binding affinities with various cell membrane components.[21] Both of these fragments are known to interact with RAGE protein and also play a major role in Alzheimer's disease.[22] RAGE mediates the transport of amyloid beta peptides across the blood-brain barrier and their accumulation in the brain;[7] and their related signaling pathways promote neuronal dysfunction.[23] The binding of amyloid beta with RAGE generates a positive feedback mechanism that promotes the RAGE-amyloid beta interaction by expressing more RAGE on the cell membrane, thus enhancing the Amyloid beta toxicity.[24] RAGE expression is elevated in neurons, microglial cells, and astrocytes during Alzheimer's disease, wherein the accumulation of amyloid beta is observed.[22]

Based on molecular modeling studies, it is suggested that the negatively charged residues located in the N-terminal side of the amyloid beta peptides (3, 7 and 11 positions of the amino acid sequence) are the binding partners with the RAGE V-domain; furthermore, it is assumed that the dimeric amyloid beta peptides are interacting with the RAGE oligomers.[25] There are several reports of RAGE interacting with amyloid beta peptides and the resulting effect on cellular signaling pathways and cellular dysfunction.[22, 26-28] The effect of these peptides on RAGE diffusion is, however, not yet known. RAGE's diffusion properties may correlate to its intermolecular interactions, signal transduction, and the cellular mechanisms related to the receptor-ligand binding.[29-31] The purpose of this study is to measure the lateral diffusion properties of RAGE protein in the presence of amyloid beta 1-40 and 1-42 peptides and to show

how these parameters correlate with ligand-mediated intracellular signaling. Fluorescence-based methods are commonly used to measure membrane protein diffusion. Diffusion properties measured by fluorescence recovery after photobleaching (FRAP) and fluorescence correlation spectroscopy (FCS) generally provide an ensemble average value of a large population of membrane proteins, and do not represent the variation of single protein diffusion on the membrane. To overcome this issue, a single particle tracking method is used for this study, where single RAGE receptors are labeled with quantum dots and each receptor is individually measured. Amyloid-beta-mediated RAGE downstream pathways include the activation of p38 mitogen activated phospho kinase (p38 MAPK)[32], which is measured by protein gel electrophoresis and Western blotting methods.

4.2 Materials and Methods

4.2.1 Cell Culture

Human embryonic kidney cell line (HEK293) from American Type Culture Collection (ATCC: CRL-1573) was used for all cellular experiments. HEK293 cell line was maintained in Dulbecco's modified Eagle's medium (DMEM) (Sigma Aldrich) supplemented with 10% fetal bovine serum, 12.5 mM streptomycin and 36.5 mM penicillin (Fisher Scientific, Pittsburgh, PA) at 37 °C and 5% CO_2 in a humidified incubator (Thermo Scientific, Waltham, MA). HEK293 cells expressing N-terminal hemagglutinin tagged RAGE (hereafter, RAGE cell line) was prepared as previously described.[33] This cell line was maintained in medium containing 400 µg/mL geneticin G418 (Santa Cruz Biotechnology). These cell lines were subcultured every 3 days using a 0.25% (w/v) trypsin-EDTA (Life Technology, Carlsbad, CA) solution.

4.2.2 Ligand Preparation

Amyloid beta 1-40 (A1075) and 1-42 (A9810) peptides were purchased from Sigma Aldrich and dissolved separately in DMSO to a concentration of 0.05 mM. Aliquots were stored

at -20 °C. On the day of the experiment, stock solutions were diluted in 3% BSA-DMEM to obtain the desired concentration of the peptides.

4.2.3 Single Particle Tracking Studies

HA-tagged RAGE expressed on the HEK293 cell membrane were specifically labeled with anti-HA labeled quantum dots (AHA-QDs) for single particle tracking studies. These AHA-QDs were prepared as previously reported.[33] Nunc™ Lab-Tek™ chambered glass slides with 8 wells were pre-treated with 0.01% poly-L-lysine (Sigma Aldrich) sterile solution for 15 minutes, washed with autoclaved de-ionized water and air dried. Cells were subcultured onto these chambered glass slides for 24 hours, then the culture medium was replaced with 3% (w/v) BSA in DMEM medium for 18 hours to cover any of the areas on the glass surface without cell growth. Cells were treated with Amyloid beta 1-40 or 1-42 (5 nM or 10nM in 3% BSA-DMEM medium) for 30 minutes at 37 °C. Cells without ligand treatment were used as the control. Then, cells were incubated with AHA-QDs (diluted to 100 pM in imaging medium containing 0.1% BSA) for 15 minutes at 37 °C. Cells were rinsed five times with imaging medium prior to performing the microscopy experiments.

SPT studies were performed at 36 ± 2 °C using a Nikon Eclipse TE2000U microscope (Melville, NY, USA) operating in wide-field, epi-fluorescence mode and housed inside a home-built thermal chamber. The light from a mercury lamp (X-Cite 120 PC) was filtered through a 425/45 nm excitation filter and focused onto the sample using a 100× 1.49 numerical aperture oil-immersion objective. Emitted light from the illuminated sample was filtered through a 605/20 nm filter and collected by an Andor iXon EM+DU-897 back-illuminated electron-multiplying charge coupled device (EMCCD). Fluorescence signal was collected with a 40 ms camera acquisition time per frame and 700 frames were collected in each data set (movie).

The ImageJ based plugin 2D/3D particle tracker was used to detect and localize the fluorescence signal from the AHA-QDs and to track their movement over time to generate the trajectories.[34-35]

A MATLAB-based application APM_GUI (Analyzing Particle Movement with Graphical User Interface) was used to analyze the trajectories.[36-37] AHA-QDs detected on wild-type HEK293 cells that did not express detectable amounts of RAGE (2 ± 1 QDs per cell) were considered to be nonspecific binding. The average diffusion coefficient calculated for the nonspecific trajectories (0.0018 $\mu m^2/s$)[38] was used as the low cutoff value; the higher values were assumed to represent AHA-QDs bound to RAGE (i.e., specific binding). Mobile trajectories were categorized into Brownian or confined trajectories based on their diffusion probabilities in a given region (Figure 2). When a particle undergoes a non-Brownian diffusive motion within restricted boundaries, this region is considered as a confined domain.[39] Outside the boundaries, particle motion may behave as a Brownian trajectory. The critical confinement index (Lc) and critical confinement time (tc) within boundaries were calculated for a series of simulated Brownian trajectories using relevant experimental parameters, as previously reported.[33] Portions of the trajectory with Lc > 3.16 and tc > 1.95 s were recognized as confined domains. The size of the confinement domains, the duration of the confinement time, and the diffusion coefficients inside and outside the confined domains were calculated for the trajectories with at least one confined domain. For trajectories that did not exhibit confinement (i.e., exhibiting only Brownian diffusion), the global diffusion coefficient (average diffusion coefficient calculated for the total duration of the trajectory) was calculated.

4.2.4 Western Blotting

Wild-type HEK293 cells and cells expressing RAGE were subcultured into T-25 flasks for 2 days. Medium in the flasks was replaced with 3% BSA-DMEM containing amyloid beta 1-

40 or 1-42 in the desired concentration for 30 minutes at 37 °C. Cells were rinsed twice with cold phosphate buffered saline (PBS) then lysed with 500 µL of cold RIPA buffer (150 mM sodium chloride, 1.0% NP-40 detergent, 0.5% sodium deoxycholate, 0.1% SDS, 50 mM Tris, pH 8.0) with 1× Halt™ protease inhibitor cocktail (Thermo Scientific, Rockford, IL). The protein BCA assay kit (Thermo Scientific, Rockford, IL) was used to determine the total protein concentration of the cell lysates. The lysate containing 15 µg protein was used for the electrophoresis with a NuPAGE Novex 4-12% Bis-Tris protein gel (Novex™) followed by the electro blotting to PVDF membrane with a 0.45 µm pore size (Invitrogen™). The membrane was blocked with 3% bovine serum albumin in Tris-buffered saline for 1 hr, and then antibodies were used to probe the membrane. p38 mitogen-activated protein kinase (MAPK) activation was measured using anti-p38MAPK rabbit monoclonal primary antibody (Cell Signaling Technology) and Alexa Fluor 647 goat anti-rabbit (Life Technologies) secondary antibody. Vinculin protein was probed with anti-vinculin rabbit polyclonal antibody (Life Technologies) and used as the loading control in the Western blot experiments. The fluorescence intensity of the labeled protein bands were measured using the Typhoon FLA 9500 variable mode laser scanner (GE Healthcare) and the resulting band intensities were quantified with ImageJ.

4.3 Results and Discussion

4.3.1 Amyloid Beta 1-40 and 1-42 Ligands Alter RAGE Diffusion in HEK 293 Cells

Single particle tracking studies were conducted to measure the diffusion of the RAGE protein on the HEK293 cell membrane in the presence and absence of amyloid beta 1-40 or 1-42 peptides. The physiologically relevant circulating concentration of amyloid beta peptide is reported to be about 4.5 nM,[7] therefore, concentrations of 5 nM and 10 nM were used for this study to resemble physiological and slightly elevated levels. RAGE-HEK293 cells without ligand treatment were also studied as a control.

The number of times RAGE was located in a confined domain (i.e., exhibiting non-Brownian diffusion) was measured for the ligand-treated and control cells (Table 1). Since the observation time (i.e., the combined time for all the trajectories that were measured) varies slightly for each measurement, the number of times RAGE was located in a confined domain was normalized to the total observation time. In the absence of amyloid beta peptide, RAGE has 0.019 confined events per second. For all studied conditions, the presence of amyloid beta increased the number of confined events. Treatment with both concentrations of amyloid beta 1-40 resulted in approximately 2× more confined events compared to the control. Amyloid beta 1-42 peptide has fewer confined events compared to the 1-40 peptide treatment, but higher than the control value. For both amyloid beta peptides, the concentration of the peptide used in this study does not influence the number of confined events. These data indicate the increased non-Brownian mobility of the RAGE protein due to the amyloid beta treatment. In addition to showing more confinement events in the presence of amyloid beta peptides, once the RAGE is in a confined domain, it spends more time within the confined domain compared to the control (Figure 3A). The size of the confined domains obtained after amyloid beta 1-40 treatment had lower radii compared to that of the control, but amyloid beta 1-42 treatment behaved conversely (Figure 3B). RAGE is a membrane protein that is pre-assembled on the cell membrane as oligomers, and ligand binding enhances the formation of higher order RAGE clusters.[18] Amyloid beta 1-42 tends to form larger oligomers than beta 1-40 at the same concentration,[19-20, 40] RAGE binds predominantly with the soluble oligomeric form of amyloid beta peptides.[24] amyloid beta 1-42 also results in more RAGE within confined domains, and also appears to correlate with a larger spread in the size of domains.

The global diffusion coefficient was calculated for each of the trajectories categorized as Brownian (i.e., not exhibiting confined domains). For the trajectories with confined domains, the diffusion coefficients for the RAGE inside and outside the confined domain were calculated separately. For the fraction of RAGE exhibiting pure Brownian diffusion, both 5 and 10 nM amyloid beta 1-40 resulted in a significantly lower diffusion coefficient compared to the control; the same trend was observed for the diffusion coefficients measured inside and outside the confined domains (Figure 4B and C). Amyloid beta 1-40 exists as an equilibrium of monomers, dimers, trimers and tetramers at lower concentrations,[19] and amyloid beta 1-40 is known to interact with the head groups of lipids in the cell membrane. This results in a decrease in the fluidity of the membrane, and especially in the lipid rafts.[41-42] This may be the reason for the decreased diffusion coefficients observed for RAGE mobility when treated with amyloid beta 1-40 peptide. In comparison, the amyloid beta 1-42 resulted in a comparable average diffusion coefficients compared to the control, albeit a wider distribution was measured with amyloid beta 1-42 (Figure 4A-C). These diffusion data indicate that the presence of both amyloid beta peptides 1-40 and 1-42 affect the mobility of the RAGE protein on the cell membrane, but to a different extent and possibly with a different mechanism.

4.3.2 p38 MAPK Signaling is Activated by Amyloid Beta 1-42 Peptide

RAGE signaling induced by the treatment of amyloid peptides was measured as the activation of p38 MAPK signaling pathway. Preliminary results indicate that amyloid beta 1-42 at 5 nM resulted approximately 1.5-fold increase of the p38 MAPK signaling compared to the control. There was no statistically significant difference observed for the treatments with 10 nM amyloid beta 1-42 or 5 or 10 nM 1-40 peptide compared to the control (Figure 5).

RAGE-dependent signal transduction of Aβ occurred at lower concentrations of Aβ, whereas other mechanisms predominate at higher levels.[28] Also, at low concentration amyloid

beta 1-42 may exist in oligomeric forms whereas at higher concentrations it may result in the fibrillar form.[20] Intracellular signaling of RAGE protein requires the oligomerization of RAGE protein on the cell membrane. The binding site of the RAGE protein for amyloid beta oligomers is known as the V-domain, but the fibrils are known to be associated with the C1-domain.[43] Therefore the different forms of amyloid beta 1-42 at different concentrations may be binding with different domains of the RAGE protein, and affect the RAGE oligomerization and activate the intracellular signaling pathways with altered mechanisms. In the case of amyloid beta 1-40, the prominent form for these concentrations may be the monomeric form, and it may bind with the other components of cell membrane[42] rather than RAGE. This may alter the intracellular signaling pathways mediated by amyloid beta interaction with RAGE membrane protein.

4.4 Conclusions and Future Insights

Amyloid beta peptides affects the diffusion properties of RAGE protein. The 1-40 fragment slows the RAGE diffusion, but the 1-42 fragment has the converse effect at the studied concentrations. This difference is believed to be the result of different oligomeric forms reacting with RAGE and as well as other membrane components. Preliminary results show that the intracellular activation of p38 MAPK pathway is detected only for the amyloid beta 1-42 cell treatment at a 5 nM concentration. This supports the assumption that although both peptide types alter the RAGE diffusion, their intracellular signaling pathways may different. To analyze this statement, different forms of amyloid beta assemblies (monomeric, oligomeric and fibrillar forms) of 1-40 and 1-42 fragments separated at different concentrations could be used to study their interaction with RAGE protein as well as to determine how these assemblies affect the diffusion and intracelluar signaling mediated by RAGE-amyloid beta interaction and internalization of these assemblies.

Acknowledgements

This material is based upon work was supported by the National Science Foundation under Grant Number CHE-1709099.

Disclaimer

Any opinions, findings, and conclusions or recommendations expressed in this material are those of the authors and do not necessarily reflect the views of the National Science Foundation.

4.5 References

1. Neeper, M.; Schmidt, A. M.; Brett, J.; Yan, S. D.; Wang, F.; Pan, Y. C.; Elliston, K.; Stern, D.; Shaw, A., Cloning and expression of a cell surface receptor for advanced glycosylation end products of proteins. *Journal of Biological Chemistry* **1992,** *267* (21), 14998-5004.

2. Schmidt, A. M.; Vianna, M.; Gerlach, M.; Brett, J.; Ryan, J.; Kao, J.; Esposito, C.; Hegarty, H.; Hurley, W.; Clauss, M., Isolation and characterization of two binding proteins for advanced glycosylation end products from bovine lung which are present on the endothelial cell surface. *Journal of Biological Chemistry* **1992,** *267* (21), 14987-97.

3. Yamamoto, Y.; Yamamoto, H., RAGE-Mediated Inflammation, Type 2 Diabetes, and Diabetic Vascular Complication. *Front Endocrinol (Lausanne)* **2013,** *4*, 105-105.

4. Wendt, T.; Harja, E.; Bucciarelli, L.; Qu, W.; Lu, Y.; Rong, L. L.; Jenkins, D. G.; Stein, G.; Schmidt, A. M.; Yan, S. F., RAGE modulates vascular inflammation and atherosclerosis in a murine model of type 2 diabetes. *Atherosclerosis* **2006,** *185* (1), 70-77.

5. Hofmann, M. A.; Drury, S.; Hudson, B. I.; Gleason, M. R.; Qu, W.; Lu, Y.; Lalla, E.; Chitnis, S.; Monteiro, J.; Stickland, M. H.; Bucciarelli, L. G.; Moser, B.; Moxley, G.; Itescu, S.; Grant, P. J.; Gregersen, P. K.; Stern, D. M.; Schmidt, A. M., RAGE and arthritis: the G82S polymorphism amplifies the inflammatory response. *Genes Immun* **2002,** *3* (3), 123-35.

6. Craig, D. L.; Maren, K. F.; Emina, H. H.; Thiruvengadam, A., RAGE and RAGE Ligands in Cancer. *Current Molecular Medicine* **2007,** *7* (8), 777-789.

7. Deane, R.; Du Yan, S.; Submamaryan, R. K.; LaRue, B.; Jovanovic, S.; Hogg, E.; Welch, D.; Manness, L.; Lin, C.; Yu, J.; Zhu, H.; Ghiso, J.; Frangione, B.; Stern, A.; Schmidt, A. M.; Armstrong, D. L.; Arnold, B.; Liliensiek, B.; Nawroth, P.; Hofman, F.; Kindy, M.; Stern, D.; Zlokovic, B., RAGE mediates amyloid-β peptide transport across the blood-brain barrier and accumulation in brain. *Nature Medicine* **2003,** *9* (7), 907-913.

8. Maczurek, A.; Shanmugam, K.; Münch, G., Inflammation and the Redox-sensitive AGE–RAGE Pathway as a Therapeutic Target in Alzheimer's Disease. *Annals of the New York Academy of Sciences* **2008,** *1126* (1), 147-151.

9. Shi Du, Y.; Xi, C.; Douglas, G. W.; Ann Marie, S.; Ottavio, A.; Lih-Fen, L., RAGE: A Potential Target for Aβ-Mediated Cellular Perturbation in Alzheimers Disease. *Current Molecular Medicine* **2007,** *7* (8), 735-742.

10. Yan, S. S.; Wu, Z.-Y.; Zhang, H. P.; Furtado, G.; Chen, X.; Yan, S. F.; Schmidt, A. M.; Brown, C.; Stern, A.; Lafaille, J.; Chess, L.; Stern, D. M.; Jiang, H., Suppression of experimental autoimmune encephalomyelitis by selective blockade of encephalitogenic T-cell infiltration of the central nervous system. *Nature Medicine* **2003,** *9* (3), 287-293.

11. Muhammad, S.; Barakat, W.; Stoyanov, S.; Murikinati, S.; Yang, H.; Tracey, K. J.; Bendszus, M.; Rossetti, G.; Nawroth, P. P.; Bierhaus, A.; Schwaninger, M., The HMGB1 Receptor RAGE Mediates Ischemic Brain Damage. *The Journal of Neuroscience* **2008,** *28* (46), 12023-12031.

12. Schmidt, A. M.; Hasu, M.; Popov, D.; Zhang, J. H.; Chen, J.; Yan, S. D.; Brett, J.; Cao, R.; Kuwabara, K.; Costache, G., Receptor for advanced glycation end products (AGEs) has a central role in vessel wall interactions and gene activation in response to circulating AGE proteins. *Proceedings of the National Academy of Sciences* **1994,** *91* (19), 8807-8811.

13. Hofmann, M. A.; Drury, S.; Fu, C.; Qu, W.; Taguchi, A.; Lu, Y.; Avila, C.; Kambham, N.; Bierhaus, A.; Nawroth, P.; Neurath, M. F.; Slattery, T.; Beach, D.; McClary, J.; Nagashima, M.; Morser, J.; Stern, D.; Schmidt, A. M., RAGE Mediates a Novel Proinflammatory Axis: A Central Cell Surface Receptor for S100/Calgranulin Polypeptides. *Cell* **1999,** *97* (7), 889-901.

14. Ostendorp, T.; Leclerc, E.; Galichet, A.; Koch, M.; Demling, N.; Weigle, B.; Heizmann, C. W.; Kroneck, P. M.; Fritz, G., Structural and functional insights into RAGE activation by multimeric S100B. *The EMBO Journal* **2007,** *26* (16), 3868-3878.

15. Klune, J. R.; Dhupar, R.; Cardinal, J.; Billiar, T. R.; Tsung, A., HMGB1: Endogenous Danger Signaling. *Molecular Medicine* **2008,** *14* (7), 476-484.

16. Chavakis, T.; Bierhaus, A.; Al-Fakhri, N.; Schneider, D.; Witte, S.; Linn, T.; Nagashima, M.; Morser, J.; Arnold, B.; Preissner, K. T.; Nawroth, P. P., The Pattern Recognition Receptor (RAGE) Is a Counterreceptor for Leukocyte Integrins. *A Novel Pathway for Inflammatory Cell Recruitment* **2003,** *198* (10), 1507-1515.

17. Yan, S. D.; Zhu, H.; Zhu, A.; Golabek, A.; Du, H.; Roher, A.; Yu, J.; Soto, C.; Schmidt, A. M.; Stern, D.; Kindy, M., Receptor-dependent cell stress and amyloid accumulation in systemic amyloidosis. *Nature Medicine* **2000,** *6* (6), 643-651.

18. Fritz, G., RAGE: a single receptor fits multiple ligands. *Trends in Biochemical Sciences* **2011,** *36* (12), 625-632.

19. Bitan, G.; Kirkitadze, M. D.; Lomakin, A.; Vollers, S. S.; Benedek, G. B.; Teplow, D. B., Amyloid β-protein (Aβ) assembly: Aβ40 and Aβ42 oligomerize through distinct pathways. *Proceedings of the National Academy of Sciences* **2003,** *100* (1), 330-335.

20. Kirkitadze, M. D.; Condron, M. M.; Teplow, D. B., Identification and characterization of key kinetic intermediates in amyloid β-protein fibrillogenesis11Edited by F. Cohen. *Journal of Molecular Biology* **2001,** *312* (5), 1103-1119.

21. Yann, V.; Botond, P., Binding Sites of Amyloid β-Peptide in Cell Plasma Membrane and Implications for Alzheimers Disease. *Current Protein & Peptide Science* **2004,** *5* (1), 19-31.

22. Yan, S. D.; Chen, X.; Fu, J.; Chen, M.; Zhu, H.; Roher, A.; Slattery, T.; Zhao, L.; Nagashima, M.; Morser, J.; Migheli, A.; Nawroth, P.; Stern, D.; Schmidt, A. M., RAGE and amyloid-β peptide neurotoxicity in Alzheimer's disease. *Nature* **1996,** *382* (6593), 685-691.

23. Takuma, K.; Fang, F.; Zhang, W.; Yan, S.; Fukuzaki, E.; Du, H.; Sosunov, A.; McKhann, G.; Funatsu, Y.; Nakamichi, N.; Nagai, T.; Mizoguchi, H.; Ibi, D.; Hori, O.; Ogawa, S.; Stern, D. M.; Yamada, K.; Yan, S. S., RAGE-mediated signaling contributes to intraneuronal transport of amyloid-β and neuronal dysfunction. *Proceedings of the National Academy of Sciences* **2009,** *106* (47), 20021-20026.

24. Akhter F., A. A., Kesari K.K., Javed R., Ruokolainen J., Vuorinen T., AGE Exacerbate Amyloid Beta (Aβ) Induced Alzheimer Pathology: A Systemic Overview. In *Networking of Mutagens in Environmental Toxicology. Environmental Science and Engineering.*, K., K., Ed. 2019; pp 159-170.

25. Chaney, M. O.; Stine, W. B.; Kokjohn, T. A.; Kuo, Y.-M.; Esh, C.; Rahman, A.; Luehrs, D. C.; Schmidt, A. M.; Stern, D.; Yan, S. D.; Roher, A. E., RAGE and amyloid beta interactions: Atomic force microscopy and molecular modeling. *Biochimica et Biophysica Acta (BBA) - Molecular Basis of Disease* **2005,** *1741* (1), 199-205.

26. Arancio, O.; Zhang, H. P.; Chen, X.; Lin, C.; Trinchese, F.; Puzzo, D.; Liu, S.; Hegde, A.; Yan, S. F.; Stern, A.; Luddy, J. S.; Lue, L.-F.; Walker, D. G.; Roher, A.; Buttini, M.; Mucke, L.; Li, W.; Schmidt, A. M.; Kindy, M.; Hyslop, P. A.; Stern, D. M.; Du Yan, S. S., RAGE potentiates Aβ-induced perturbation of neuronal function in transgenic mice. *The EMBO Journal* **2004,** *23* (20), 4096-4105.

27. Lue, L.-F.; Walker, D. G.; Brachova, L.; Beach, T. G.; Rogers, J.; Schmidt, A. M.; Stern, D. M.; Yan, S. D., Involvement of Microglial Receptor for Advanced Glycation Endproducts (RAGE) in Alzheimer's Disease: Identification of a Cellular Activation Mechanism. *Experimental Neurology* **2001,** *171* (1), 29-45.

28. Yan, S. D.; Roher, A.; Chaney, M.; Zlokovic, B.; Schmidt, A. M.; Stern, D., Cellular cofactors potentiating induction of stress and cytotoxicity by amyloid β-peptide. *Biochimica et Biophysica Acta (BBA) - Molecular Basis of Disease* **2000,** *1502* (1), 145-157.

29. Jacobson, K., Lateral diffusion in membranes. *Cell Motility* **1983,** *3* (5), 367-373.

30. Liebman, P. A., A historical perspective on the lateral diffusion model of GTPase activation and related coupling of membrane signaling proteins. *Cellular Logistics* **2014,** *4* (2), e29389.

31. Ramadurai, S.; Holt, A.; Krasnikov, V.; van den Bogaart, G.; Killian, J. A.; Poolman, B., Lateral Diffusion of Membrane Proteins. *Journal of the American Chemical Society* **2009,** *131* (35), 12650-12656.

32. Lue, L.-F.; Walker, D. G.; Jacobson, S.; Sabbagh, M., Receptor for advanced glycation end products: its role in Alzheimer's disease and other neurological diseases. *Future Neurol* **2009,** *4* (2), 167-177.

33. Syed, A.; Zhu, Q.; Smith, E. A., Ligand binding affinity and changes in the lateral diffusion of receptor for advanced glycation endproducts (RAGE). *Biochim Biophys Acta* **2016,** *1858* (12), 3141-3149.

34. Sbalzarini, I. F.; Koumoutsakos, P., Feature point tracking and trajectory analysis for video imaging in cell biology. *Journal of Structural Biology* **2005,** *151* (2), 182-195.

35. Mainali, D.; Smith, E. A., Select cytoplasmic and membrane proteins increase the percentage of immobile integrins but do not affect the average diffusion coefficient of mobile integrins. *Anal Bioanal Chem* **2013,** *405* (26), 8561-8.

36. Menchón, S. A.; Martín, M. G.; Dotti, C. G., APM_GUI: analyzing particle movement on the cell membrane and determining confinement. *BMC Biophysics* **2012,** *5* (1), 4.

37. Simson, R.; Sheets, E. D.; Jacobson, K., Detection of temporary lateral confinement of membrane proteins using single-particle tracking analysis. *Biophysical Journal* **1995,** *69* (3), 989-993.

38. Zhu, Q.; Smith, E. A., Diaphanous-1 affects the nanoscale clustering and lateral diffusion of receptor for advanced glycation endproducts (RAGE). *Biochimica et Biophysica Acta (BBA) - Biomembranes* **2019,** *1861* (1), 43-49.

39. Bosch, Peter J.; Kanger, Johannes S.; Subramaniam, V., Classification of Dynamical Diffusion States in Single Molecule Tracking Microscopy. *Biophysical Journal* **2014,** *107* (3), 588-598.

40. Walsh, D. M.; Lomakin, A.; Benedek, G. B.; Condron, M. M.; Teplow, D. B., Amyloid β-Protein Fibrillogenesis: DETECTION OF A PROTOFIBRILLAR INTERMEDIATE. *Journal of Biological Chemistry* **1997,** *272* (35), 22364-22372.

41. Terzi, E.; Hölzemann, G.; Seelig, J., Self-association of β-Amyloid Peptide (1–40) in Solution and Binding to Lipid Membranes. *Journal of Molecular Biology* **1995,** *252* (5), 633-642.

42. Terzi, E.; Hölzemann, G.; Seelig, J., Interaction of Alzheimer β-Amyloid Peptide(1−40) with Lipid Membranes. *Biochemistry* **1997,** *36* (48), 14845-14852.

43. Sturchler, E.; Galichet, A.; Weibel, M.; Leclerc, E.; Heizmann, C. W., Site-Specific Blockade of RAGE-V_d Prevents Amyloid-β Oligomer Neurotoxicity. *The Journal of Neuroscience* **2008,** *28* (20), 5149-5158.

4.6 Tables and Figures

Table 4.1 Properties of the analyzed trajectories of RAGE on HEK293 cell membrane for the indicated ligand treatments.

	Total number of confined regions	Total time of the trajectories (s)	Total number of confined regions over the total time of the trajectories (s^{-1})
No treatment	26	1323	0.019
Amyloid beta 1-40 (5nM)	57	1593	0.036
Amyloid beta 1-40 (10nM)	49	1352	0.036
Amyloid beta 1-42 (5nM)	30	1349	0.022
Amyloid beta 1-42 (10nM)	34	1477	0.023

1 **10**
Asp- Ala- Glu- Phe- Arg- His- Asp- Ser- Gly- Tyr-
20
Glu- Val- His- His- Gln- Lys- Leu- Val- Phe- Phe-
30
Ala- Glu- Asp- Val- Gly- Ser- Asn- Lys- Gly- Ala-
40
Ile- Ile- Gly- Leu- Met- Val- Gly- Gly- Val- Val-
42
Ile- Ala-

Figure 4.1 The amino acid sequence of amyloid beta 1-40 and 1-42 peptides.

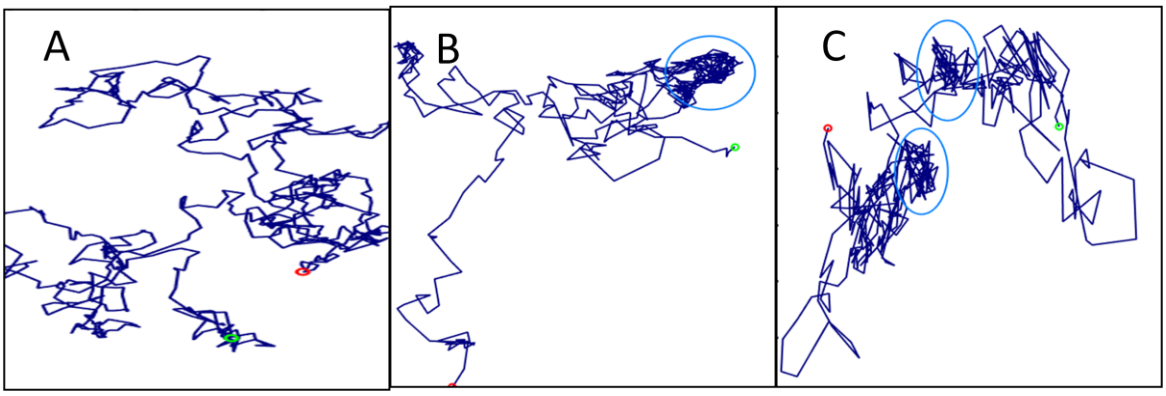

Figure 4.2 Representative RAGE mobile trajectories indicating: (A) a Brownian trajectory with no confined domains, (B) a trajectory with a single confined domain, and (C) a trajectory with two confined domains. Confined regions with Lc > 3.16 and tc > 1.95 s are indicated with light blue circles. Green and red spots indicates the starting point and the end point of the trajectory, respectively.

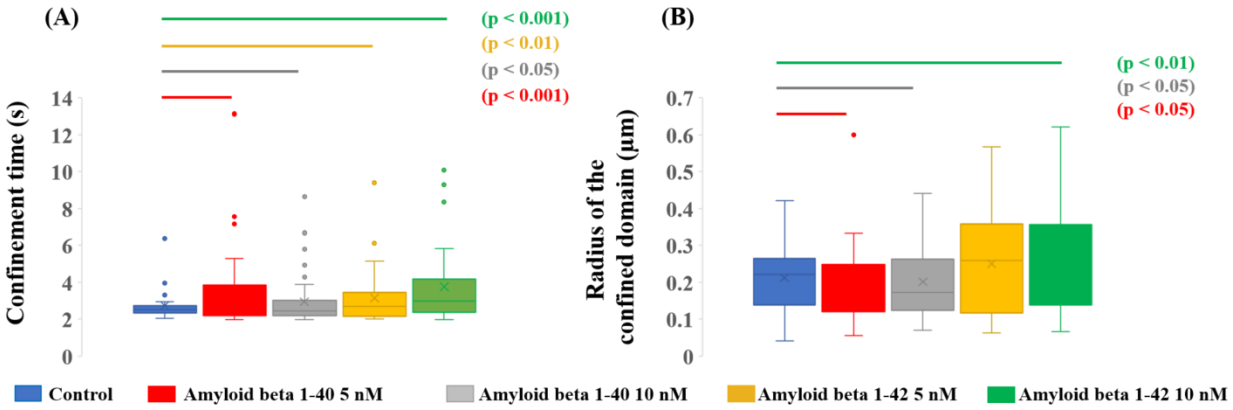

Figure 4.3 The box and whisker plots representing (A) the time and (A) the radius measured for the confined domains of the analyzed trajectories resulted from the indicated treatment. The upper and lower margins of the box indicates the first and third quartiles of the data set. Lines extending vertically from the boxes (whiskers) represent the variability outside the first and third quartiles. Outliers are given as individual points. The vertical line and the cross mark inside the box represent the median and the mean of the data set, respectively. The p-values below 0.05 showing the statistically significant differences compared to the non-treated cells are labeled with vertical lines.

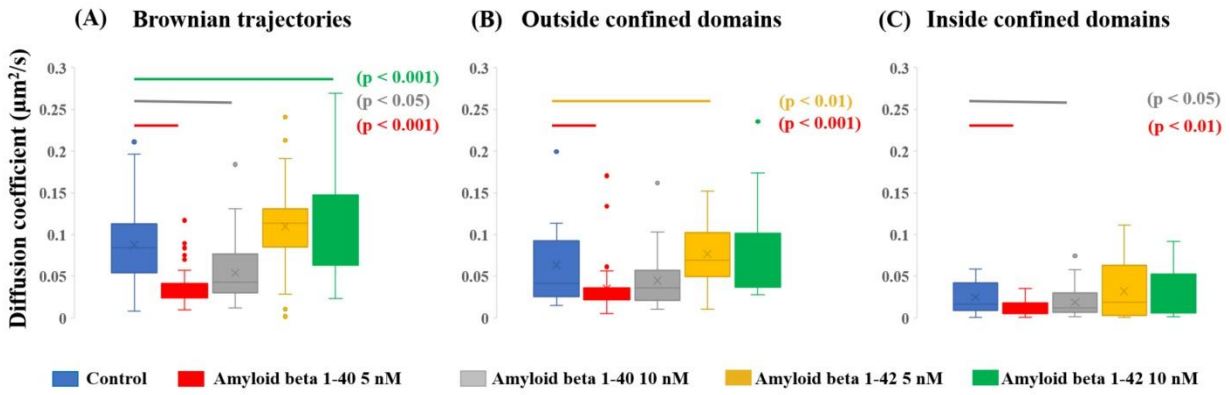

Figure 4.4 The box and whisker plots representing the diffusion coefficients calculated for the analyzed trajectories. (A) Global diffusion coefficient calculated for the Brownian trajectories with no confined regions. Diffusion coefficient calculated for the mobile fraction (B) outside and (C) inside the confined region. The p-values below 0.05 showing the statistically significant differences compared to the non-treated cells are labeled with vertical lines.

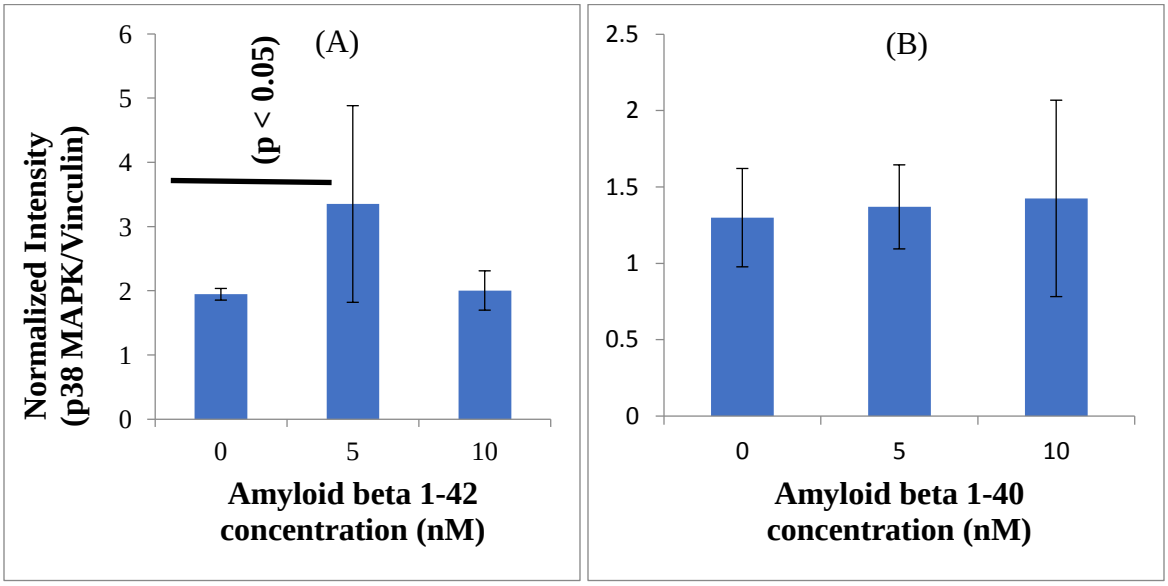

Figure 4.5 The plots of normalized signal intensities of p38 MAPK protein band divided by vinculin protein band detected from Western blot analysis of the RAGE-HEK293 cells treated with (A) amyloid beta 1-42 and (B) amyloid beta 1-40 peptides in two different concentrations.

CHAPTER 5. GENERAL CONCLUSIONS AND FUTURE WORK

The work presented in this dissertation was focused on two interrelated aspects: development of novel fluorescent probes for specific cellular organelle imaging as well as for super-resolution imaging, and evaluation of the diffusion properties of the receptor for advanced glycation endproducts (RAGE) interacted with amyloid beta ligands.

In Chapter 2, two coumarin-based compounds with sulfonamide side groups were developed to selectively image the endoplasmic reticulum (ER) in mammalian cells. Hydrophobicities of these probes were comparable to the commercially available ER targeting probes. Co-localization experiments using commercially available organelle specific probes for ER, mitochondria, and lysosomes, shown the ER selectivity (Pearson's correlation coefficient: 0.94) of these novel probes. Cytotoxicity of these probes in mammalian cells was low with IC50 values ranging 205 to 252 μM. They had fluorescent quantum yields of 0.60 when excited with 400 nm light. Their emission spectra were much narrower (from 435 to 525 nm in methanol) compared to the only commercially available 400 nm excitable ER probe, ER-Tracker^{TM} Blue-White DPX. Therefore, these probes are suitable for multicolor imaging with yellow and red emitting fluorophores. ER in live as well as fixed cells were imaged with these probes. Thus these probes are suitable for various types of cellular experiments. Lifetimes measured for these probes revealed their applicability for fluorescence lifetime imaging experiments. The conjugation of the coumarin core can be extended to develop a series of ER specific probes with varying absorption/emission profiles.

Chapter 3 described the development of a novel BODIPY-based photoactivatable probe for localization-based super-resolution imaging. The probe was attached with paclitaxel to image the microtubules. Super-resolution images of *in vito* microtubules were generated with an

average full width at half maximum diameter of 45 ± 10 nm. Live and fixed cell microtubules were also imaged at sub-diffraction level with this probe. Photoactiovation and excitation were achieved with a single visible laser (488 nm). Addition of reducing agents or oxygen scavengers in the imaging medium was not required. This probe utilized comparably lower laser irradiation (0.16 kW cm^{-2}) than traditional localization-based super-resolution probes. These features revealed the utility of this probe for super-resolution imaging of a variety of biological systems. Structural modifications of this probe to increase the water solubility and the brightness will further enhance the versatility of this probe. A series of probes with varying excitation/emission wavelengths could be developed to achieve multicolor super-resolution imaging with photoactivatable BODIPY.

Finally, RAGE lateral diffusion affected by amyloid beta peptides was measured using the fluorescence-based single particle tracking method. The 1-40 peptide slowed the RAGE diffusion but the 1-42 fragment acted controversially at the studied concentrations. Preliminary results showed that only the 1-42 treatment at 5nM concentration activated the p38MAPK signaling pathway. The different oligomerization pathways of 1-40 and 1-42 fragments may responsible for the controversial behavior of the two peptide types. Further studies are focused to study the affect of different forms of amyloid beta assemblies (monomeric, oligomeric and fibrillar forms) on RAGE mobility and related signaling pathways. RAGE ligands are also known to interact with other membrane receptors and to activate the common intracellular signaling pathways. Therefore dual color single particle tracking studies will be developed to study the crosstalk between ligand treated RAGE and related membrane receptors.